STUDY OF COMPOUND MATERIALS FOR X-RAY OPTICAL APPLICATIONS

By

Amol Singh

Enrolment Number: PHYS 03 2010 04 010

Raja Ramanna Centre for Advanced Technology
Indore-452013, India

A thesis submitted to the

Board of Studies in Physical Sciences

In partial fulfillment of requirements for the Degree of

DOCTOR OF PHILOSOPHY

of

HOMI BHABHA NATIONAL INSTITUTE

August 2015

Homi Bhabha National Institute

Recommendations of the Viva Voce Committee

As members of the Viva Voce Committee, we certify that we have read the dissertation prepared by **Amol Singh** entitled **"Study of Compound Materials for X-Ray Optical Applications"** and recommend that it may be accepted as fulfilling the thesis requirement for the award of Degree of Doctor of Philosophy.

Chairman- Dr. P. A. Naik		**Date:**	4/3/16
Guide/Convener- Dr. Mohammed H. Modi		**Date:**	4.3.2016
Co-guide- Dr. G. S. Lodha		**Date:**	4.3.16
External Examiner- Prof. Pankaj Srivastava	Srivastava	**Date:**	4/3/2016
Member 1- Dr. Dr. K. S. Bindra *(Out of station)*		**Date:**	
Member 2- Dr. H. S. Rawat	HSRawat	**Date:**	04/03/2016
Member 3- Dr. S. K. Dixit	SKDixit	**Date:**	4/3/2016
Member 4- Dr. Aparna Chakrabarti	Aparna Chakrabarti	**Date:**	4.3.2016
Member 5- Dr. S. M. Gupta		**Date:**	4.3.2016
Co-opted External Member- Dr. V. Sathe	Vasant Sathe	**Date:**	4.3.2016

Final approval and acceptance of this thesis is contingent upon the candidate's submission of the final copies of the thesis to HBNI.

I/We hereby certify that I/we have read this thesis prepared under my/our direction and recommend that it may be accepted as fulfilling the thesis requirement.

Date: 04-March-2016

Place: Indore

Co-Guide: 4.3.16
Dr. G. S. Lodha

Guide:
Dr. Mohammed H. Modi

STATEMENT BY AUTHOR

This dissertation has been submitted in partial fulfillment of requirements for an advanced degree at Homi Bhabha National Institute (HBNI) and is deposited in the Library to be made available to borrowers under rules of the HBNI.

Brief quotations from this dissertation are allowable without special permission, provided that accurate acknowledgement of source is made. Requests for permission for extended quotation from or reproduction of this manuscript in whole or in part may be granted by the Competent Authority of HBNI when in his or her judgment the proposed use of the material is in the interests of scholarship. In all other instances, however, permission must be obtained from the author.

Amol Singh

DECLARATION

I, hereby declare that the investigation presented in the thesis has been carried out by me. The work is original and has not been submitted earlier as a whole or in part for a degree/diploma at this or any other Institution/University.

Amol Singh

List of publications arising from the thesis

In Journal:

1. Study of structural and optical properties of zirconium carbide (ZrC) thin-films grown by ion beam sputtering for soft x-ray optical applications.
   Amol Singh, Mohammed H. Modi, A. K. Sinha, Rajnish Dhawan, G.S. Lodha
   Surf. Coat. Technol., (**2015**), **272**, 409-414**.**
2. Influence of structural disorder on soft x-ray optical behavior of NbC thin films.
   Amol Singh, Mohammed H. Modi, Parasmani Rajput, A. K. Sinha, G.S. Lodha
   J. Appl. Phys., (**2015**), **117**, 175301 (1-7).
3. Optical properties of zirconium carbide in 60–200 Å wavelength region using x-ray reflectivity technique.
   Amol Singh, Mohammed H. Modi, G.S. Lodha
   Appl. Opt., (**2015**), **54**, 253-258.
4. Cleaning of Carbon Layer from the Gold Films Using a Pulsed Nd:YAG Laser.
   Amol Singh, Ambar Choubey, Mohammed H. Modi, B.N. Upadhyaya, S.M. Oak, G.S. Lodha, S.K. Deb
   Appl. Surf. Sci., (**2013**), **283**, 612-616**.**
5. Quantitative determination of higher harmonic contents in the soft x-ray spectra of toroidal grating monochromator using a reflection multilayer.
   Mohammed H. Modi, R.K. Gupta, **Amol Singh**, G.S. Lodha
   Appl. Opt.**,** (**2012**), **51**, 3552-3557.

In conference proceedings:

1. Study of NbC thin films for soft x-ray multilayer applications.
   Amol Singh , Mohammed H. Modi, Parasmani Rajput, S. N. Jha, G.S. Lodha
   AIP Conf. Proc., (**2015**), **1665**, 080008 (1-3).

2. Structure and composition of zirconium carbide thin-film grown by ion beam sputtering for optical applications.
   Amol Singh, Mohammed H. Modi, Rajnish Dhawan, G.S. Lodha
   AIP Conf. Proc., (**2014**), **1591**, 869-871.
3. Study on effective laser cleaning method of carbon layer from gold surface.
   Amol Singh, A.K. Choubey, Mohammed H. Modi, B.N. Upadhyaya, G.S. Lodha
   J. Phys.: Conf. Ser., (**2013**), **425**, 152020 (1-4).

Other publications during the PhD work

1. Study on effective cleaning of gold layer from fused silica-mirrors sample using nanosecond pulsed Nd: YAG laser.
   A.K. Choubey, **Amol Singh**, Mohammed H. Modi, B.N. Upadhyaya, G.S. Lodha, S.M. Oak
   Appl. Opt., (**2013**), **52**, 7540-7548**.**
2. Study on Higher Harmonic Suppression Using Edge Filter and Polished Si Wafer.
   R. K. Gupta, **Amol Singh** , Mohammed H. Modi, G.S. Lodha
   AIP Conf. Proc., (**2014**), **1591**, 988-991.
3. Comparison of Mo/Si and NbC/Si lamellar multilayer gratings near Si absorption edge.
   Ankita Niranjan, Mohammed H. Modi, **Amol Singh**, Mourad Idir, G.S. Lodha
   AIP Conf. Proc., (**2014**), **1591**, 687-690.
4. Analysis of soft x-ray/VUV transmission characteristics of Si and Al filters.
   Aby Josheph, Mohammed H. Modi, **Amol Singh**, R. K. Gupta, G.S. Lodha
   AIP Conf. Proc., (**2013**), **1582**, 498-501.

DEDICATED TO MY PARENTS

ACKNOWLEDGEMENTS

It is a great honor and privilege to express my deep sense of gratitude to my Ph.D. guide Dr. Mohammed H. Modi, at the successful completion of my thesis work. He infused enthusiasm at every step in my research work. He has a cool temperament that certainly benefits a person working with him. I feel invigorated at every moment on recalling the words of inspirations received from him. He has a great ability to keep the person motivated. The academic freedom I enjoyed from him was commendable.

I sincerely thank Dr. G. S. Lodha, Co-supervisor of my project work, for giving all kinds of freedom in carrying out this research work. He has infused many ideas that helped me a lot in growing up in the field of science. He owns a great quality to sort out the experimental difficulties with many exciting ideas that eventually helped me in reaching the targets during this project work.

I am extremely thankful to Dr. P. A. Naik, Head ISUD for his constant encouragement. I am grateful to Dr. A. K. Tyagi, BARC and Dr. S. M. Oak and members of C3-Doctoral Committee for their constructive motivation and guidance.

I sincerely thank Dr. Aparna Chakrabarti for proof reading my thesis and for many suggestions I received from her time to time.

I am extremely thankful to Dr. Tapas Ganguli for various help and suggestions during the course of my thesis.

Thanks are due to Dr. Andrew Nelson (ANSTO, Australia) for providing and modifying Moto-fit tool for reflectivity data analysis.

I sincerely thank to Dr. A. K. Sinha, Dr. Shailendra Kumar and Dr. Sanjay Rai for fruitful discussions and suggestions time to time.

I specially thank to Mr. Rajkumar Gupta for help in learning the operation of Reflectivity beamline.

I sincerely thank Mr. Rajnish Dhawan for help in sample deposition. I thank Dr. Ambar Choubey, Dr. B. N. Upadhyaya for help in operation of Nd:YAG laser. I sincerely thank Mr. Manvendra Singh for help in GIXRD measurements at ADXRD beamline. Thanks are due to Dr. Parasmani Rajput and Dr. S. N. Jha for help in EXAFS measurements at Scanning EXAFS beamline.

I would like to thank Dr. V. G. Sathe of IUC Indore for help in Raman measurements. Thanks are due to Dr. D. M. Phase and Mr. A. D. Wadikar of IUC Indore for help in XPS measurements. Thanks are due to Ms. Mangalika Sinha for help in proofreading the thesis.

I am indebted to members of Indus-1 operation crew without whom it would have not been possible to do the experiments on Indus-1.

I specially thank my friend Gaurav Mishra for his constant motivation right from my B.Sc. for my career.

Above all, it would have not been possible for me to achieve this milestone in my research career without encouragement and support from my all family members who have dreamed and prayed for my all around success. My Parents who hold exceptional concerned about my success has imparted a great enthusiasm at every moment. Without active support of my wife Anuradha, I couldn't imagine to triumph over different landmarks during my research career.

Contents

SYNOPSIS

The objective of the present thesis is to investigate the properties of new materials to probe their suitability as x-ray optical elements. Multilayer mirrors comprised of low Z / high Z elements are widely used in modern synchrotron radiation sources[1]. Such multilayers pose a severe drawback because of the high chemical reactivity of the constituent elements when they are used at elevated temperatures in high heat load environment. Compound materials have shown stable and enhanced optical performance in soft x-ray energy region[2]. NbC/Si multilayer is proposed for energy region near the Si L edge (124 Å) where it exhibits a better thermal stability and an identical reflectivity performance compared to Mo/Si multilayer[2]. Similarly, near the Al L-edge (170 Å), the simulations suggest that the ZrC/Al multilayer seems to have better performance than Zr/Al multilayer. The expected performance from compound material is difficult to achieve. This is because when thin films are deposited from bulk target, there are growth related changes in structural and chemical properties, which affect the optical performance. Therefore, prior to actual use of such materials, they must be investigated thoroughly for their structural and chemical properties.

Further, to predict the optical response of a material to incident radiation, the knowledge of optical constants δ and β is essential. In case of compound materials, optical constants are calculated by taking a weighted sum of the optical constants of the constituent elements using the database of Henke et al[3]. This approach works well for photon energies away from the absorption edges of the constituent elements. In the close vicinity of an absorption edge, this approach fails, as the formation of chemical bonds lead to a shift in the absorption edge. In general, overlapping of wave functions of electrons of the constituents of a compound material leads to modification of the optical constants. Several techniques such as transmission, photoemission, angle-dependent reflections etc. have been applied to determine the optical constants. In angle-dependent reflectivity technique both δ and β can be determined experimentally at discrete photon energies, which is an advantage over the transmission measurements where only the absorption (β) value is measured experimentally.

In this thesis, we have performed a detailed structural and chemical investigation on thin films of compound materials NbC and ZrC. The structural parameters of these films are determined using grazing incidence x-ray reflectivity (XRR) technique. Optical response of these two materials (NbC and ZrC thin film) is measured using soft x-ray reflectivity (SXR) technique at Indus-1 reflectivity beamline[4]. Several techniques such as grazing incidence x-ray diffraction (GIXRD), x-ray photoelectron spectroscopy (XPS), x-ray absorption fine structure (XAFS), power spectral density (PSD) analysis using atomic force microscopy (AFM) images etc. are used for the determination of surface morphology and structural properties of NbC and ZrC thin films.

Further, surface contamination on x-ray optical elements seriously affects the optics performance. Carbon contamination and hydrocarbon cracking on optical elements in soft x-ray spectrometers and synchrotron radiation beamlines is a severe problem. Simulations suggest that a 10 Å thick carbon layer reduces relative reflectivity of a single multilayer optical surface by 1.4%, because of high absorption of EUV radiation by carbon which makes this contamination layer as a serious source of loss of throughput[5]. Extreme ultraviolet lithography (EUVL) scanner optics typically consists of ten such reflecting layers, where the total throughput deteriorates drastically. As a remedy, the optical elements need to be replaced periodically[6]. Since these optical elements are very costly, hence disposal of the damaged mirrors is not a viable solution. So it is desirable to develop a technique for periodic removal of the carbon contamination without damage or modifications of the surface underneath[7,8,9].

To remove the surface contamination from x-ray optical elements, a laser based cleaning technique is deployed successfully. We have optimized several parameters of laser system to remove carbon contamination from the optics surface. The system has been optimized to remove underneath coating material (gold layer in present case) successfully.

Thesis Outline:

This thesis comprises of six chapters and the contents of each chapter are discussed briefly in the following section.

1. Introduction:

This chapter contains literature survey and details of the importance of compound materials in x-ray optical applications. Several techniques for determination of optical constants and their merits/ demerits are discussed.

2. Experimental techniques and procedures:

This chapter describes the details of experimental techniques used in present thesis work. Samples are prepared using ion beam sputtering (IBS) technique, details of IBS setup is discussed. Theoretical aspects of x-ray reflectivity measurements and data analysis procedure are elaborated. Details of the reflectivity beamline used for reflectivity measurements for optical constant analysis has been discussed. Higher harmonic contents from the beamline are calculated quantitatively and the results are explained.

The beamline mirrors are generally get contaminated with ambient hydro carbon present in vacuum vessels during their exposure to intense synchrotron light. Therefore the coating materials of the mirror need to be removed and recoated with a fresh material for further use. In this chapter the procedure and results of gold layer removal is also described.

Details of other system used for structural characterizations like x-ray photoelectron spectroscopy (XPS), grazing incidence x-ray diffraction (GIXRD), atomic force microscopy (AFM), x-ray absorption fine structure (XAFS), Raman spectroscopy, x-ray absorption spectroscopy (XAS) have also been described in this chapter.

3. Study on structural and optical properties of NbC:

NbC has earlier been found to be suitable candidate for the fabrication of soft x-ray multilayer for high reflectivity performance near Si L-edge region[2]. In this chapter, we have carried out detailed studies of structural and optical properties of NbC thin films on Si substrate, deposited using ion-beam sputtering technique. A discrepancy of ~30% in soft x-ray reflectivity performance of NbC film has been observed in the present study, which could not be explained with Henke’s tabulated data. To understand this deviation, a detailed structural and chemical characterization of NbC thin films of different thicknesses (100-500 Å) has been carried out using several experimental techniques. Structural parameters (thickness, roughness and density) of these films have been determined using XRR technique. The rms surface roughness for all the thin films is found in 3-6 Å range, which suggests smooth surface morphology of NbC thin films. Density of NbC films is found to be increasing from 6.13 g/cm^3 to 7.11 g/cm^3 with increase in film thickness from 100 Å to 500 Å (bulk density is 7.82 g/cm^3). Further, to understand this increase in density of the films, XANES and EXAFS studies have been carried out. Detailed analysis suggests that Nb-Nb coordination increases with increase in film thickness. This implies the possibility of presence of Nb vacancy in the films at lower thicknesses.

Further, to investigate the chemical stoichiometry as a function of the depth of the films, detailed XPS studies have been carried out. Analysis of XPS results after various sputtering cycles suggests that some amount of unreacted carbon is present in the depth of the film.

Optical constants of NbC in 60-150 Å wavelength region are measured using SXR technique and compared with the tabulated Henke values. The values of δ and β are found to be lower (5 to 38 %) than the bulk value.

In conclusion, Nb vacancy and presence of unreacted carbon is found to be responsible for variation in optical constants that in turn lowers the reflectivity performance of thin film in soft x-ray region. Our present study suggests that the NbC is a suitable material for soft x-ray optical applications.

4. Study on structural and optical properties of ZrC:

Zr/Al multilayers are regularly used near Al edge as reflecting mirrors[10]. However, these systems are thermally unstable above 200 °C. To improve the thermal stability, Zr may be replaced by a suitable compound material. Contrast between the optical constants of ZrC and Al, as obtained from Henke et al[3] tabulated data, has been found to be better than those of Zr and Al. Therefore, we have carried out detailed studies on structural and optical properties of ZrC thin films and the results are described in this chapter. A discrepancy of 9-30% in soft x-ray reflectivity performance of ZrC film is observed, which could not be explained using Henke's tabulated data. To understand this deviation, ZrC thin films of different thicknesses (100 to 300Å) on Si substrate are deposited using ion beam sputtering technique. Following that, detailed structural and chemical characterization of these films has been carried out. Structural parameters (thickness, roughness and density) of ZrC thin films have been determined using XRR technique. The rms surface roughness for all the thin films is found to be in 3-6 Å range, which indicates smooth surface morphology of ZrC thin films. Density of ZrC films is found to be about 97% of the bulk density for all the thicknesses. This high density of the films offers an advantage towards their application as x-ray thin films/multilayers.

Further, to investigate the chemical stoichiometry as a function of the depth of the films, detailed XPS studies have been carried out. Analysis of XPS results after various sputtering cycles established the presence of unreacted carbon near the surface with small amount of oxygen throughout the film thickness.

Optical constants of ZrC in 60-200 Å wavelength region are measured using SXR technique. The δ and β values are found to be 15-35 % less than the data obtained from Henke's tabulated values. This deviation in optical constants in soft x-ray region may be due to the change in chemical composition of ZrC as discussed above. Our detailed studies suggest that ZrC may turn out to be a suitable candidate for the fabrication of soft x-ray multilayer for high reflectivity performance near Al L-edge region.

5. Surface contamination effects on optical properties:

In this chapter, the effect of surface contamination on optics performance is described. Laser cleaning technique has been deployed for cleaning of optical elements for the first time. A lamp pumped acousto-optic Q-switched Nd:YAG laser system, with 100 ns pulse duration and 10 mJ of pulse energy is used for laser cleaning process. Process parameters such as laser repetition rate, pulse duration, pulse energy, laser intensity, and focused beam area for the carbon thin film are optimized for carbon cleaning experiments.

Further, reflectivity results obtained from gold mirror before and after laser cleaning of carbon layer suggest that the carbon layer has been completely removed. Surface quality is analyzed after laser cleaning using SXR and PSD analysis and it has been found that the laser cleaned surface has significant improvement compared to the actual mirror surface. Cleaning efficiency analyzed using several techniques (like XPS, Raman spectroscopy) are discussed.

6. Summary and future scope:

In this chapter summary and conclusion of the whole work is described briefly. It also describes the future direction and possibility of use of compound materials in multilayer mirrors and monochromators. Scope of compound materials in x-ray optics with improved performance for near future is discussed.

References:

1. Alexander Kazimirov, D. M. Smilgies, Q. Shen, X. Xiao, Q. Hao, E. Fontes, D. H. Bilderback, Sol M. Gruner Y. Platonov and V. V. Martynov, “Multilayer X-ray optics at CHESS” J. Synchrotron Radiation, **13**, 204 (2006).
2. Mohammed H. Modi, S. K. Rai, Mourad Idir, F. Schaefers, G. S. Lodha, “NbC/Si multilayer mirror for next generation EUV light sources” Opt Exp. **20**, 15114 (2012).
3. http://henke.lbl.gov/optical_constants/
4. R.V. Nandedkar, K.J.S. Sawhney, G.S. Lodha, A. Verma, V.K. Raghuvanshi, A.K.Sinha, M.H. Modi, M. Nayak, Curr. Sci. “First results on the reflectometry beamline on Indus-1” **82**, 298 (2002).
5. D.L. Windt, Comput. Phys. “IMD-Software for modeling the optical properties of multilayer films” **12**, 360 (1998).
6. J. Chen, E. Louis, C.J. Lee, H. Wormeester, R. Kunze, H. Schmidt, D. Schneider, R.Moors, W. van Schaik, M. Lubomska, F. Bijkerk, “Detection and characterization of carbon contamination on EUV multilayer mirrors” Opt. Exp. **19**, 16969 (2009).
7. K. Boller, R.-P. Haelbich, H. Hogrefe, W. Jark, C. Kunz, Nucl. Instrum. Methods in Phys. Research, “Investigation of carbon contamination of mirror surfaces exposed to synchrotron radiation” **208**, 273 (1983).
8. T. Koide, S. Sato, T. Shidara, M. Niwano, M. Yanagihara, A. Yamada, A. Fujimori,A. Mikuni, H. Kato, T. Miyahara, Nucl. Instrum. Methods A, “Investigation of carbon contamination of synchrotron radiation mirrors” **246**, 215 (1986).
9. C. Tarrio, S. Grantham, Rev. Sci. Instrum, “Synchrotron beamline for extreme-ultraviolet multilayer mirror endurance testing”. **76**, 056101 (2005).
10. Qi Zhong, Wenbin Li, Zhong Zhang, Jingtao Zhu, Qiushi Huang, Haochuan Li, Zhanshan Wang, Philippe Jonnard, Karine Le Guen, Jean-Michel André, Hongjun Zhou, Tonglin Huo, “Optical and structural performance of the Al(1%wtSi)/Zr reflection multilayers in the 17–19nm region” Opt. Express **20** (2012) 10692.

List of Figures:

List of Tables:

Chapter 1.

Introduction

In this chapter the importance of x-ray thin films/multilayers are described. Theoretical background of refractive index and optical constants are described. The critical issues related with soft x-ray optics are discussed. Scope of the present work is described.

1.1. Introduction:

The electromagnetic spectrum extends from the radio waves to the x-ray region. X-ray was one of the most important discoveries in science by W C Röntgen in 1895. There is no sharp boundary in soft x-ray and extreme ultraviolet region (EUV). The EUV region starts from photon energies of about 30 eV and extends up to about 250 eV and the soft x-ray energy region extends from about 250 eV to few keV, with corresponding wavelengths in the range of 400 Å to 50 Å and 50 Å to 3 Å respectively. The progress in use of soft x-ray/EUV region evolved very slowly because of extremely high absorption due to several atomic resonances in all the materials, typically of order one micrometer or less. In last many years researchers have shown renewed interest in the area of soft x-ray/EUV radiation applications. This spectral region offers great opportunities to both science and technology. There are several important and timely applications in this energy region such as microscopy, lithography, astrophysics, solid state physics etc. EUV lithography is a rapidly developing area[1,2], where the objects in nm scale or less are fabricated such as micro stepper, Schwarzchild optics, metal oxide semiconductor electronics devices, computer circuits etc. Further with the development of new technologies, the performances of optical components (such as gratings monochromators, detectors, mirrors, lenses etc.) are improved.

In soft x-ray beamlines, grating monochromators are used worldwide at the synchrotron radiation sources. The monochromatic x-rays from grating monochromators are used for several experiments in material science, which contain significant amount of higher harmonic contamination[3,4]. The fractional composition of these higher harmonic contaminations depends on several factors, such as grating diffraction efficiency, detector response, mirror reflectivity etc. The undesired photons of higher harmonics are a common characteristic and are an intrinsic problem in synchrotron beamlines, which makes the analysis of experimental data quite complicated. The higher harmonic contribution in a grazing incidence beamline can be around 25% or more. In such cases the higher order contamination need to be suppressed or quantitatively determined. Absorption based harmonic suppressor system comprised of transmission foils; gas filters and so forth are used in various beamlines worldwide. These filters work near the absorption edges of the filter materials. In order to minimize the artifacts of higher harmonics in experimental data the spectral purity of the grating based beamlines need to be determined. In this thesis Mo/Si multilayer (ML) is used to determine the higher harmonic contents of the soft x-ray beamline which is explained in chapter-2.

The strong absorption in this region is the main characteristics of optical response of matter, because the binding energies for all materials are comparable to soft x-ray/EUV energy region. The complex refractive index in x-ray region is defined as $n=1-\delta+i\beta$, where delta (δ) and beta (β) are dispersion and absorption terms respectively and are known as optical constants. The values of δ and β are comparable in this energy region. The dispersive part $1-\delta$ is very close to unity and therefore the refraction phenomena are very weak. Because of high absorption and weak refraction, utilization of conventional refractive optical elements (such as lens) seems impossible. The other possibility is to use diffractive/ reflective optical elements such as gratings, mirrors etc. For a perfectly smooth surface, the reflected intensity at grazing incidence angle θ can be determined using the Fresnel equations explained below in section 1.2.4.1. From the Fresnel equations, the reflectivity at extreme grazing angles (θ »$=0^o$) is close to 1, while as θ approaches to normal incidence ($\theta=90^o$), the reflectivity falls down drastically {$R= (\delta^2+\beta^2)/4$}. Figure 1.1 shows the calculated normal incidence reflectivity as a function of energy for Nb, Zr, Al and Si for perfectly smooth surface. In the practical situations the reflectivity further drops because of imperfections (roughness) at the interfaces. Thus utilization of single layer reflective optics at near normal incidence is not feasible. However there are several issues of imaging defects, such as spherical aberrations, coma and astigmatism. Several optical configurations (such as Kirkpatrick-Baez Mirrors) were invented to solve these issues. Most of the optical elements used in soft x-ray SR beamlines involve highly aspherical surfaces[5] such as toroidal mirrors, paraboloids, and hyperboloids. Such surfaces are quite complicated for precise fabrication and often these fabrications are partially successful.

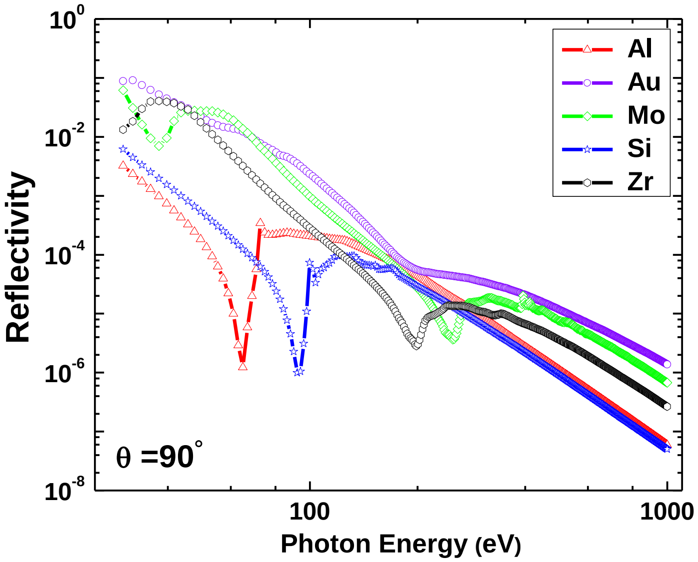

Figure 1.1: Normal incidence reflectivity for Al, Au, Mo, Si and Zr are shown in the 30-to 1000 eV energy region, calculated for s polarized light. The reflected intensities are very small for all the materials, and decreases rapidly with energy, suggesting that single layer mirrors cannot be used at normal incidence in soft x-ray/EUV energy region.

Figure 1.1 suggests that a mirror made of a single layer cannot reflect significant amount of radiation at normal incidence, it is quite challenging to develop reflective elements with enhanced reflectivity at normal incidence. Multilayer mirrors comprised of alternating layers of low Z/high Z elements came into existence as a solution to this problem[6]. The multilayer mirror works according to Bragg's condition $2d\sin\theta=n\lambda$, where d is the thickness of each individual layer pair, called multilayer period and λ is the wavelength. The reflected intensity is enhanced by N^2 times in comparison to that of thin film mirror composed of single layer. This elemental multilayer poses a severe drawback of intermixing and alloy formation among the constituent elements. In the present thesis we have investigated compound materials to replace one of the elements from multilayer system for improved stability and to avoid the intermixing problem.

1.2. Theoretical Background:

1.2.1. Origin of Refractive Index:

To understand the abilities of soft x-ray scattering to obtain the structural and chemical information, it is necessary to understand the interaction of x-ray with matter. Although for more accurate results, quantum mechanical calculations are required[7], but much can be explained from semi-classical model[8]. The basic results are similar in both quantum mechanical model and in semi-classical model. In a simple semi-classical model, the atom can be represented by a massive positively charged ($+Ze$) nucleus surrounded by number of (Z) electrons at discrete binding energies. In this model the nucleus does not respond dynamically to the incident high frequency fields, but the electrons are caused to oscillate at the frequency ω imposed by the incident electric field $\boldsymbol{E_i}$ of the electromagnetic wave. Various electrons, bound by different restoring forces, respond differently to the impressed fields. The response of the electrons depend on the resonant frequencies ω_s of the bound electrons and on the closeness of the driving (incident wave) frequency to the resonance, that is ($\omega - \omega_s$). Further, an equation of motion is required for each of the bound electrons so that its acceleration can be determined in the presence of an incident field. Thus it is required to determine an appropriate formulation of Newton's second law of motion ($F = ma$) for each of the bound electrons. In the semi-classical model the multi-electron atom can be treated as a collection of harmonic oscillators, each with its set of resonances $\hbar\omega_s$, which can be associated with the known transitions between the stationary states of the atom. Before proceeding to the semi-classical equation of motion it can be noted that in a proper quantum mechanical model, the presence of a time dependent external electric field perturbs the atomic system so that there is a time dependent probability of finding the atom in various stationary states ψ_n – perhaps upper and lower states – oscillating continuously between the two at the impressed frequency and thus giving the sense of a time-dependent oscillation of charge distribution within the atom. In the semi-classical model each bound electron is forced to execute the simple harmonic motion by the incident electric field while in the presence of the restoring central force field of the massive, positively charged nucleus. Using expressions for the transverse acceleration of each bound electron, in terms of the incident field $\boldsymbol{E}_i$ which excites it to oscillation the equation of motion for each of these electrons can be written as:

$$m\frac{d^2\boldsymbol{x}_s}{dt^2}+m\gamma\frac{d\boldsymbol{x}_s}{dt}+m\omega_s^2\boldsymbol{x}_s=-e\left(\boldsymbol{E}_i+\boldsymbol{v}_s\times\boldsymbol{B}_i\right) \qquad \textbf{1.1}$$

where the ($\boldsymbol{v_s}\times\ \boldsymbol{B}_i=0$) term is small for the non-relativistic oscillation velocities $\boldsymbol{v}$ and can be ignored.

In this equation, the first term is the acceleration, the second term is the dissipative force term that accounts for the energy loss (assume $\gamma\ /\omega <<1$), and the third term is due to the restoring force for an oscillator of resonant frequency ω_s. On the right hand side of Eq-1.1 the term $\{-e\ (E_i+\ \boldsymbol{v_s}\times\ \boldsymbol{B}_i)\}$ is the Lorentz force exerted by the incident field; and where the ($\boldsymbol{v_s}\times\ \boldsymbol{B}_i=0$) term is small for the non-relativistic oscillation velocities $\boldsymbol{v}$ and can be ignored.

Here it can be assumed that the displacement x, velocity, and acceleration will have the same $e^{-i\omega t}$ time dependence. So the time derivative can then be replaced by $-i\omega$ and Eq. 1.1 becomes:

$$m\left(-i\omega_s\right)^2 \boldsymbol{x}_s + m\gamma(-i\omega_s)\boldsymbol{x}_s + m\omega_s^2\boldsymbol{x}_s = -e\boldsymbol{E}_i \qquad \textbf{1.2}$$

But in case of atom which contains many electrons, the electron distribution function within the atom can be written as:

$$n(\boldsymbol{r},t) = \sum_{s=1}^{z} \delta\left[\boldsymbol{r} - \Delta\boldsymbol{r}_s(t)\right] \qquad \textbf{1.3}$$

where r is the coordinate of the nucleus and $\Delta\boldsymbol{r}$ is the vector displacement from the nucleus and Z is the total number of electrons in the atom. In order to account for the differing phase seen by each electron, the spatial dependence of the incoming wave must be kept. To do so the electric field should be rewritten as:

$$\boldsymbol{E}_i(\boldsymbol{r},t) \rightarrow \boldsymbol{E}_i e^{-i(\omega t - \boldsymbol{k}_i.\Delta\boldsymbol{r}_s)} \qquad \textbf{1.4}$$

Further the expression for $\boldsymbol{E}(\boldsymbol{r},t)$ is modified by approximating $\boldsymbol{r}_s$ by $\boldsymbol{r}$ in the slowly varying amplitude term, while retaining it in the rapidly varying phase term. The electric field is then given by:

$$E(r,t) = -r_e \sum_{s=1}^{Z} \frac{\omega^2 E_i \sin\Theta}{\omega^2 - \omega_s^2 + i\gamma\omega} \frac{1}{r} \exp\left\{-i\left[\omega\left(t - \frac{r}{c}\right) + \omega\left(\frac{\boldsymbol{k}_0.\Delta\boldsymbol{r}_s}{c}\right) - \boldsymbol{k}_i.\Delta\boldsymbol{r}_s\right]\right\} \qquad \textbf{1.5}$$

where Θ is the angle between $\boldsymbol{E}_i$ and $\boldsymbol{k}$, $t-r/c$ is the retarded time. Now introducing the density fluctuation wave vector $\Delta\boldsymbol{k}=\boldsymbol{k}-\boldsymbol{k}_i$ associated with the inhomogeneity of the medium, the expression for $E(r,t)$ becomes:

$$E(\boldsymbol{r},t) = -\frac{r_e}{r} \underbrace{\left[\sum_{s=1}^{Z} \frac{\omega^2 e^{-i\Delta\boldsymbol{k}.\Delta\boldsymbol{r}_s}}{\omega^2 - \omega_s^2 + i\gamma\omega}\right]}_{f(\Delta\boldsymbol{k},\omega)} E_i \sin\Theta e^{-i\omega(t-r/c)} \qquad \textbf{1.6}$$

The complex atomic scattering factor, a function of the incident wave frequency ω, the various resonance frequencies ω_s of the bound electrons, and the phase terms due to their various positions within the atom, $\Delta\boldsymbol{k}.\Delta\boldsymbol{r}_s$ describes the electric field amplitude of the scattered wave relative to that scattered by a free electron and is given by:

$$f(\Delta\boldsymbol{k},\omega)=\left[\sum_{s=1}^{Z}\frac{\omega^2 e^{-i\Delta\boldsymbol{k}.\Delta\boldsymbol{r}_s}}{\omega^2-\omega_s^2+i\gamma\omega}\right] \qquad \mathbf{1.7}$$

Further the phase expression in Eq.-1.7 gets simplified in two special cases, a) long wavelength limit and b) scattering in the forward direction in either case the expression for the atomic scattering factor reduces to:

$$f^0(\omega)=\left[\sum_{s=1}^{Z}\frac{\omega^2}{\omega^2-\omega_s^2+i\gamma\omega}\right] \qquad \mathbf{1.8}$$

In the simple semi-classical model g_s are integers that represent the number of electrons associated with a given resonance frequency ω_s and is known as oscillator strength. Thus the sum of oscillator strengths is equal to the total number of electrons:

$$\sum_s g_s = Z \qquad \mathbf{1.9}$$

A shortcoming of the semi-classical model is that while it gives the proper form of scattering cross-sections and refractive index, it does not provide a basis to calculate the oscillator strengths. In the quantum mechanical description these oscillator strengths arise naturally as non-integer transition probabilities, g_{kn}, between stationary states ψ_k and ψ_n of the atom, leading to an expression similar to Eq.-1.9 when summed over final states n from an initial state k:

$$\sum_n g_{kn} = Z \qquad \mathbf{1.10}$$

Eq.-1.10 is known as the Thomas–Reiche–Kuhn sum rule[9,10,11]. After introducing the oscillator strengths, the atomic scattering cross-sections of a multi-electron atom for the special cases of long wavelength ($\lambda >> a_0$) or small angles ($\theta << \lambda / a_0$) can be given as:

$$\sigma(\omega) = \frac{8\pi}{3} r_e^2 \left| f^0(\omega) \right|^2 = \frac{8\pi}{3} r_e^2 \left| \sum_s \frac{g_s \omega^2}{\omega^2 - \omega_s^2 + i\gamma\omega} \right|^2 \qquad \textbf{1.11}$$

Although the simple semi-classical model gives a solution for the scattering of radiation by a multi-electron atom, the different interpretations of oscillator strengths are identical within the limitations discussed to that derived by modern quantum mechanical techniques. These limitations require that either the wavelength be large compared to atomic dimensions or the scattering to be in the forward direction, and it also that the photon energy be not too close to an atomic resonance, as that case requires an understanding of lifetimes (damping rates γ), which is not addressed by the semi-classical model[12]. In this very special case one can simultaneously satisfy the conditions that $\omega^2 >> \omega_s^2$ and $\lambda / a_0 >> 1$, so that the atomic scattering factor reduces to:

$$f\left(\Delta\boldsymbol{k}, \omega\right) \rightarrow f^0\left(\omega\right) \rightarrow \sum_s g_s = Z \qquad \textbf{1.12}$$

From Eq.-1.11;

$$f^0(\omega) = \sum_s \frac{g_s \omega^2}{\omega^2 - \omega_s^2 + i\gamma\omega} \qquad \textbf{1.13}$$

This can be written in terms of its complex components

$$f^0\left(\omega\right) = f_1^0(\omega) - i f_2^0(\omega) \qquad \textbf{1.14}$$

Considering the effect of several atoms, each containing many electrons in general this is a very complicated problem; however, if we restrict ourselves to propagation in the forward direction, the problem simplifies significantly, leading to relatively simple expressions for the refractive index. Indeed, it is the sum of forward-scattered radiation from all atoms that interferes with the incident wave to produce a modified propagating wave, compared to that in vacuum. The wave equation

$$\left(\frac{\partial^2}{\partial t^2} - c^2\nabla^2\right)\boldsymbol{E}_t(r,t) = -\frac{1}{\varepsilon_0}\frac{\partial \boldsymbol{J}_T(r,t)}{\partial t} \tag{1.15}$$

where $\boldsymbol{J}_T$ is the transverse component of the total current density and the subscript T denotes the direction transverse to k. The two possible transverse coordinates correspond to the two possible states of polarization. Eq.-1.15 is recognized as the transverse wave equation in the k, ω-space. After substituting the value of total current density contributing to the propagation in the forward direction and comparing with the standard form of the wave equation, the complex refractive index n can be written as:

$$n = 1 - \frac{n_a r_e \lambda^2}{2\pi}[f_1^0(\omega) - i f_2^0(\omega)] \tag{1.16}$$

where λ is the wavelength in vacuum. Further the refractive index for x-rays is very close to one, it is common to write it in the form $n=1-\delta+i\beta$, where delta (δ) and beta (β) are known as optical constants and in mathematical form

$$\delta = \frac{n_a r_e \lambda^2}{2\pi} f_1^0(\omega) \tag{1.17}$$

$$\beta = \frac{n_a r_e \lambda^2}{2\pi} f_2^0(\omega) \tag{1.18}$$

1.2.2. Absorption and Refraction:

From the knowledge of the refractive index, it is now convenient to consider phase variation and absorption during wave propagation. It is required to understand how the absorption coefficient μ is related to the refractive index that appears in the propagation of short wavelength electromagnetic radiation. To understand this a plane wave propagating in some material with an initial amplitude $\boldsymbol{E}_0$ is considered.

$$\boldsymbol{E}(r,t) = \boldsymbol{E}_0 e^{-i(\omega t - \boldsymbol{k}.\boldsymbol{r})} \tag{1.19}$$

The plane wave has complex dispersion relation and is given by:

$$\frac{\omega}{k} = \frac{c}{n} = \frac{c}{1-\delta+i\beta} \tag{1.20}$$

Substituting the value of k in Eq.-1.19 in the direction of propagation defined by $\boldsymbol{k}.\boldsymbol{r}=kr$, one get

$$\boldsymbol{E}(r,t) = \underbrace{\boldsymbol{E}_0 e^{-i\omega(t-r/c)}}_{vacuum\_propagation} \underbrace{e^{-i(2\pi\delta/\lambda)r}}_{\phi-shift} \underbrace{e^{-(2\pi\beta/\lambda)r}}_{decay} \tag{1.21}$$

where the first exponential factor is the phase advance, the second factor (containing $2\pi\delta r/\lambda$) represents the modified phase shift due to the medium, and the factor containing $2\pi\beta r/\lambda$ represents decay of the wave amplitude. To calculate the intensity of the wave for Eq.-1.21, the associated magnetic field must be determined and then to calculate the Pointing vector, the cross product of E and H need to be performed. The intensity I is given by:

$$I = I_0 e^{-\left(4\pi\beta/\lambda\right)r} \tag{1.22}$$

Eq.-1.22 suggests that the wave decays with distance r into the material with exponential decay length defined as:

$$l_{abs} = \frac{\lambda}{4\pi\beta} \tag{1.23}$$

1.2.3. Total External Reflection:

Figure 1.2 illustrates the incident, reflected, and refracted waves at a material interface. Here all angles are measured from the surface normal. Further from the Snell's law for a refractive index, neglecting absorption is $\sin\phi' = \sin\phi/(1-\delta)$:

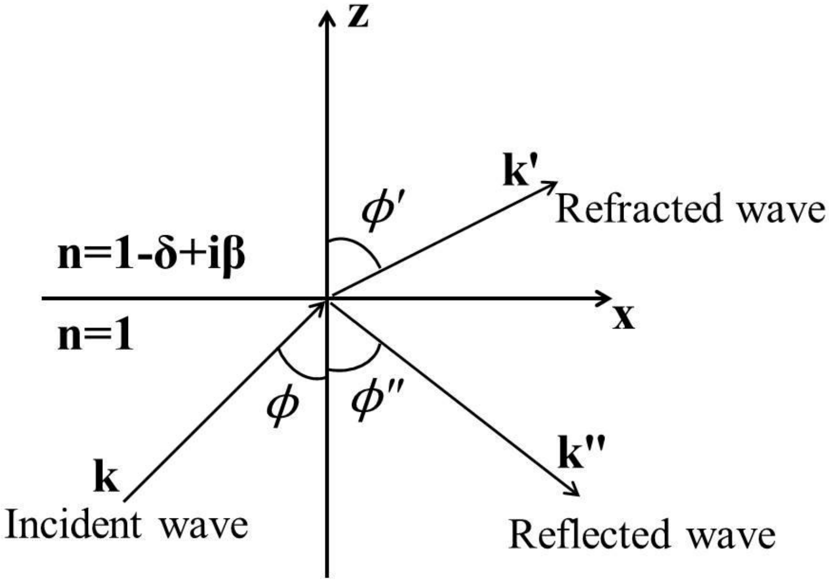

Figure 1.2: Interface geometry for incident, reflected, and refracted waves. Here the plane of incidence is defined as containing the incident wave vector k and the surface normal.

Thus the refracted wave is at an angle ϕ', somewhat further from the surface normal than ϕ because of the change in refractive index of the medium. As ϕ approaches π/2, sin ϕ' approaches to one somewhat faster. The limiting condition occurs at a critical angle of incidence, $\phi = \phi_c$, where $\phi' = \pi/2$, so that $\sin \phi' = 1$ and

$$\sin\phi_c = 1 - \delta \qquad \textbf{1.24}$$

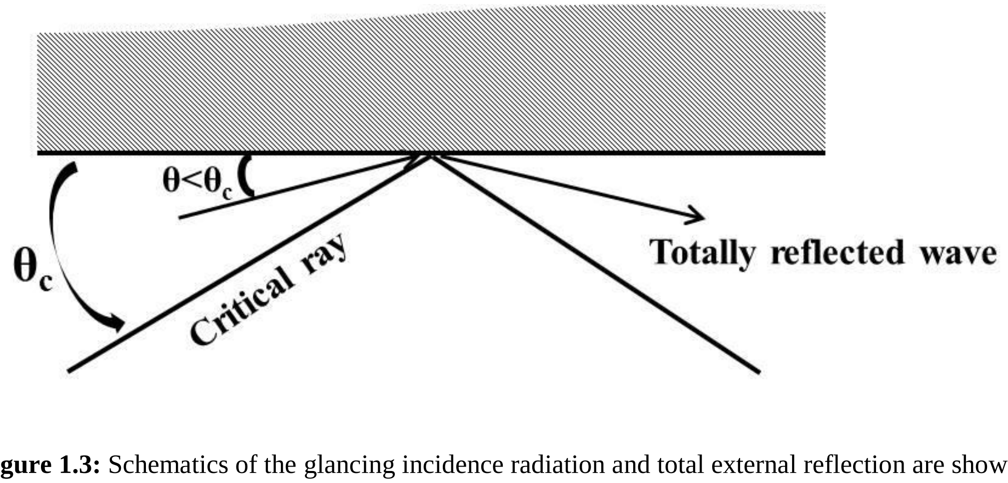

Figure 1.3: Schematics of the glancing incidence radiation and total external reflection are shown.

$$\sin\phi' = \frac{\sin\phi}{1-\delta} \qquad \textbf{1.25}$$

Eq.-1.24 is the condition for the total external reflection; the incident x-rays do not penetrate the medium and propagate along the interface at an angle $\phi' = \pi/2$. Since $\delta << 1$ for x-rays, the phenomenon occurs only for glancing angles where ϕ is near 90º. Thus it is convenient to introduce the complimentary angle θ, measured from the interface, where $\theta + \phi = 90º$. The critical angle θ_c comes out:

$$\theta_c = \sqrt{2\delta} \qquad \textbf{1.26}$$

1.2.4. Techniques to Determine Optical Constants:

The most commonly used techniques for the determination of optical constants in soft x-ray/EUV region are reflection and transmission. There are several other techniques such as ellipsometry, interferometry, photoemission and total electron yield method, which are also used to determine optical constants with certain limitations. The ellipsometry technique is useful only for energy range <35 eV. Above this energy range there is a technical limit in producing a good polarizer. Similarly the electron energy loss spectrometry is good for low energy range <30 eV. Each technique has their own limitations and none of them can be used for determination of optical constants for complete spectral range. Below some techniques used to determine the optical constants in soft x-ray/EUV region are explained in brief.

1.2.4.1. X-ray Reflectivity:

In the x-ray reflectivity technique, the reflected photons are measured from the smooth surface of a sample as a function of incidence angle. In this technique, the incident beam needs to be monochromatic, collimated and polarization should be well defined.

Angle versus reflectivity data are measured for a fixed wavelength λ. Measured data are analyzed by means of the Fresnel reflectivity formula as defined below:

$$R_s = \frac{\left|\cos\phi - \sqrt{n^2 - \sin^2\phi}\right|^2}{\left|\cos\phi + \sqrt{n^2 - \sin^2\phi}\right|^2} \qquad \textbf{1.27}$$

$$R_p = \frac{\left|n^2\cos\phi - \sqrt{n^2 - \sin^2\phi}\right|^2}{\left|n^2\cos\phi + \sqrt{n^2 - \sin^2\phi}\right|^2} \qquad \textbf{1.28}$$

where R_s and R_p are the reflectivity for s and p- polarized light respectively and ϕ is the incidence angle from the normal. Effect of surface roughness is taken into account using Nevot-Croce model[13]. Optical constants (both delta and beta) are determined by fitting of reflectivity data.

1.2.4.2. X-ray Transmission:

In this technique, intensity of incident and transmitted beam is measured. Figure 1.4 shows the schematics of transmission measurements. For sample of known thickness *r*, the transmitted intensity is given by:

$$T = \frac{I}{I_0} = e^{-\rho\mu r} \qquad \textbf{1.29}$$

where ρ is the mass density, I is the transmitted flux, I_0 is the incident flux and μ is the mass absorption coefficient. Beta is determined from the mass absorption coefficient ($\mu=4\pi\beta/\lambda$). With the knowledge of absorption data, the real part δ can be determined using Kramers-Kronig relations discussed below (in section 1.2.5). The Kramers Kronig integration is performed in whole energy range, which is not possible in practical situations. In the practical case several interpolation/extrapolation functions are used, which generate significant error in the data.

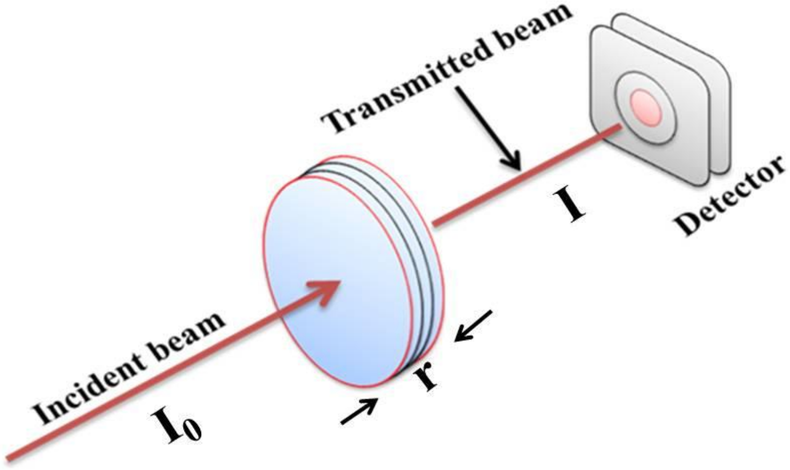

Figure 1.4: Schematic of the transmission measurements.

1.2.4.3. Interferometry:

This technique is used in the hard x-ray energy region. In this technique, the incident beam is passed through the sample of thickness *r*, phase shift ($\Delta\phi$) in the incident beam is produced and is measured from the interference fringes. The value of δ is obtained from the relation:

$$\Delta\phi = \left(\frac{2\pi\delta}{\lambda}\right) \times r \qquad \mathbf{1.30}$$

The incident beam is divided into two parts using the beam splitter, one part passes through the sample and the other is used as a reference beam. The interference fringes are formed from the recombination of these two beams. The phase shift $\Delta\phi$ is obtained from the interference pattern using Eq-1.30. This technique is very difficult to use in the soft x-ray energy region, because it is very difficult to make suitable beam splitter to produce a flat wave-front in soft x-ray region.

1.2.4.4. Ellipsometry:

In the ellipsometry technique[14], the change in polarization state of the incident beam is measured upon reflection from the sample. Because of difference in Fresnel reflection coefficient for s- and p-polarized light, the linearly polarized light after an oblique reflection becomes elliptically polarized. The refractive index is derived from the measurement of the polarization ellipse. This technique is highly surface sensitive and is used to determine the film thickness and the complex dielectric constants simultaneously. The technique requires high flux and a high degree of polarization. With the availability of the synchrotron radiation sources, which are highly polarized, this technique can be applied in the < 35eV energy region.

1.2.4.5. Electron Energy Loss Spectrometry:

In this technique,[15] the electrons of few hundred kilo electron volt energy (50 – 300 keV) pass through a thin sample. The schematic of the measurement geometry is shown in Figure 1.5.

The inelastic scattering processes inside the sample lead to change in energy and momentum of the electrons, which are the measurable quantities. Since the differential scattering cross section $d\sigma$ for an electron which loose δE energy while it scatters into a differential solid angle $d\Omega$ at an angle θ is given by[16].

$$\frac{d^2\sigma}{d\Omega dE} = \left(\frac{e}{\pi\hbar v^2}\right)^2 \operatorname{Im}\left(\frac{-1}{\tilde{\varepsilon}}\right)\frac{1}{\theta_E^2+\theta^2} \qquad \textbf{1.31}$$

$$\theta_E = \frac{\Delta E}{2E_0} \qquad \textbf{1.32}$$

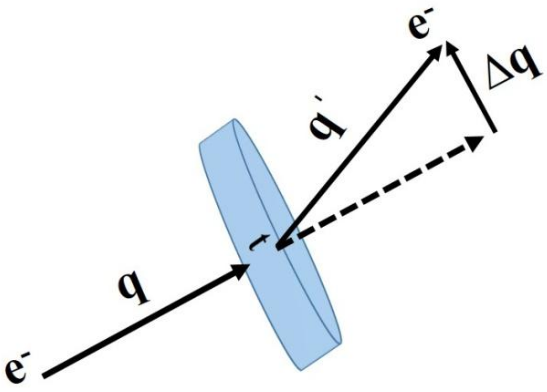

Figure 1.5: The vector diagram of the electron scattering in a film of thickness t.

where, ΔE is the energy loss by the electron and $\mathrm{Im}(-1/\tilde{\varepsilon})$ is the loss function, which is measured. From the Kramers- Kronig analysis of the loss function, real part is determined. This technique can be used to determine the optical constants in <30 eV energy range. In the high energy range multi electron scattering dominates, which in turn creates complications.

1.2.4.6. Total Electron Yield:

Total electron yield (TEY) method is used in the X-ray region to determine the optical constants of thin film/multilayers. In this technique, the electron yield is measured. Pepper et al.[17] explained that the optical constants of thin films can be determined from the TEY spectra. For thin films the yield intensity *(Y)* is given by:

$$Y = C\int_0^d e^{-\frac{y}{L}}\eta(y)dy = CF(y) \qquad \mathbf{1.33}$$

where L is the attenuation length of the photoelectrons, C is a parameter that takes into account the probability of absorption of photons by electrons; $\eta(y)$ is the number of photons absorbed per unit volume divided by the number of incident photons in the unit area of the surface where radiation is incident. Ejima et al.[18] extended the single layer model to multilayer model by introducing different transmission rates for the interfaces and attenuation length for different layers. With the assumptions that the absorption is very less and the thickness of the top most layer is much higher than the attenuation length the electron yield intensity I_m of m^{th} layer[19] is found to be proportional to:

$$I_m \approx I_{top}\{1+|R_{m-1}|^2 + R_{m-1}\cos(\delta_{m-1} - k'_m(d_m + L_m))\} \quad \textbf{1.34}$$

where I_{top} is the yield intensity of the topmost layer R_{m-1} is the reflection coefficient of the $(m\text{-}1)^{th}$ layer which can be obtained from the reflection spectra. The term $\{\delta_{m-1}\text{-}k'_m\,(d_m+L_m)\}$ is the TEY phase. As the thickness of the topmost layer changes, the TEY phases also change. By subtracting these two TEY phases, one can get rid of the reflection phase term and the attenuation length phase term. Thus the real part of the refractive index *Re (n)* can be obtained from:

$$\mathrm{Re}(n) = \frac{k'(0^\circ)\lambda}{2\pi} = \frac{2k'(0^\circ)\lambda\Delta d}{4\pi\Delta d} \quad \textbf{1.35}$$

The extinction co-efficient i.e. the imaginary part of the refractive index can be obtained from:

$$\mathrm{Im}(n) \propto \eta(y) L_m \frac{\lambda}{2\pi} \quad \textbf{1.36}$$

From this technique the optical constants of the top most layers can be obtained, but it gives inaccurate results for the bulk because this technique is highly surface sensitive.

1.2.5. Kramers Kronig relations:

In principle δ and β for all the materials can be determined from absorption and phase shift measurements, as discussed above. The β is determined using transmission measurements. However, determining δ is more problematic, particularly for soft x-rays, because interferometry is not sufficiently advanced. The $f_2^0(\omega)$ is determined from the absorption measurements of thin foils (or gases) of elements of interest in a broad range of photon energies. This can be done with the availability of broadly tunable SR sources and a suitable monochromator. From the transmission measurements, the macroscopic mass absorption coefficient $\mu(\omega)$ can be determined. The real part of the atomic scattering factor $f_1^0(\omega)$ is then determined through mathematical relationships between $f_1^0(\omega)$ and $f_2^0(\omega)$, generally referred as Kramers–Kronig relations[20,21,22,23].

$$f_1^0(\omega) - Z = -\frac{2}{\pi} P_c \int_0^\infty \frac{u f_2^0(u)}{u^2 - \omega^2} du \qquad \mathbf{1.37}$$

where Z is the atomic number of the element. Further if one can determine the delta from using phase angle from reflectivity versus wavelength spectrum, $f_2^0(\omega)$ can be determined from:

$$f_2^0(\omega) = \frac{2\omega}{\pi} P_c \int_0^\infty \frac{f_1^0(u) - Z}{u^2 - \omega^2} du \qquad \mathbf{1.38}$$

Eq.-1.37 and 1.38 provides the desired integral relationship between real and imaginary parts of the atomic scattering factors and are known as Kramers Kronig relations. The accuracy of the experimental data for $f_2^0(\omega)$ can be examined by the sum rule defined as:

$$Z = \frac{2}{\pi} \int_0^\infty \frac{f_2^0(u)}{u} du \qquad \mathbf{1.39}$$

where $f_2^0(u)/u$ is the oscillator strength associated with the frequency u in the region of $(0, \infty)$. Further for the materials with absorption threshold well separated in energy so that the oscillator strength of one absorption region is exhausted before the onset of the next, a partial sum rule may be used which is defined as:

$$Z - \frac{2}{\pi} \int_\omega^\infty \frac{f_2^0(u)}{u} du = N_{eff}(\omega) \qquad \mathbf{1.40}$$

Here N_{eff} represents the effective number of electrons in the atom contributing to the absorption, i.e., having binding energy less than the photon energy. Thus from the above expression of partial sum rule, it is clear that $N_{eff} = Z.N_{eff}(\omega)$.

1.3. Structural Properties:

The structural properties of the thin films depend on deposition method as well as deposition parameters. The optical properties of thin films are effected due to both structural (amorphous and crystalline, crystalline size, film density etc.) and chemical effects (doping and film stoichiometry)[24]. The optical properties can be described by the most important physical quantity known as refractive index. Furthermore for thin films and nanomaterials, the refractive index values are sensitive to microstructure and are influenced by various factors such as surface/interface structure, crystal quality, lattice parameters, lattice strain, defect structure and chemical composition[25].

In literature several reports are available where the effects of structural parameters on optical properties are studied. Das et al.[26] have shown that change in crystalline state of Al_2O_3 film is responsible for change in optical behavior in the soft x-ray energy region. They have compared optical constants of amorphous Al_2O_3 and sapphire crystal. Similarly Wang et al.[27] have shown that the optical properties of TiO_2 changes significantly with the change in crystalline state. Further significant change in the optical properties of gallium oxide thin films is reported due to change in structural properties by Ramana et al[25].

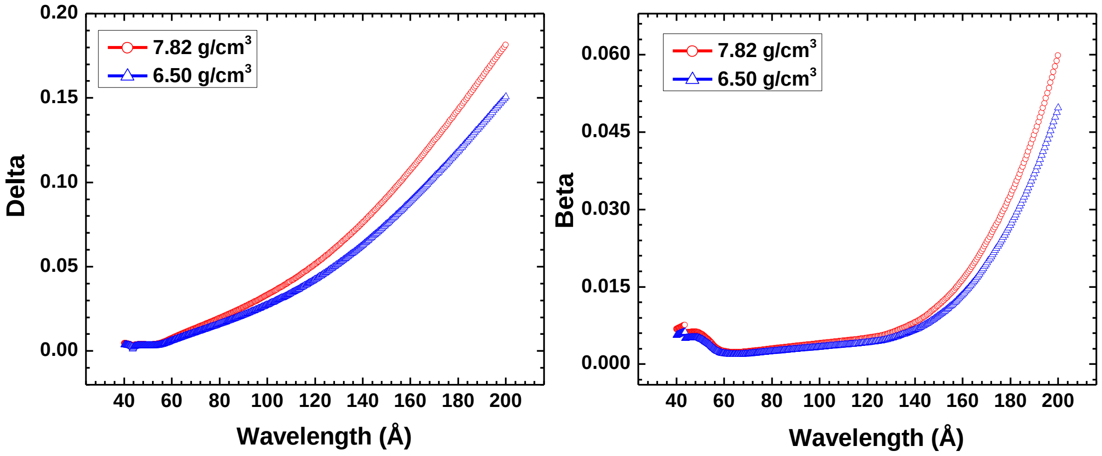

Figure 1.6: Effect of density on the optical constants of NbC is shown. It is clear that a decrement of about 15 % in density affects the optical constants significantly.

As an example Figure 1.6 shows the optical constants of NbC in the 40-200 Å wavelength region. It is clear that a decrement in the density (about 15%) significantly affects the optical constants, suggesting that the structural parameters need to be optimized and determined.

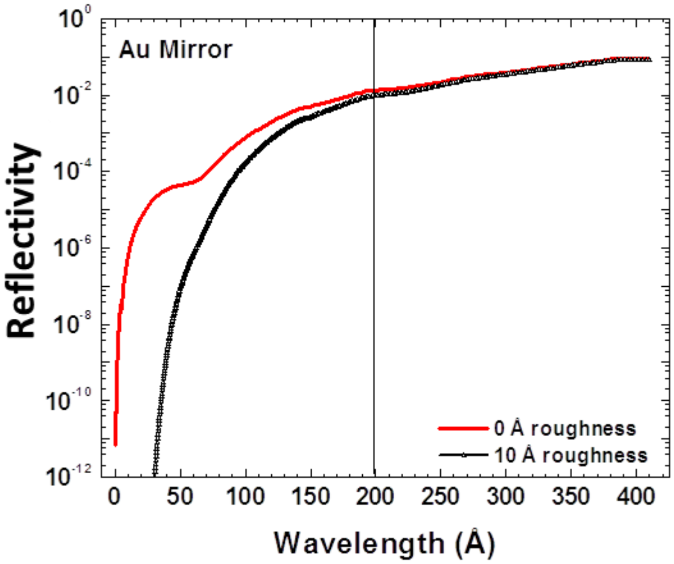

Figure 1.7: Effect of surface roughness on Au thin film mirror. Reflectivity of Au mirror drops significantly with surface roughness of 10 Å.

Further the surface and interface roughness significantly affect the reflectivity performance of thin film/multilayer mirror as shown in Figure 1.7. From Figure 1.7 it is clear that a surface roughness of 10 Å deteriorates the reflectivity profile of Au mirror prominently below 300 Å wavelength. The imperfect surfaces are of two categories, 1) low frequency roughness and 2) high frequency roughness. The low frequency roughness enlarges the half width of the focal spot and is also called figure error, while the high frequency roughness creates diffuse scattering. The scattering background deteriorates the image contrast. The above discussion suggests that the effect of structural disorder on optical properties of thin films need to be investigated. In the present work structural properties of NbC and ZrC thin films are carried out.

1.4. Scope of Present Work:

In literature Mo/Si multilayer is reported as best candidate for high reflectivity performance near Si L- edge and is the most promising reflective coating for extreme ultraviolet (EUV) lithography applications near 130 Å wavelength. Similarly Zr/Al multilayer is used as a reflective coating for EUV applications near Al L- edge. But these elemental multilayers pose a severe problem in regard to high chemical reactivity among the constituent elements. In Si based multilayers (e.g. Mo/Si, W/Si, Nb/Si etc.), silicide formation is a common problem, when they are used at elevated temperatures in high heat load environment. Similarly Al based multilayers, such as Zr/Al are thermally unstable above 200°C[28,29] and later intermixing and formation of Al-Zr alloy starts. Recent development of free electron laser sources[30,31] generating ultra-short EUV pulses have posed new challenges for x-ray optical elements. X-ray pulses of very high brightness stimulate radiation induced damage in optical elements[32,33]. The emerging technology requires improved and stable optical elements[34,35]. To overcome this difficulty a barrier layer (of carbon, B_4C etc.) is deposited in between low Z and high Z materials. However, inserting an extra layer leads to a phase variation in the waves reflecting from different interfaces at the Bragg condition and thereby the resultant phase mismatch reduces the reflectivity performance. Moreover, the barrier layer should be ultra-thin in order to minimize the phase mismatch which requires a stringent deposition control. As a solution to intermixing, compound materials are used in multilayers mirrors, because the optical constants of compound materials are very similar to those of corresponding elements in soft x-ray energy region[36]. A. F. Jankowski et al. have shown W/B_4C multilayer to be a more thermally stable combination in comparison with W/C multilayers[37]. Recently, NbC/Si multilayer is proposed for extreme ultraviolet (EUV) applications[38], where NbC (metal carbide) layers are non-stoichiometric[39,40] and have a significant amount of unreacted carbon. The presence of unsaturated carbon in the near vicinity of metal species (Nb, Mo, Zr etc.) may act as a barrier layer for Si or other elements to prevent the chemical intermixing. The NbC/Si multilayer is found to be thermally stable up to 700°C, without significant loss in the reflectivity performance. Similarly theoretical calculation suggests that ZrC/Al may be a better choice than Zr/Al multilayer.

Figure 1.8 shows the reflectivity calculations carried out for NbC/Si and Mo/Si using identical structural parameters and for ZrC/Al and Zr/Al as well. It is found that the theoretical reflectivity for Mo/Si and NbC/Si multilayer remains close with each other similarly for ZrC/Al and Zr/Al it remains the same. In order to use compound materials in actual applications, the structural and optical properties of their thin films must be investigated in detail. When thin films of a compound material are formed, the structural properties get modified[36], growth related atomic rearrangement affect the chemical stoichiometry and that in turn affects their optical properties[41]. Hence the structural properties of thin films of such compound materials must be investigated.

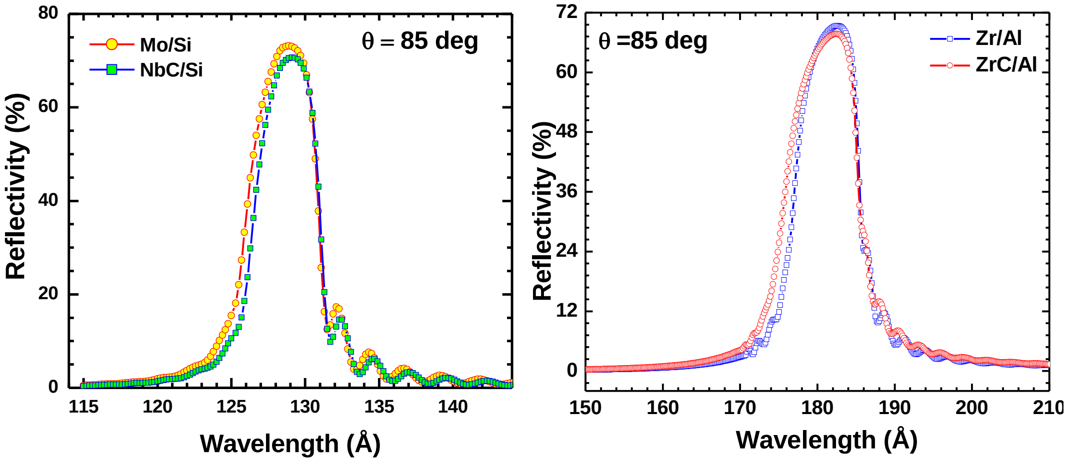

Figure 1.8: Calculated soft x-ray reflectivity profile of Mo/Si and NbC/Si multilayers on the left panel with identical structural parameters (d = 63 Å, Γ = 0.428, σ = 3 Å, N = 51 layer pairs) at 85.0° incidence angle [38]. Similarly on the right panel calculated reflectivity profile of Zr/Al and ZrC/Al multilayers with identical structural parameters (d = 97.3 Å, Γ = 0.35, σ = 5 Å, N = 60 layer pairs) at 85.0° incidence angle are shown.

Further in order to predict the performance of compound multilayer and to use compound material in soft x-ray optical elements, precise knowledge of optical constants is required. Earlier several techniques have been used to determine the optical constants, such as transmission, photoemission, angle dependent reflection, angle dependent electron yield, interferometry and ellipsometry. Optical constants from a variety of sources are compiled in ref.[42,43] Henke et al.[42] have used photo absorption data for the determination of atomic scattering factor for all elements having atomic number Z= 1-92 in the energy range 50 to 30,000 eV. They have applied Kramers-Kronig relation to determine real part of refractive index from the absorption data. However, there are discrepancies among the data reported by different authors on the same material, because the determination of optical constants is subjected to a number of inherent difficulties in the soft x-ray/EUV energy region. For example, the high absorption is prominent in the regions above absorption edges, which prevents reliable transmission measurements unless free standing ultrathin films are fabricated and a x-ray source of high photon flux and spectral purity is available. Further the Kramers– Kronig integrals used for determination of δ from the transmission data, should be calculated over frequency range of zero to infinity. The practical limitation of generating absorption data for infinite range introduces certain errors in real part of refractive index, if calculated by Kramers-Kronig method. Furthermore, in case of reflectivity, smooth and flat surfaces are required. The presence of surface roughness would cause significant amount of the reflected signal to be scattered in non-specular directions, resulting in poor reflectivity curves.

In case of compound materials, optical constants are calculated by taking a weighted sum of the optical constants of constituent atoms using Henke's database. This approach works well for photon energies away from the absorption edges of the constituent elements. In the close vicinity of an absorption edge this approach fails as the formation of chemical bonds leads to shift in absorption edge data. In general, overlapping of electron wave functions of the constituents of compound material modifies the optical constants. Various experimental studies carried out earlier show significant variation in experimentally measured optical constant values from those obtained using Henke's tabulation for different compound materials. Rao et al.[44] have shown large deviation (~50%) in optical constants of InP in 50-200 Å wavelength region. This large deviation has been attributed to change in near neighbor environment in compounds. Similarly Ksenzov et al.[45] found a large mismatch in optical constants of B_4C near boron absorption edge. They used B_4C compound material in Ru/ B_4C multilayer system. They explained this large deviation near boron edge on the basis of change in chemical composition. Fragmentation and segregation of constituent elements from compound materials are responsible for significant variation in optical constant values. In an earlier reported study on optical constants of ZnS[46] it was shown that sulphur got segregated towards the surface of the film and that caused a big deviation in the experimentally determined values from those of the bulk. Similarly, crystalline and amorphous state of a film is also responsible for a change in optical behavior. A study on sapphire crystal and amorphous Al_2O_3 revealed a large deviation of 28-30% in the values of optical constants in wavelength range away from Al L-edge[26]. All these studies suggest that the experimental investigation of optical constants of compound materials is a prerequisite before their use in optical devices.

Further, surface contamination on x-ray optical elements seriously affects the optics performance. Carbon contamination and hydrocarbon cracking on optical elements in soft x-ray spectrometers and synchrotron radiation beamlines is a severe problem. Simulations suggest that a 10 Å thick carbon layer reduces relative reflectivity of a single multilayer optical surface by 1.4%, because of high absorption of EUV radiation by carbon which makes this contamination layer a serious source of the loss of throughput[47]. Extreme ultraviolet lithography (EUVL) scanner optics typically consists of ten such reflecting layers, where the total throughput deteriorates drastically. As a remedy, the optical elements need to be replaced periodically[48]. Since these optical elements are very costly, hence disposal of the surface contaminated mirrors is not a viable solution. So it is desirable to develop a technique for periodic removal of the carbon contamination without damage or modifications of the surface underneath[49,50,51]. In this work to remove the surface contamination from x-ray optical elements, a laser based cleaning technique is deployed successfully.

The materials under investigation in this work are NbC and ZrC. The goal of this thesis is to construct an accurate, self-consistent set of values for the optical constants of these compound materials in a wide energy range. Structural and optical properties are investigated in this work and explained in detail. Chapter 2 gives an outline of the instruments utilized for the measurements and describes their capabilities. In Chapter 3, structural and optical investigation on NbC thin films are explained. In Chapter 4, structural and optical investigation on ZrC thin films are explained. In Chapter 5, the surface contamination effects on optical properties and removal of surface contamination are explained. Finally in Chapter 6 the summary of whole work and future direction is discussed.

Chapter 2.

Experimental Techniques

In this chapter, details of the Reflectivity beamline, including a brief introduction of Indus-1 synchrotron source are described. Results of higher harmonic contamination study for Reflectivity beamline are discussed. Several other experimental techniques used in the present thesis are discussed.

2.1. Introduction:

The electromagnetic radiation has been used for the study of chemical and physical properties of the materials from last many years. The visible light gives the direct information of sizes, colors etc. at macroscopic levels and has been used extensively. With the advent of x-rays and the associated technologies it has become possible to understand physical phenomena even at the atomic scale. Due to the limitations in technology, a portion of electromagnetic radiation was left unused in the soft x-ray/EUV region (10Å < l < 1000Å). With emergence of ultra-high vacuum (UHV) technology, attention of researchers has been drawn towards the soft x-ray field. Since last three decades, the experimental activities in this region have been increased enormously.[52] With the development of multilayer thin film technology, near normal incidence optics has become viable[53] that has given a new dimension to imaging devices. With the availability of the synchrotron radiation sources, the field has further revolutionized. Problems particularly associated with the soft x-ray tube sources, as insufficient brightness, limited wavelength coverage and no tunability, have reduced. Dedicated soft x-ray reflectivity beamlines have been setup on various SR facilities[54,55]. In India, a 450 MeV electron storage ring, Indus-1, provides VUV/ soft x-ray radiation[56]. The quasi- continuous SR light, emitted from this storage ring, extends from far infra- red to soft x-ray region with a critical wavelength of 61 Å. A reflectivity beamline (BL-4) facility for the characterization of x-ray optical elements is available. Beamline has wide energy coverage (10 eV to 300 eV) and can be used for multipurpose applications.

To study various physical and chemical properties of the materials by means of different experimental techniques like x-ray reflectivity, photoelectron spectroscopy, photo absorption etc.

different beamlines are available in Indus-1. In this chapter the beamline used for soft x-ray reflectivity measurements and other experimental techniques are described in details.

2.2. Synchrotron radiation source:

In conventional lab sources, the x-rays are emitted by the bombardment of accelerated electrons on a target material. It gives an intense characteristic radiation superimposed on a continuum bremsstrahlung. In conventional x-ray sources, the intensity is limited by the power density exerted by an impinging electron beam, though by cooling and rotating the target, power density can be increased by an order of magnitude. Emitted radiations from these sources are un-polarized, and the intensity available is also not sufficient for many experiments. Due to the isotropic emission over a large angular range, the intensity falls rapidly as one goes away from the source. Shortcomings of laboratory based x-ray sources have been overcome in synchrotron sources where the circulating charged particles emit the electromagnetic radiation upon the centripetal acceleration in a strong magnetic field of a storage ring device. The radiation emitted by the relativistic electron beam circulating with ~GeV energy is seen in a narrow search light cone, in the forward direction of a laboratory frame. Due to bunching of the electron beam in a storage ring, the emitted SR light has a time structure. Further, SR radiation is highly polarized in the plane of electron orbit. Wavelength tunability is possible from far infrared to x-ray region. The unique features of synchrotron radiation are as follows:

- ✓ High flux: orders of magnitude higher than the lab sources.
- ✓ Wavelength tunability from far infrared to x-ray region which is not possible in any other sources.
- ✓ Time structure: pulse duration of Pico second width.
- ✓ Highly polarized in the plane of electron orbit.

- ✓ Highly collimated with a few mrad vertical divergence.
- ✓ It is also considered as a standard radiation source due to well-defined characteristic features.
- ✓ SR machine operates in UHV environment thus offers the best possible cleanliness.

In x-ray reflectivity experiments, the reflectivity decreases rapidly as a function of incident angle. This fall is inversely proportional to fourth power of the momentum transfer vector $(q=4\pi \sin\theta/\lambda)$, where θ is the incidence angle and λ is the wavelength. To measure the x-ray reflectivity over a large angular range, a high intensity incident beam is required. A typical x-ray reflectivity experiments covers 6-7 order changes in intensity. Wavelength tunability is required to perform the reflectivity experiments at different wavelengths, which depends on the absorption threshold of the material. For exploring the polarizer mirrors, the known polarization state of an incident beam is a useful feature.

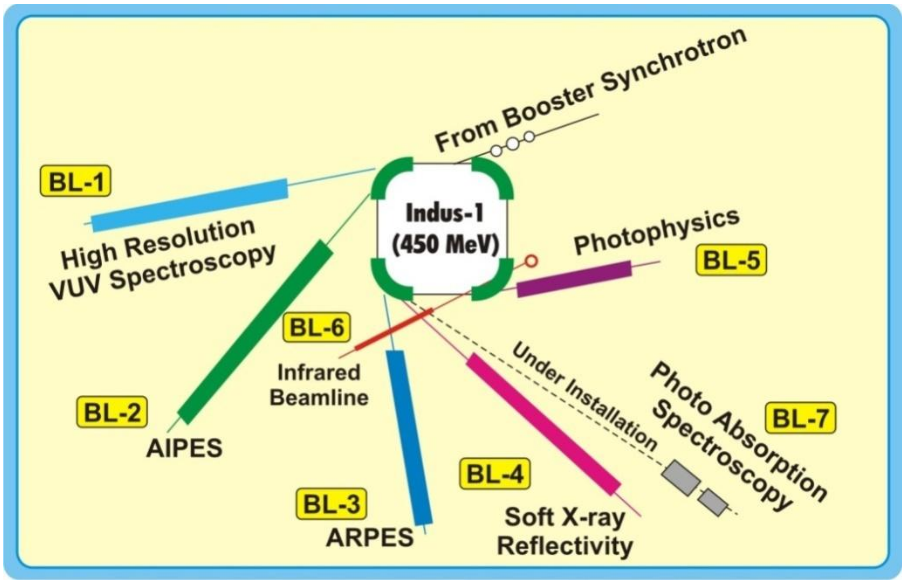

Figure 2.1: Schematic of Indus-1 experimental hall. Locations of different beamlines are shown. BL-4 is the reflectivity beamline, which is described in this chapter.

2.2.1. Indus-1:

In Figure 2.1, the layout of Indus-1 synchrotron source along with associated beamlines is shown. Indus-1 is a 450 MeV electron storage ring. It produces continuous electromagnetic radiation in soft x-rays to infrared region, where critical wavelength is 61Å (λ_c) that divides the power spectrum on wavelength scale in two equal parts and is defined by the relation:

$$\lambda_c(\AA) = \frac{18.64}{E^2(GeV) \times B(T)} \qquad \textbf{2.1}$$

The circumference of Indus-1storage ring is 18.96 meter which accommodates the four bending magnets of 1.5 Tesla field. The radiating electron beam, which loses the energy, is powered by a radio frequency cavity of 31.619 MHz. The two electron bunches of the length 11.3 cm revolve with the frequency of 15.82 MHz. The characteristic features of Indus-1are given in Table 2.1.

Table 2.1: Parameters of Indus-1 synchrotron radiation source.

Electron energy	450 MeV
Beam Current	100 mA
Beam lifetime	1.8 Hr.
Bending magnet field	1.5 Tesla
Critical wavelength	61.38 Å (202 eV)
Circumference	18.96 m
Electron bunch length	11.3 cm
Photon flux @ λ_c	7.2×10^{11} photons/s/mradhoriz. 0.1%BW
Brightness	3.1×10^{12} photons/s/mm^2/mrad^{2}0.1%BW

2.3. Beamline:

Beamline is an optical device, which plays an important role in the utilization of SR sources. It interfaces the synchrotron machine with the experimental station. Beamline optics provides a monochromatic beam from the quasi-continuous SR radiation. The photon beam intensity and the energy resolution are the main characteristic parameters of beamline. The design of a beamline depends on experimental requirements, for example the reflectivity experiments need a high flux and a moderate energy resolution, whereas the experiments of photoelectron spectroscopy require a high resolution in photon energy for mapping the energy bands in solids. Other influencing factors are radiation safety, sizes of vacuum hardware, fixed beam exit, beam spot etc., thus the configuration of a beamline varies as per the requirement of the experimental station. In soft x-ray region there are no transmission media except the vacuum. The refractive index for all materials is close to unity thereby the transmission optics is not applicable. Reflection optics is other alternative, which gives a considerable flux at extreme grazing angles, although, the grazing incidence geometry needs large size mirror, as footprint of a beam is large. To generate the big optics with a minimum figure error over a large area is a technological challenge and that increases the cost significantly. The SR beamline consists of a state of art technology in the optics as well as in the ultra-high vacuum field. To study various physical and chemical properties of the materials by means of different experimental techniques like x-ray reflectivity, photoelectron spectroscopy, photo absorption etc. different beamlines are available in Indus-1. In the following section the soft x-ray reflectivity beamline is described.

2.3.1. Reflectivity Beamline:

The Reflectivity beamline provides monochromatic photons in the range of 40Å to 1000Å.[57] It is one of the first beamline, commissioned on Indus-1 source. The beamline is installed on bending magnet port of 50° where the size of circulating electron beam in storage ring is 0.8 mm × 0.1 mm (horizontal × vertical). The acceptance angle of beamline is 10 mrad× 5 mrad.

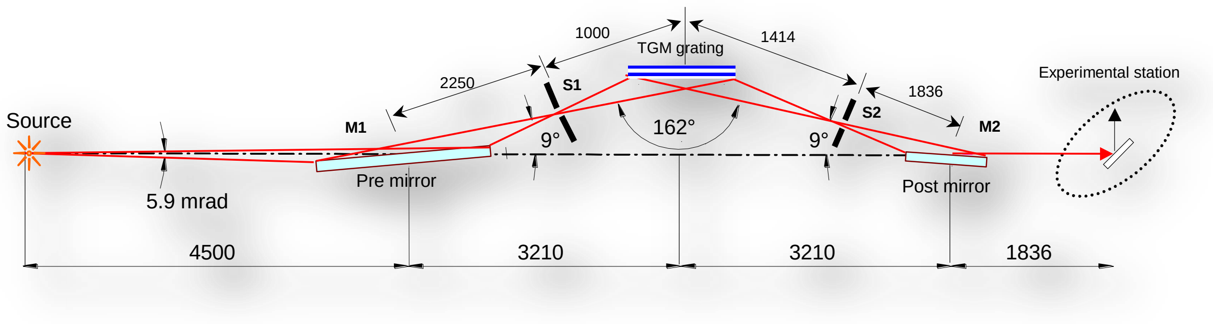

Figure 2.2: Optical layout of the Reflectivity beamline consists of pre and post focusing mirror and a TGM monochromator.

The optical layout of the Reflectivity beamline is shown in Figure 2.2. The first optical element that images the source on entrance slit S1 of the monochromator is gold-coated toroidal mirror (M1). The mirror M1 de-magnifies the source in ratio of 2:1. The angle of incidence chosen for M1 is 4.5°, which is sufficiently small to give the best possible reflectivity at lower part of the wavelength range. For the monochromatization of the synchrotron radiation in the wavelengths range of 40-1000Å, three holographically made gold-coated toroidal gratings with different groove density are used. Three respective gratings have a different groove density of 1800, 600, and 200 line/mm respectively to get the monochromatic photon in three different range of 40-120Å, 120- 360Å and 360-1000Å. Gratings are interchangeable in situ without breaking the vacuum. They accomplish the dual task of focusing as well as the monochromatization. The constant deviation angle of 162° from a toroidal grating followed by a reflection from post mirror maintains the exit beam in a horizontal plane. The resolving power i.e. $\lambda/\Delta\lambda$ of the monochromator lies in the range of 200-500, which depends upon slit S1 and S2 opening. Both the entrance and the exit slits are variable in 0 to 1.8 mm with a resolution of 1mm in the vertical direction. The monochromatic image of the source at exit slit S2 is focused by vertical deflecting toroidal mirror M2 on the sample position in a reflectometer station. The demagnification ratio for mirror M2 is 1:1 that gives approximate beam size of ~1mm × 1mm at the focus point. The grazing angle of incidence is 4.5° for mirror M2 also. The monochromatic focused beam coming out of beamline is in horizontal plane. All the parameters for beamline are given in Table 2.2.

Table 2.2: Parameters of Reflectivity beamline.

Wavelength range	40-1000 Å
Monochromator Type Grating-1 (40 Å-120 Å) Grating-2 (120 Å-360 Å) Grating-3 (360 Å-1000 Å)	TGM 1800 groove/mm 600 groove/mm 200 groove/mm
Resolving power ($\lambda/\Delta\lambda$)	200-500
Photon flux	~ 10^{11}
Mirror M1 and M2	Toroidal, gold coated
Beam size at experimental station	~ 1 mm × 1 mm

The experimental station at Reflectivity beamline is a high vacuum reflectometer, which can be used for variety of experiments like optical studies, mirror performance testing, reflectivity measurements of thin film multilayer mirrors, efficiency testing of the soft x-ray gratings etc. X-ray reflectivity, particularly in soft x-ray / VUV region, requires a high precision rotation motion of the sample and detector over a large angular range, where the angular motions are to be carried out in a vacuum environment. The vacuum of experimental station and beamline must be compatible with each other as no vacuum isolation windows are available for soft x-rays. The beamline operates in UHV environment, so the experimental station must be either UHV compatible or it need to be connected with the beamline by using a properly designed differential pumping device. The differential pumping device takes care of vacuum mismatch between reflectometer and beamline. The goniometer assembly of the reflectometer comprises two rotary stages and one linear stage. The two rotary stages can be moved in coupled and uncoupled mode to carry out different modes of reflectivity, such as detector scan, rocking curve scan, θ-2θ scan, and so forth. The linear stage is employed to bring the sample in and out of the direct beam to facilitate the direct beam monitoring. This feature is useful for normalization of reflectivity data with incident beam intensity. Sample and detector can be aligned with a precision of 0.01°. A soft x ray silicon photo diode detector (IRD, USA) with 100% internal quantum efficiency[58] is used to monitor the reflected beam intensity. The current output of the detector is recorded using a Keithley 6514 picoammeter.

2.4. Quantitative Analysis of Higher Harmonics:

The undesired photons of higher harmonics are a common characteristic and are an intrinsic problem in synchrotron beamlines, which makes the analysis of experimental data quite complicated. In the Reflectivity beamline, provisions are made to suppress the higher diffraction order contamination coming from grating[3] to maintain the spectral purity of a monochromatic beam. Therefore just after the slit S2, different edge filters are mounted like Silicon, Aluminum, Tin, Boron, Carbon, and Indium. These are transmission filters of 1000 to 1500Å thick foils mounted on 87% transmitting nickel mesh. Any one of these edge filters can be introduced in SR path.

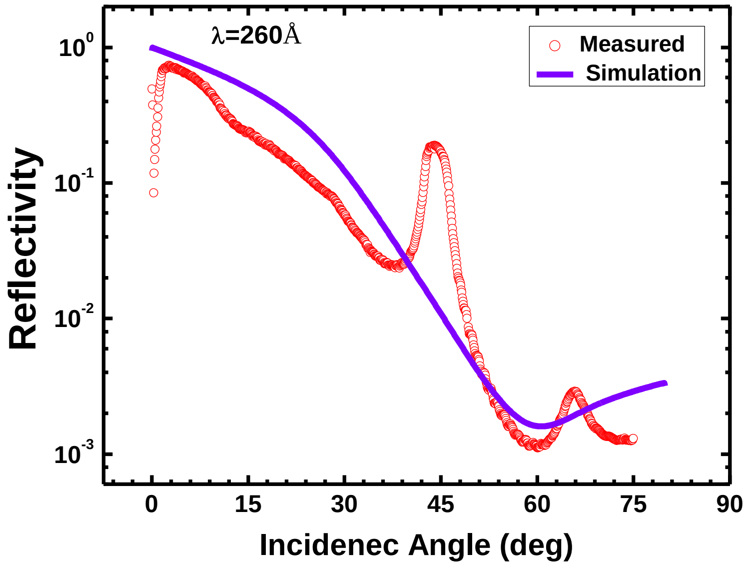

Figure 2.3: Open circle shows the measured SXR curve of the Mo/Si multilayer using λ = 260 Å. Continuous line represents the simulated SXR spectra for the same wavelength and using the multilayer parameters obtained from the GIXR analysis.

These filters work near the absorption edges of the filter materials. In order to minimize the artifacts of higher harmonics in experimental data the spectral purity of the grating based beamlines need to be determined. In this work higher harmonic contamination from the TGM are analyzed using a Mo/Si multilayer of d=97 Å, N=60 layer pair[59]. SXR reflectivities are calculated for incident wavelength λ and its second harmonic λ/2, and its third harmonic λ/3 using the predetermined structural parameters of the multilayer. The fractional composition of the reflectivity data corresponding to the three wavelengths λ, λ/2, and λ/3 are varied to get the best fit of the measured SXR data, and that in turn gave the fractional composition of the harmonics present. Figure 2.3 shows the measured SXR spectra of the Mo/Si multilayer at λ = 260 Å.

If the spectral purity of the incident wavelength is better than 0.1%, then all the Bragg peaks appearing in the measured curve should not be present, as evident from the simulated curve shown in Figure 2.3.

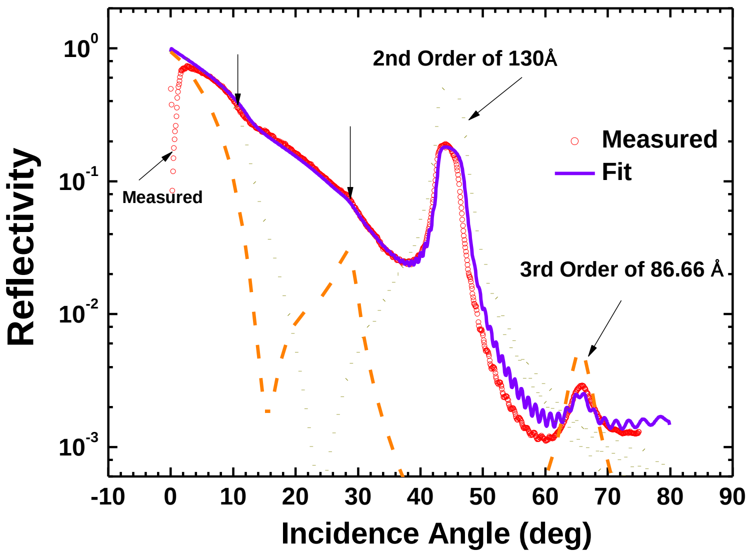

Figure 2.4: Measured reflectivity curve at λ = 260Å is fitted by taking into account the fractional contribution of higher harmonics $\lambda/2$ = 130 Å (dotted curve) and $\lambda/3$ = 86.66 Å (dashed curve).

The presence of two Bragg peaks in the measured data near 44°and 66° incidence angle clearly suggest that the wavelength λ = 260 Å emerging from the TGM contains a significant amount of higher harmonics. With the simulation it is found that the peak at 44° corresponds to the second-order Bragg reflection of λ = 130 Å and the peak at 66° degree corresponds to the third-order Bragg reflection of λ = 86.66 Å from the multilayer. Therefore, to analyze the fractional composition of the harmonic wavelengths the SXR curves at the three wavelengths (260 Å, 130 Å, 86.66 Å) have been theoretically calculated. Fractional composition of these theoretical curves has been varied such that the best fit for the measured reflectivity curve is obtained. This is shown in Figure 2.4, where the best fit for the measured data is obtained with fractional composition of 42% of 260 Å, 35% of 130 Å, and 23% of 86.66 Å wavelengths. It is to be noted that the data away from the Bragg peak region also contain the information of harmonic wavelengths as indicated by the arrows in Figure 2.4. Therefore, the analysis of measured SXR data of the Bragg peak region only will not be sufficient to calculate the correct value of harmonic content.

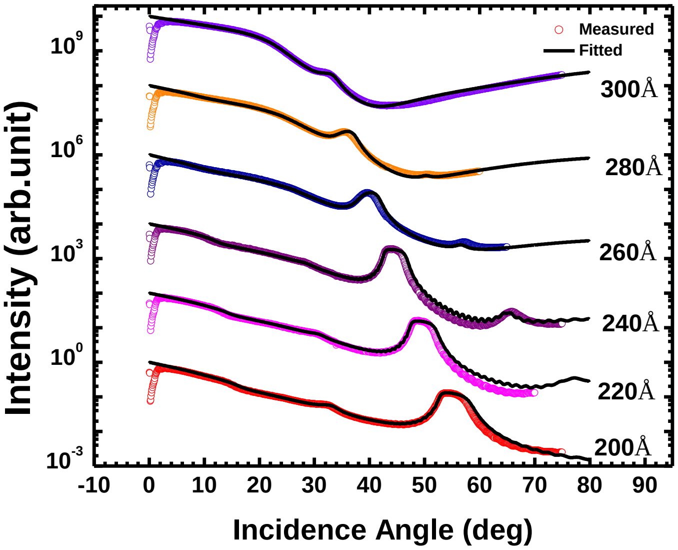

Figure 2.5: Measured and fitted SXR curves at different wavelengths indicated in the graph. For the sake of clarity the curves are vertically shifted.

The same multilayer is used to measure angle versus-reflectivity curves at other wavelengths in the 200 to 300 Å wavelength region. The reflectivity pattern at each wavelength is analyzed, and the fractional composition of the higher harmonics present is calculated. The resultant fit of all the SXR data obtained at each wavelength is shown in Figure 2.5.

Further Figure 2.6 shows the fractional composition of the first, second, and third harmonics present in the incident wavelength coming from the TGM of the beamline. In the 240 to 300 Å wavelength region the second-harmonic contribution is around 30 to40%, and it is >20% for the third harmonic. It is evident that the total harmonic contribution is 50% in the incident beam. The trend of harmonic contribution below 220 Å wavelength is decreasing.

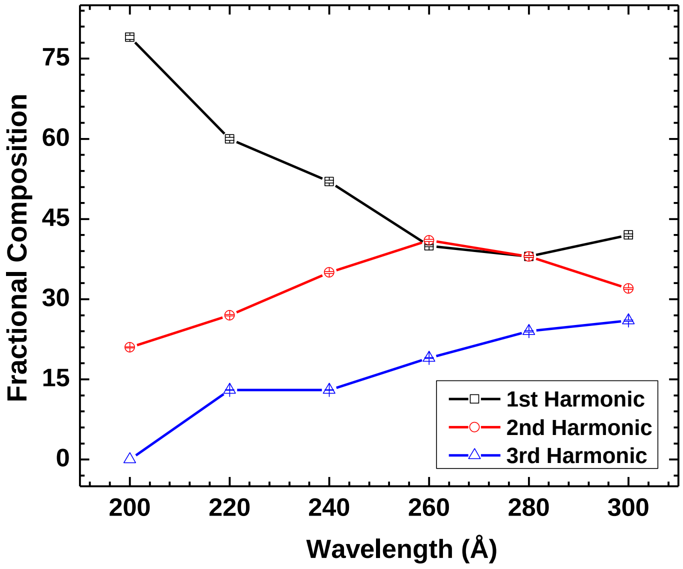

Figure 2.6: The fractional composition of higher harmonics calculated from the SXR analysis in different wavelengths coming from the TGM of the reflectivity beamline.

2.5. Mirror Refurbishment Process:

The coating on optical elements (Mirrors and Gratings) in SR beamlines got damaged due to contamination. This damaged coating on the optical surface degrades the beamline performance. To reuse these mirrors, the coating material needs to be removed by using suitable cleaning method. In the present work, we have used laser cleaning method to remove the gold layer from SiO_2 substrate. After several parameter optimizations, we have successfully removed a 480 Å thick gold layer from SiO_2 substrate successfully. A detailed explanation and analysis of gold removal using nanosecond Nd:YAG laser is given in Ref [60]. Figure 2.7 shows the measured and fitted SXR curves for SiO_2 substrate before and after gold cleaning. The circle in the SXR curve represents the experimental values of reflected intensity and the continuous line represents the fitted values. Measurements are carried out for incidence angle in the range of 0°–70°. Fitting of the SXR curve revealed that, before laser cleaning, the gold layer thickness was 480Å with surface roughness of 26 Å. The SXR curve shows interference fringes before cleaning caused by the waves reflected from the air–gold film interface and the gold film–substrate interface. This curve shows that critical angle θ_c is 21.03°for thin gold film. After the gold layer cleaning, the critical angle θc is shifted from the value of 21.03°toward a lower angle value of 11.13° in the curve, which corresponds to the critical angle for SiO_2 substrate. It clearly indicates that the gold layer is effectively removed from the SiO_2 substrate. The SiO_2 substrate rms roughness is found to be 8 Å before laser cleaning. This roughness improved to a value of 5 Å after the laser cleaning process. It is also observed that, after laser cleaning, the exposure of these mirrors to the atmosphere results in the formation of an additional surface layer of 30–50 Å thickness due to atmospheric effects.

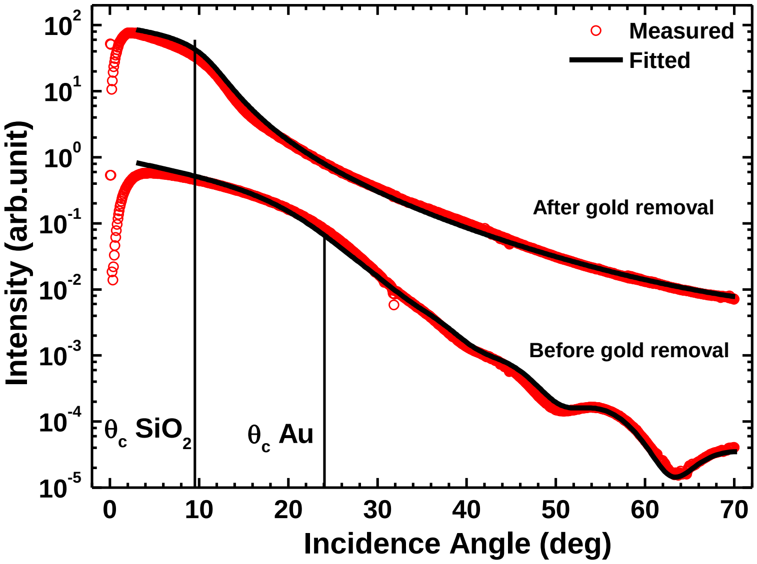

Figure 2.7: Soft x-ray reflectivity spectra of the sample before and after gold layer cleaning using 130 Å wavelength. Open circles represent the experimental data whereas continuous lines are corresponding to the best fit. Curves are vertically shifted in the y axis for clarity. The vertical lines mark positions of the critical angle for Au film and fused silica substrate [60].

Further x-ray photoelectron spectroscopy (XPS) measurements before and after laser cleaning are carried out and the results are shown in Figure 2.7. The XPS curve of the gold film is fitted using two components, one with peak energy near 83 eV and the second having peak energy near of 87.5 eV corresponding to gold film as shown in Figure 2.7. After the laser cleaning, it is found that the peaks corresponding to the gold layer disappear completely. It is clear from the XPS analysis that, after the laser cleaning, the gold layer is removed completely.

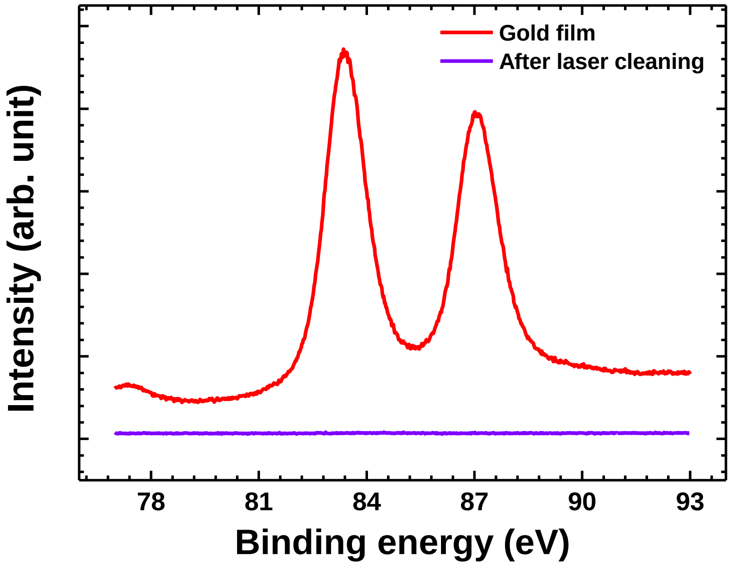

Figure 2.8: XPS spectrum of the gold layer (4f core) shows that the peaks of gold disappear after the laser cleaning process [60].

2.6. Sample:

The deposition processes to deposit thin films can be classified generally as physical or chemical deposition methods. Physical vapor deposition (PVD) includes deposition by evaporation, laser ablation, vacuum-arc, sputtering (direct current, e-beam, and magnetron), etc., whereas chemical vapor deposition (CVD) involves chemical reaction from the vapor phase. The purpose of any PVD or CVD process is to deposit thin films with desired properties in a controlled and reproducible manner. These properties may be chemical, mechanical, electrical, or optical in nature such as composition, purity, morphology, thickness, microstructure, electrical and thermal conductivity, optical absorption or transmission, adhesion, wear, reactivity etc.

In the present thesis work, we have used ion-beam sputtering technique for the deposition of thin films, which is briefly discussed. When energetic gas ions (e.g. inert gas like argon) impinge on the target material, the atoms/molecules are ejected from the target through momentum transfer. This process is known as sputtering.

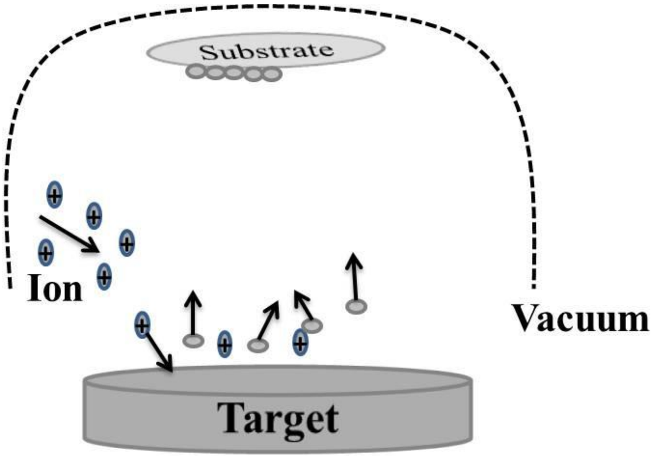

Figure 2.9: Schematic diagram of the sputtering process. Argon ions impinge on the target surface and sputter away target atoms that can form a film at the substrate.

The material that is sputtered away from the target traverses the vacuum chamber and condenses on the surfaces, including the substrate. A thin film is thus formed on the substrate. The general principle of sputtering is explained in Figure 2.9. The film growth rate is determined by two factors: (i) the sputtering rate, i.e. the rate at which material is sputtered away from the target, (ii) the sticking coefficient. The sputtering rate is the product of the ion current density and the sputtering yield. The sputtering yield is an important quantity of the sputtering process and is defined as the number of atoms sputtered away from the target per incident ion[61,62]. It depends on several parameters such as the energy, mass and atomic number of the bombarding ion and the target composition. An ion source is used to produce a directed ion beam which is incident on the target material for sputtering deposition. The most commonly used ion source is the Kaufman broad ion source and the same is employed in our ion beam sputtering deposition system. The schematic diagram of the ion beam sputtering deposition setup is shown in Figure 2.10.

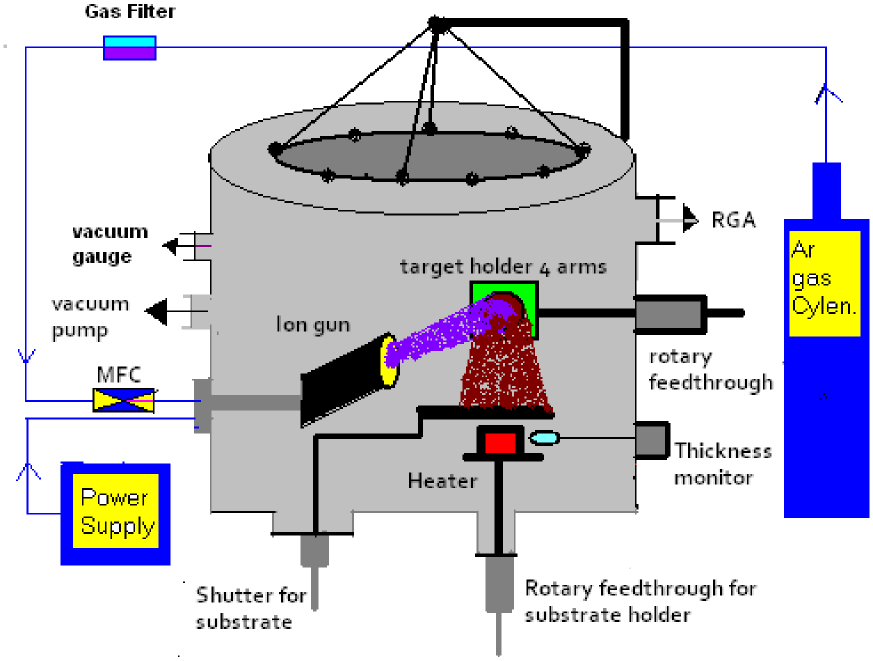

Figure 2.10: Schematic diagram of ion-beam sputtering set-up is shown.

We used a 3 cm diameter Kaufmann-type 1.5 kV hot-cathode gridded ion source, at an angle of 45° with respect to the chamber wall. The argon gas of purity 99.999% is used as sputtering gas in the ion source. The gas flow is measured using mass-flow controller. In our system, a multi-target holder is available, in which four targets of different materials on a rotary motion feed-through can be mounted at the same time. A turbo-molecular pump is used for evacuating the chamber.

In the present thesis work the samples were prepared using ion beam sputtering setup. Prior to start the deposition process, the chamber was first evacuated to a base pressure of 2×10^{-7} mbar. After flushing the chamber two three times with argon gas to remove the contamination of the adsorbed gases, the argon gas flow was fixed at 3 sccm (standard cubic centimeters), which results in a vacuum drop to 5 × 10^{-4} mbar in the chamber. An argon ion-beam of current about 25 mA and voltage 1000 V was used to sputter the target material.

2.7. Structural and Optical Characterization:

2.7.1. X-ray reflectivity:

To determine the structural parameters (thickness, roughness and density) of NbC and ZrC thin films, we have used x-ray reflectivity (XRR) technique. XRR is a very powerful technique for the investigation of the surface and interface behavior of thin film/multilayer materials. This technique is suitable for the determination of (i) thickness of thin films and multilayers, (ii) electron density profile, and (iii) surface and interface roughness of thin films.

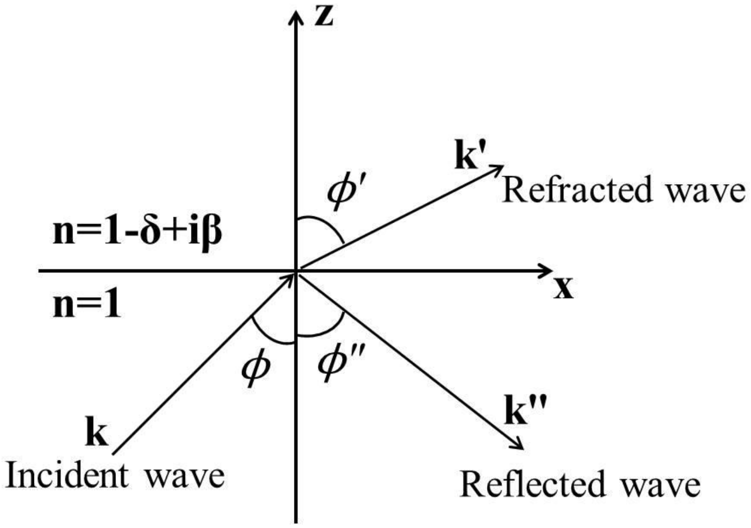

Figure 2.11: Schematic illustration of reflection and refraction of an electromagnetic wave on surface of a two-media system.

When a monochromatic x-ray beam of wavelength λ is incident at the interface of two media of different refractive indices, a part of it is specularly reflected and a part is refracted at an angle ϕ'(see Figure 2.11). Both reflection and refraction depend on the refractive indices of the media and the angle of incidence. The reflected intensity can be simply defined by the intensity ratio of the reflected beam and the incident beam and it can be derived from the Fresnel formulas. The Fresnel's reflectivity formula for s and p polarized light are defined as:

$$r_s = \frac{\cos\phi - \sqrt{n^2 - \sin^2\phi}}{\cos\phi + \sqrt{n^2 - \sin^2\phi}} \quad \mathbf{2.2}$$

$$r_p = \frac{n^2\cos\phi - \sqrt{n^2 - \sin^2\phi}}{n^2\cos\phi + \sqrt{n^2 - \sin^2\phi}} \quad \mathbf{2.3}$$

The reflectivity R is the modulus square of the reflection coefficient ($R=|r|^2$) and is defined as:

$$R_s = |r_s|^2 = \frac{\left|\cos\phi - \sqrt{n^2 - \sin^2\phi}\right|^2}{\left|\cos\phi + \sqrt{n^2 - \sin^2\phi}\right|^2} \quad \mathbf{2.4}$$

$$R_p = |r_p|^2 = \frac{\left|n^2\cos\phi - \sqrt{n^2 - \sin^2\phi}\right|^2}{\left|n^2\cos\phi + \sqrt{n^2 - \sin^2\phi}\right|^2} \quad \mathbf{2.5}$$

Using Eq. 2.4 and 2.5, the reflectivity data are analyzed and structural and optical parameters are determined simultaneously from the measured reflectivity data of a given sample.

The XRR method involves monitoring the intensity of the x-ray beam reflected by a sample at grazing angles. A monochromatic x-ray beam of wavelength λ irradiates a sample at a grazing angle θ and the reflected intensity at an angle 2θ is recorded by a detector. This mode of operation is known as θ-2θ mode. For incident angles θ below a critical angle θ_c, total external reflection occurs. The density of the material is determined from the critical angle with the assumption that the absorption is very less. Above θ_c the reflected waves from different interfaces interferes and gives rise to interference fringes which are also known as Kiessig fringes. The period of the interference fringes and the fall in the intensity are related to the thickness and the roughness of the layer. The effect of surface roughness is taken into account using Névot Croce model. Névot and Croce considered roughness by assuming layers with non-homogeneous thickness. They assumed that the root mean square (rms) deviation of interface with respect to smooth surface is σ_j. With this assumption, they corrected the Fresnel coefficients of reflection as:

$$R = R_F \exp(-2k_j k_{j+1}\sigma_j^2) \tag{2.6}$$

In the present case we have performed both hard and soft x-ray reflectivity techniques. Hard x-ray reflectivity (XRR) measurements are carried out using Bruker D-8 system consisting of a θ-2θ goniometer and a x-ray source of Cu target at $\lambda=1.54$ Å Cu-Kα. Standard alignment procedures are done to align both theta and two theta axes within 0.002°. All the measurements are carried out in the angle range of θ = 0° to 3 to 4° depending upon the sample with a step size of 0.005° in theta axes. Parratt formalism has been used to analyze reflectivity data. Effect of surface roughness has been taken into account using Névot-Croce model, explained above (in Eq-2.6). Soft x-ray reflectivity (SXR) measurements are carried out in 0-70° angle range in 60-200 Å wavelength region using Reflectivity beamline, which has been described above.

2.7.2. X-ray Photoelectron Spectroscopy:

To determine the chemical composition of NbC and ZrC thin films, we have carried out x-ray photoelectron spectroscopy (XPS) measurements. XPS is an analytical tool to investigate the electronic state, chemical state, empirical formula and elemental composition of the elements which are present in the sample.[63] The concept of photons was used to describe the ejection of electrons from a surface when photons were impinged upon it. In other words, when a sample is irradiated with mono energetic photon of energy hν, it emits electrons from the sample surface. The kinetic energies of the emitted electrons are given as:

$$K.E. = h\nu - E_B - \varphi \qquad \mathbf{2.7}$$

where, hν is the energy of the incident photon, E_B is the binding energy of the electrons in the atomic orbital from which it is ejected and φ is the work function of the instrument. Photoelectrons are detected only when $h\nu \geq B.E. + \varphi$. These photoelectrons are sorted with respect to their K.E and a spectrum is generated (known as energy dispersion curves) that represents the emitted electrons per energy interval versus their K.E. From the obtained K.E. the B.E. of the electronic states relative to Fermi level of the emitted electrons are determined. Hence, photoelectron's energy distribution is analogous to the electronic state's energy distribution in a solid. Schematic diagram of photoemission spectroscopy process is shown in Figure 2.12.

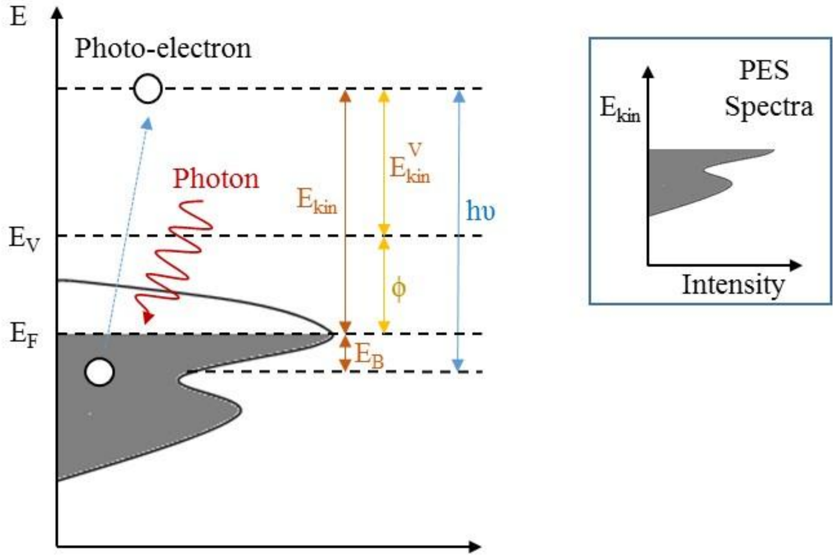

Figure 2.12: Schematic diagram of x-ray photoemission spectroscopy [63].

The basic process of photoemission involves the excitation of electrons from the sample by absorption of a photon of energy *hv*, the transport of the photo excited electrons to the surface of sample and their ejection from the surface into the vacuum. The probabilities of interaction of electrons with matter far exceeds those of the photons, so while the path length of the photons is of the order of micrometres and that of the electrons is of the order of few tens of Angstroms. Therefore, only those electrons that originate within tens of angstroms below the solid surface can leave the surface without energy loss. Since ionization occurs to a depth of a few micrometres which make the photoemission a surface sensitive technique in spite of large penetration depth of X-rays. These electrons having a mean free path up to a few Angstroms only produce the peaks in the spectra and are most useful while the other electrons, which undergo loss processes before emerging out from the surface; form the background. The loss processes include scattering of photo excited electrons with other electrons, plasmons and phonons. The electron-electron scattering dominates the background at the lower K.E values.

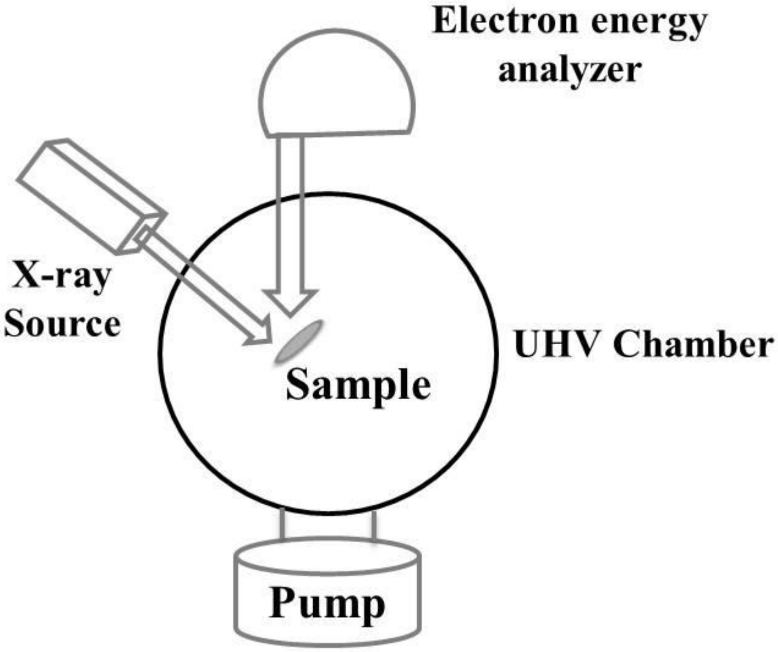

Figure 2.13: Block diagram of X-ray photoelectron spectrometer.

The photoelectron spectroscopy chamber (See Figure 2.13) consist of three major components 1)- A photon source, 2)- An electron energy analyser and 3)- An electron detector. In the chamber, ultrahigh vacuum is maintained in order to increase the mean free path of photoelectrons emerging from the sample surface and reaching the detector. Also, the ultrahigh vacuum is prerequisite to minimize the chances of formation of contamination layer on the sample surface during the measurements. The monochromatic photon source is essential as the photoelectron's energy depends on it. The electrostatic analyser helps to analyse the energy of photoelectrons. The electrostatic lens, the hemispherical elements and the detector (basically an electron multiplier tube) complete the assembly of the analyser. Omicron energy analyser with monochromatic X-ray radiation source Al K_α (E = 1486.6 eV) is used for collection of core level photoemission data in the present work. The chemical shift arising in the core level of ionizing atom depending on the chemical environment helps to predict the chemical structure of the sample.

In the present thesis work XPS measurements of NbC and ZrC thin films are carried out using Al source operated at 10 kV anode voltage and 10 mA emission current. Samples are etched by Argon ion beam (4 kV, 1 μA) to clean the sample surface and for chemical depth profiling. Survey scans are collected over 0 – 1400 eV kinetic energies. Detailed core scans are then performed to find the oxidation state of the constituent elements. XPS data have been recorded for as deposited and after different (10, 20, 30 and 40 minutes) sputtering time cycle. XPS spectra have been de-convoluted using Gaussian de-convolution method.

2.7.3. X-ray Diffraction:

To investigate the crystalline state of NbC and ZrC thin films, grazing incidence x-ray diffraction (GIXRD) measurements are carried out. X-ray diffraction (XRD) is a non-destructive technique for the qualitative and quantitative analysis of the crystalline as well as amorphous materials. Basically, XRD is the "reflection" of an x-ray beam from a family of parallel and equally spaced atomic planes, on the basis of Bragg's law[64]. Diffraction occurs when the x-ray waves interact with a regular structure, whose repeat distance is of the order of the x-ray wavelength. X-rays wavelengths are of the order of few angstroms, the same as the typical inter-atomic distances in crystalline solids, which suggest that x-rays can be diffracted from crystalline materials of regularly repeating atomic structures.

Figure 2.14 shows the schematic representation of Bragg's law. When a monochromatic x-ray beam is incident on lattice planes at an angle θ, the diffraction occurs if the path of rays reflected by successive planes (with inter-atomic spacing, d) is a multiple of the wavelength. Then, it is possible to analyze the inter-atomic spacing of a crystal (or a powder) by measuring the first-order angles of diffraction, using the formula,

$$2d\sin\theta = m\lambda \tag{2.8}$$

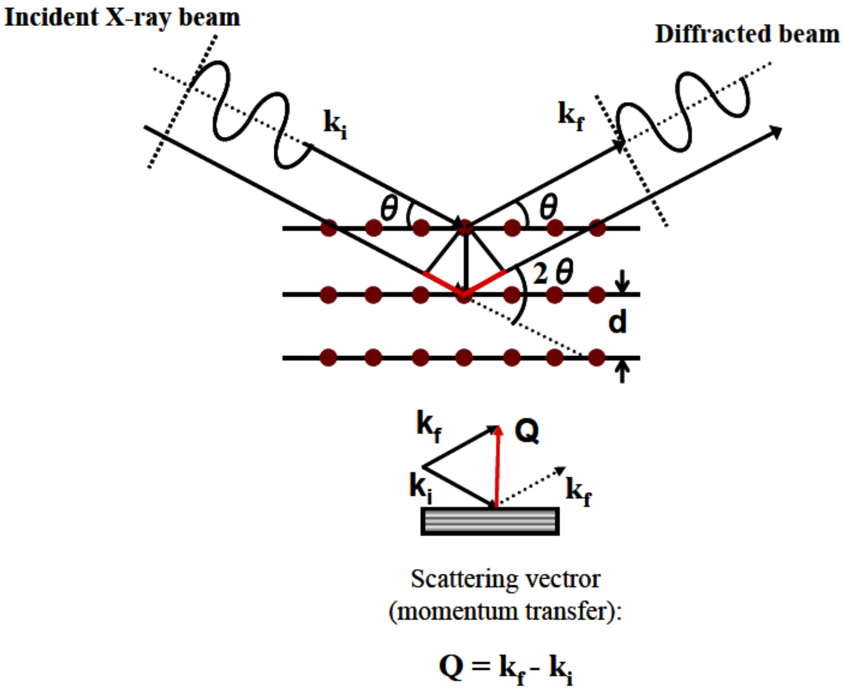

Figure 2.14: Geometric construction of Bragg's law [64].

where, m is an integer, λ is the wavelength of x-rays in angstroms, and θ is the diffraction angle in degrees. X-ray radiation has generally large penetration depth into any matter. In the case of thin films, the diffracted intensities for film materials are very low compared to the substrate and background. To overcome this restriction, Grazing Incidence X-ray Diffraction (GIXRD) is used. In this geometry, the stationary incident beam is fixed at very small angle with the sample surface (typically 0.5°to 1°), which increases the path length of the X-ray beam inside the thin film grown on the substrate. This results in increased diffracted intensity corresponding to thin film and reduces the diffracted intensity from the substrate simultaneously. Because of this, a dramatic increase in the film signal-to-background ratio is achieved. In the present case the GIXRD measurements are carried out at ADXRD beamline[65] at Indus-2 synchrotron radiation source. The beamline consists of a Si (111) based double crystal monochromator and two experimental stations namely a six circle diffractometer with a scintillation point detector and Mar- 345 dtb Image plate area detector[66]. In the present study, GIXRD measurements have been carried out at wavelength λ=1.24 Å using the image plate detector. Incident monochromatic beam is fixed at an angle of 0.5° and GIXRD patterns are recorded. The wavelength and the distance between the sample and the detector is calibrated using XRD pattern of NIST standard LaB_6 powder.

2.7.4. Atomic Force Microscopy:

For the investigation of surface morphology of NbC and ZrC thin films in large spatial frequency region, atomic force microscopy (AFM) measurements have been carried out. AFM is the one of the most powerful technique for determination of surface morphology of the films at nanoscale. AFM probes the sample surface of with a sharp tip, typically of length in microns and often less than 100 Å in diameter. The tip is located at the free end of a cantilever that is 100 to 200 μm in length. The movement of the tip on sample is performed by an extremely precise positioning device made from piezoelectric ceramics, most often in the form of a tube scanner. The scanner is capable of sub-angstrom resolution in x, y and z -directions. The z -axis is conventionally perpendicular to the sample. Tips are made from Si_3N_4 or Si, and extended down from the end of a cantilever. The inter-atomic forces between the probe tip and the sample surface cause the cantilever to deflect as the sample's surface morphology changes.

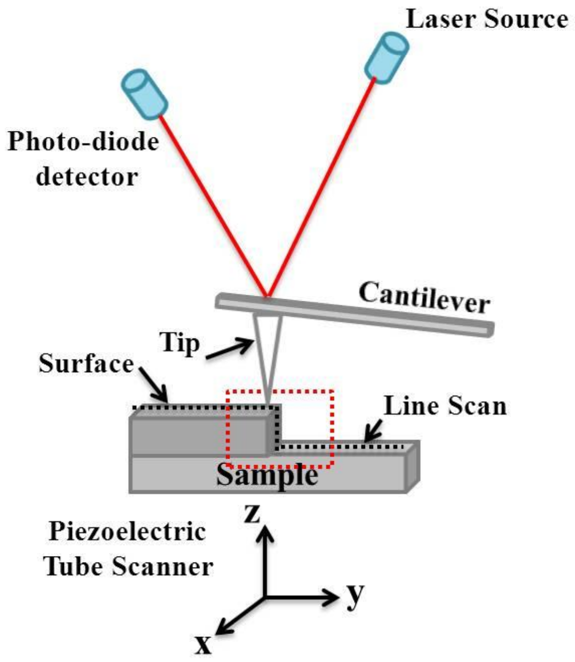

Figure 2.15: Schematic diagram for atomic force microscope.

Since the cantilever works on Hooke's law for small displacements, the interaction force between the tip and the sample can be determined. The force between the tip and the sample surface is very small, usually less than 10^{-9} N. The detection system does not measure force directly. It senses the deflection of the cantilever. The AFM head employs an optical detection system in which the tip is attached to the underside of a reflective cantilever. A diode laser beam is focused on the split photo-diode from the back of a reflective cantilever. As the tip scans the surface of the sample, moving up and down with the contour of the surface, the laser beam is deflected off the attached cantilever into a dual element photodiode. The photo detector measures the difference in light intensities between the upper and lower photo-detectors, and then converts it to voltage. Feedback from the photodiode difference signal, through software control from the computer, enables the tip to maintain either a constant force or constant height above the sample. In the constant force mode the piezo-electric transducer monitors the real time height deviation. A schematic diagram of AFM setup is shown in Figure 2.15.

In the AFM technique, the image contrast can be obtained in three different modes, depending on the application. These modes are contact mode, non-contact mode and tapping mode and are explained below.

Contact Mode:

In the contact mode, also known as repulsive mode, the AFM tip makes soft physical contact with the sample. The tip is attached to the end of a cantilever with a spring constant, lower than the effective spring constant holding the atoms of the sample together. As the scanner gently traces the tip across the sample (or the sample under the tip), the contact force causes the cantilever to bend to accommodate changes in morphology. One of the drawbacks of the contact mode is that there exists large number of lateral forces on the samples as the tip is “dragged” over the specimen. Therefore, this mode is applied on hard crystalline surface but it is not suitable for biological samples where this force is still strong enough to cause their deformations.

Non-Contact Mode:

In the non-contact or attractive mode, the tip is at a distance (of the order of tens to hundreds of Å) from the sample surface where the attractive van der Waals forces dominate. The cantilever must oscillate above the surface of the sample.

Tapping Mode:

In the tapping mode, the cantilever oscillates at its resonant frequency (often hundreds of kilohertz) and is positioned above the surface so that it can tap the surface for a very small fraction of its oscillation period. This is still in contact with the sample, but for the very short time over which this contact occurs, it means that lateral force is dramatically reduced as the tip scans over the surface.

In this work, Digital Instruments MultiMode SPM with Nanoscope Iva controller AFM is used for AFM measurement in the contact mode. AFM measurements are carried out over 1×1, 2×2, 5×5 and 10×10 μm^2 range over 256×256 pixel area. AFM data measured over different length scales have been combined to generate a single power spectral density (PSD) over a large spatial frequency range. PSD can be calculated using[67]

$$PSD(f) = \Omega \frac{1-\exp[-2\nu\,|2\pi \mathrm{f}|^{n}\,\tau]}{\nu\,|2\pi \mathrm{f}|^{n}} \qquad \mathbf{2.9}$$

where Ω is the volume of a constitute element of the film, ν is the independent growth parameter which characterizes the relaxation, n varies according to kinetic mechanism that dominates the smoothening process. PSD curves generated from AFM images of different scales are combined to generate a single PSD in large frequency range. Further the rms roughness is calculated by integrating the PSD in whole frequency rage using following equation:

$$\sigma^2 = 2\pi \int_{f\,\min}^{f\,\max} PSD(f)\, f df \qquad \mathbf{2.10}$$

The rms roughness has been determined by integrating the PSD in 10^{-2} to 10^{-4} nm^{-1}range for NbC and ZrC thin films.

2.7.5. X-ray Absorption Fine Structure:

To reveal the oxidation state of Nb and local structure of NbC thin films of different thicknesses, Nb K-edge x-ray absorption fine structure (XAFS) measurements are carried out. X-ray absorption spectroscopy (XAS) is a powerful tool to study local electronic and atomic structure of solids, liquids and gases. XAS spectra typically display x-ray absorption fine structure (XAFS) above the x-ray absorption edge which can be exploited for a variety of analytical purposes. In the near edge region, XAFS measurements can be used for qualitative chemical analysis (oxidation states, coordination symmetry). Far above the absorption edge, XAFS measurements can yield information about the local coordination environment of the absorbing atoms (bond lengths, coordination numbers and structural disorder). When a beam of monochromatic x-ray goes through matter, it loses its intensity due to interaction with the atoms in the material. The intensity drops exponentially with distance if the material is homogeneous and the intensity after transmission is given by $I = I_0e^{-\rho\mu t}$, where I and I_0 are the transmitted and the incident x-ray intensities respectively, ρ is the mass density, μ is the absorption coefficient and t is the thickness of the sample. The absorption coefficient decreases with increase in energy, except for certain photon energies. Whenever the photon energy reaches the critical value for a core electron transition the absorption coefficient increases abruptly. These abrupt increase in absorption occur whenever the incident photon has just enough energy to promote a core electron to an unoccupied valence level or into the continuum (leave the atom). The probability to eject an electron is largest when the photon energy is sufficient for the transition process. After each absorption edge, the absorption coefficient decreases with increase in the photon energy. XAFS is a final state interference effect involving scattering of the outgoing photoelectron from the neighboring atoms.

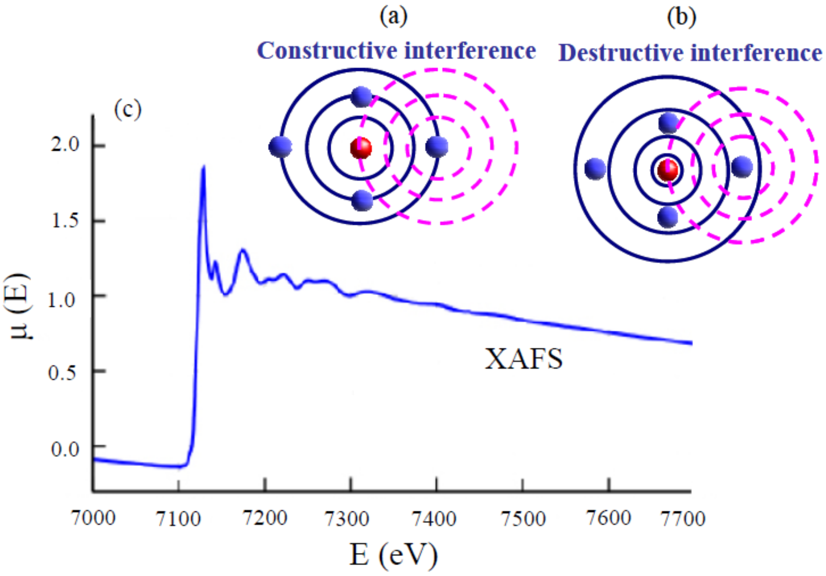

Figure 2.16: The photoelectron wave is shown with solid line circle, which can be backscattered from the neighboring atoms shown with dotted line circle and interfere with the photoelectron wave at the absorbing atom. Depending on the wavelength of the photoelectron, the scattered wave can interfere (a) constructively or (b) destructively. (c) The resultant XAFS spectrum is shown as function of energy [71].

The probability of an x-ray photon absorbed by a core electron depends on both the initial and the final states of the electron. The initial state is the localized core level corresponding to the absorption edge. The final state is that of the ejected photoelectron which can be represented as an outgoing spherical wave originating from the x-ray absorbing atom. If the absorbing atom has a neighboring atom, the outgoing photoelectron wave will be backscattered by neighboring atom, thereby producing an incoming electron wave. The final state is then the sum of the outgoing and all the incoming waves, one from each neighboring atom. It is the interference between the outgoing and the incoming waves that gives rise to the sinusoidal variation of $\mu\ (E)$ vs E. A photoelectron ejected by absorption of an x-ray photon will travel as a spherical wave with a wavelength $\lambda=2\pi/k$, where k is the photon wave vector and is defined as:

$$k = \sqrt{\frac{2m}{h^2}(\mathrm{E}-\mathrm{E}_0)} \qquad \textbf{2.11}$$

where m is the mass of the electron, h is Plank's constant, E is the incident photon energy and E_0 is the threshold energy of the corresponding absorption edge. The amplitude and frequency of this sinusoidal modulation of $\mu(E)$ vs E depends on the type (and bonding) of the neighboring atoms and their distances away from the absorber, respectively.

For the XAFS, we are interested in the oscillation well above the absorption edge, and define the XAFS fine-structure function χ (E) defined as:

$$\chi(E) = \frac{\mu(E) - \mu_0(\mathrm{E})}{\Delta\mu_0(\mathrm{E})} \qquad \mathbf{2.12}$$

where $\mu(E)$ is the experimental absorption coefficient (in an x-ray fluorescence experiment, the absorption coefficient μ is calculated by $\mu\ (E) \propto I_f / I_0$), and $\mu_0\ (E)$ is the atomic contribution to the absorption coefficient which is proportional to the number to atoms per unit volume, $\Delta\mu_0$ is the measured jump in the absorption, $\mu(E)$ at the threshold energy E_0. The difference [$\mu\ (E) - \mu_0\ (E)$] represents the XAFS oscillations with the background subtracted via division $\Delta\mu_0$, the XAFS oscillation $\chi\ (E)$ is normalized to a per atom basis. In order to obtain structure information, $\chi\ (E)$ is converted to $\chi\ (k)$.

The different frequencies apparent in the oscillation in $k\ \chi(k)$ correspond to the different near-neighbor coordination shells which can be described and modeled according to the XAFS Equation[68]

$$k\chi(k) = S_0^2 \sum_j \frac{N_j}{R_j^2} F_j(k) \exp(-2k^2\sigma_j^2) \exp\left(-\frac{2R_j}{\lambda(\mathrm{k})}\right) \sin\left\{2kR_j + \phi_j(\mathrm{k})\right\} \qquad \mathbf{2.13}$$

where N_j is the multiplicity of the j^{th} contribution, and $2R_j$ and σ_j are the average length and variation (Debye-Waller factor) of the photoelectron path respectively. Further $F_j\ (k)$ and $\phi_j(k)$ are the amplitude and phase shift function, λ(k) is the photoelectron mean free path and S_0^2 is an empirical parameter taking into account many-body effect.

The experimental XAS spectra, $\mu(E)$, are treated following the standard methods to extract the XAFS structural signal $\chi(k)$: the pre-edge background is fitted with a straight line and then subtracted; the post-edge atomic background is modeled with a smooth polynomial spline through the experimental data. The energy scale for the photoelectron wave vector is defined to choose the edge energy (E_0) at the maximum of the $\mu(E)$ first derivative data. The statistical noise of XAS data (η) is evaluated as follows: the post-edge experimental data are fitted with high order polynomials simulating the structural signal, and then the statistical noise is estimated as the variance of the difference, normalized to the jump height between polynomial function and the experimental data.

In the present thesis work XANES and EXAFS spectra were recorded at BL-9, Scanning EXAFS Beamline[69,70] of Indus-2 synchrotron radiation source. EXAFS measurements for NbC films are carried out in fluorescence mode. The beamline consists of Rh/Pt coated meridional cylindrical mirror for collimation and Si (111) based double crystal monochromator to select excitation energy. XANES and EXAFS measurements were carried out in fluorescence mode using Vortex energy dispersive detector (VORTEX-EX). The energy range of EXAFS is calibrated using standard Nb foil. Two standards NbO_2 and Nb_2O_5 are measured in transmission mode to estimate the oxidation state of Nb in NbC films. EXAFS data are processed using ATHENA software[71], whereas detailed fitting of EXAFS data are carried out in the k range of 2.5-7.5 $Å^{-1}$ using standard EXAFS equation (Eq-2.13) using Artemis program where amplitudes and phases corresponding to all possible scattering from near neighbor atoms are calculated using FEFF 6.0 code[72].

2.7.6. Raman Spectroscopy:

Raman spectra are extremely sensitive to all form of carbon (graphite or diamond), we have carried out Raman measurements of gold film before and after laser cleaning. Raman spectroscopy is a technique used in condensed matter physics and chemistry to study vibrational, rotational, and other low-frequency modes in a system. It relies on inelastic scattering, or Raman scattering of monochromatic light, usually from a laser in the visible, near infrared, or near ultraviolet range. The laser light interacts with phonons or other excitations in the system, resulting in the energy of the laser photons being shifted to lower or higher value. The Raman Effect corresponds, in perturbation theory, to the absorption and subsequent emission of a photon via an intermediate electron state, having a virtual energy. Energy level diagram of the states involved in Raman signal are shown in Figure 2.17.

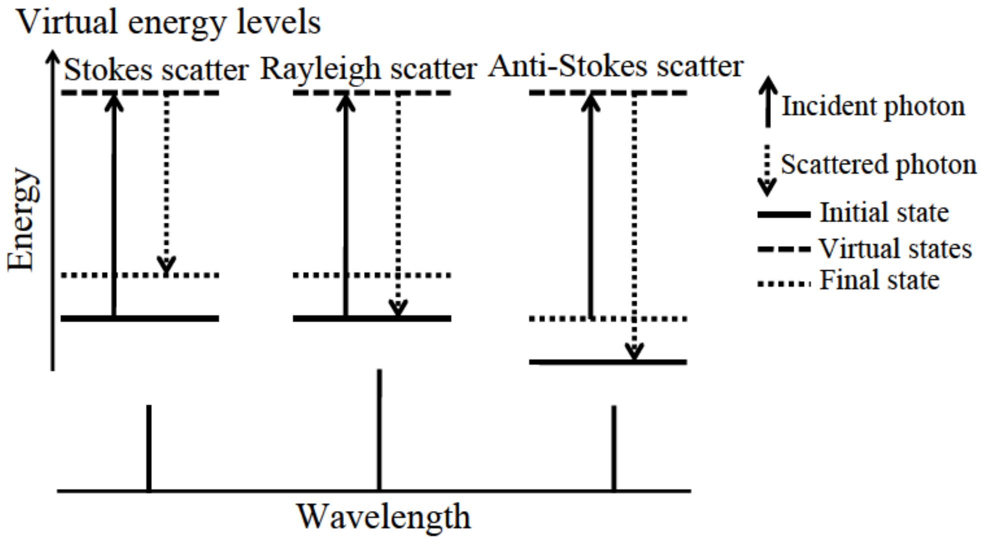

Figure 2.17: Energy level diagram for Raman Scattering.

Based on the energy level diagram, there are three possibilities:

- ✓ There is no energy exchange between the incident photons and the molecules (and hence no Raman effect)

- ✓ There is energy exchange between the incident photons and the molecules. The energy differences are equal to the differences of the vibrational and rotational energy-levels of the molecule. In crystals, only specific photons are allowed (solutions of the wave equations which do not cancel themselves) by the periodic structure, so Raman scattering can only appear at certain frequencies. In amorphous materials like glasses, more photons are allowed and thereby the discrete spectral lines become broad.
    - Molecule absorbs energy (Stokes scattering): The resulting photon of lower energy generates a Stokes line on the red side of the incident spectrum.
    - Molecule loses energy (anti-Stokes scattering): Incident photons are shifted to the blue side of the spectrum, thus generating an anti-Stokes line.

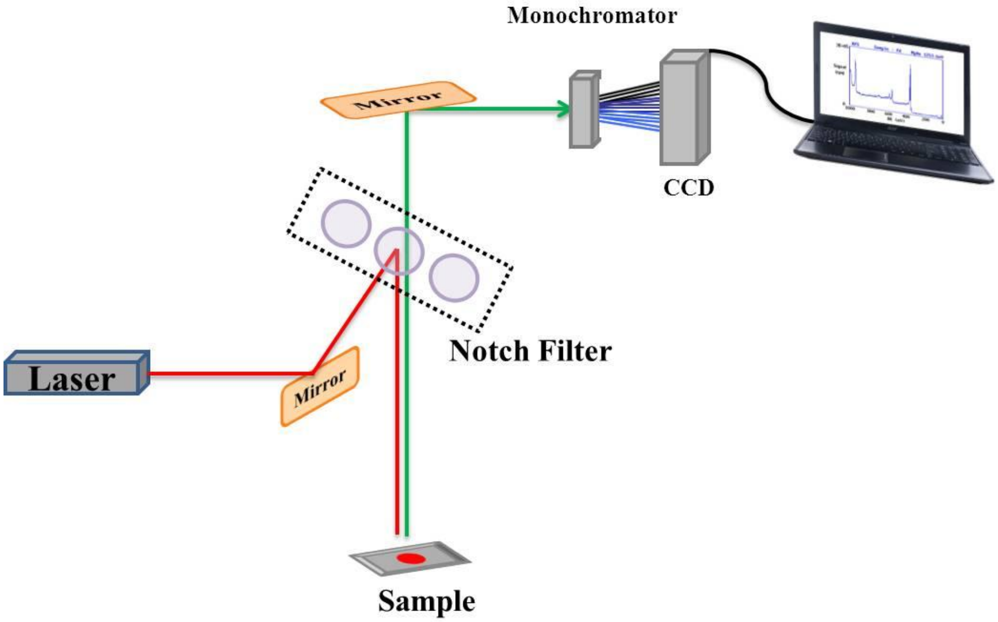

Figure 2.18: Schematic diagram of HR 800 micro Raman setup.

Raman spectroscopy employs the Raman Effect for materials analysis. The frequency of light scattered from a molecule may be changed based on the structural characteristics of the molecular bonds. Raman scattering consists of frequencies of $\upsilon_0 \pm \upsilon_m$ where υ_m is a vibrational frequency of a molecule and υ_0 is the frequency of the incident beam. Thus, the vibrational frequency (υ_m) as a shift from the incident beam (υ_0) is measured[73].

A Raman spectrometer consists of four major components which are excitation source, sample illumination and collection system, wavelength selector, and detector and computer control/processing system. In this thesis, the micro Raman system HR800 from Jobin Yvon Horiba with 488 nm of argon 10 mW, is used as shown in Figure 2.18. In this system, the laser is totally reflected by the notch filter towards the sample under the microscope. The Raman signal are collected by the microscope objective in back scattering configuration follows the same way back. The reflection on the sample of the laser line (Rayleigh scattering) is redirected onto the notch filter rejecting the excitation wavelength of the confocal hole and entrance slit of the spectrograph. Raman shifted light is passed to a dispersive grating under the entrance optic of the instrument and forming a spectrum image on the CCD (charge-coupled device) detector.

In the present thesis work Raman scattering is excited using the Ar laser at 488 nm and is measured using a Jobin-Yvon micro-Raman spectrometer (HR800) over the range 800–1800 cm^{-1}. Raman spectrum is de-convoluted with Lorentzian peaks.

Chapter 3.

Study on Structural and Optical Properties of NbC

Compound materials (such as B_4C, LaN, NbC etc.) are being used in soft x-ray and extreme ultraviolet optical applications and have shown stable and enhanced performances. In this chapter, optical constants of NbC in 60-150 Å wavelength region are determined and effect of structural disorder on soft x-ray optical response is analyzed. A discrepancy in soft x-ray performance of NbC film is observed, which could not be explained with Henke's tabulated data. To understand this detailed structural and chemical characterizations are carried out using several experimental techniques. Results obtained are described in detail.

3.1 Introduction:

Multilayer mirrors comprised of low Z / high Z elements such as Mo/Si, Nb/Si, W/Si, Zr/Al etc. are widely used in variety of applications in the soft x-ray energy region. Mo/Si multilayer exhibits high reflectivity performance near Si L absorption edge and are the most promising reflective coating for extreme ultraviolet (EUV) lithography applications near 130 Å wavelength[74]. However this combination has a severe drawback of high chemical reactivity among the constituent elements due to negative heat of mixing between Mo and Si. Silicide formation is a common problem in Si based multilayers, when they are used at elevated temperatures in high heat load environment. In Mo/Si multilayers the process of silicide formation starts after 300-400°C. W/C multilayer is used in soft x-ray region of < 3 keV and in hard x-rays of > 3 keV[75,76,77,78].[79]. In W/C multilayers amorphous to crystalline transition in W layer with increase in film thickness is reported on thermal annealing. Formation of hexagonal tungsten carbide (WC) on interfaces is found[80]. Recent development of free electron laser sources[30,31] generating ultra-short EUV pulses have posed new challenges for x-ray optical elements. X-ray pulses of very high brightness stimulate radiation induced damage in optical elements[32,33]. The emerging technology requires improved and stable optical elements[34,35]. Further to overcome this difficulty of intermixing and to prevent silicide formation in Si based multilayers, barrier layers (of pure carbon, B_4C etc.) are used in between the constituent elements. In literature a barrier layer of < 3 Å of pure carbon and < 3 Å B_4C at each Mo-Si interface is used to prevent the intermixing[81,82]. However, inserting an extra layer leads to phase variation in the waves reflecting from different interfaces at the Bragg condition and thereby resultant phase mismatch reduces the reflectivity performance. Further this barrier layer should be ultrathin in order to minimize the phase mismatch, which requires a stringent deposition control. In literature several authors have used compound materials (NbC, B_4C, LaN, ZrC etc.) as a replacement to elements in the elemental multilayers. The optical constants of these compound materials are very similar to those of corresponding elements in the soft x-ray energy region. A. F. Jankowski et al. have shown W/B_4C multilayer a better combination (thermally more stable) in comparison with W/C multilayers[83]. W/B_4C multilayers have shown equal or exceed reflectivity performance than W/C multilayer, without any change in the structure on thermal treatment up to 500°C. Recently NbC/Si multilayer has been proposed for EUV applications as a replacement to Mo/Si multilayer[38]. In transition metal carbides, the carbide layers are non-stoichiometric and has significant amount of unreacted carbon[39,40]. The presence of unreacted carbon in the near vicinity of metal species (Nb, Mo, Zr etc.) may act as a barrier layer for Si or other elements to prevent the chemical intermixing. The NbC/Si multilayer was shown thermally stable up to 700°C without significant loss in reflectivity performance[38]. In this combination the NbC shows similar optical performance to that of Mo in the soft x-ray/ EUV region. The new combination of NbC/Si multilayer can be used near the Si L edge region in place of conventional Mo/Si combination.

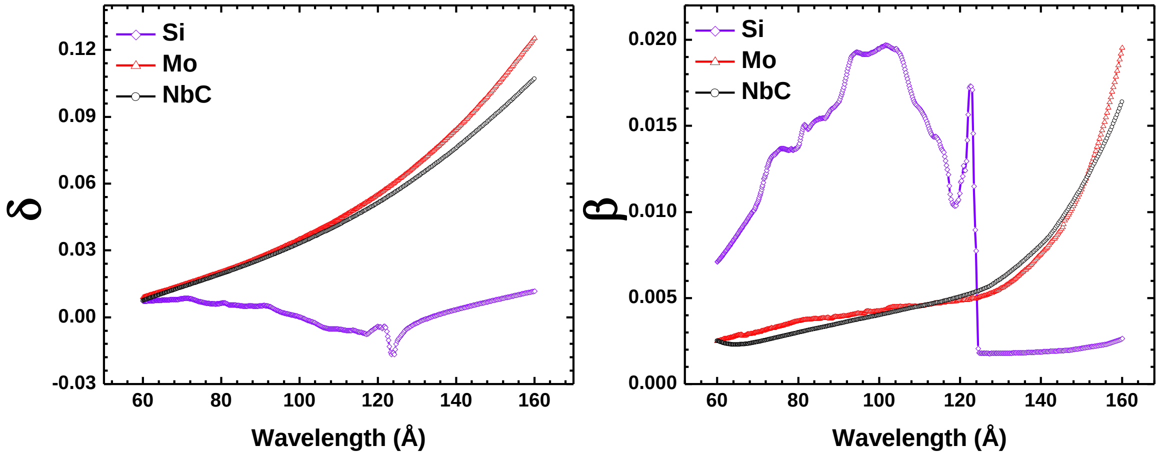

Figure 3.1: Comparison of the optical constants of NbC and Mo with Si is shown in 60-160 Å wavelength region. Delta (δ) and beta (β) contrast for NbC and Si are similar to Mo and Si.

In Figure 3.1, the optical constants of Mo, NbC and Si, calculated from centre for x-ray optics (CXRO) database[84] are plotted in 60 – 160 Å wavelength region. From Figure 3.1, it is clear that the optical constants for Mo and NbC are similar in the whole wavelength region. Also the contrast in optical constants of NbC and Si is similar as the contrast between Mo and Si. Therefore NbC/Si multilayer exhibit identical reflectivity performance as one obtains with Mo/Si multilayer.

Depositions of high quality NbC thin films are difficult due to their unusual properties such as high melting point, low evaporation and sputtering rate, high reactivity of Nb with oxygen and water vapors. In literature, few studies on the study of NbC thin films deposited using several techniques such as physical vapour deposition, chemical vapour deposition, DC magnetron sputtering, e-beam evaporation, pulsed laser deposition (PLD) etc.are available. In PLD technique laser fluence of around 10J/cm^2 is required for the deposition of metal carbide thin films, which is difficult to be implemented[85]. Further deposition of high quality NbC thin films requires optimization of several deposition parameters to obtain high density and low surface roughness. Jeffrey A. Klug et al. have deposited NbC thin film based superconductors[86], using atomic layer deposition (ALD) technique. They obtained reasonable low density films of 3.44 g/cm^3 for the films deposited at substrate temperature of 125°C. Highest density of 4.99 g/cm^3 is achieved for the films deposited at substrate temperature of 350°C, which is still quite below the bulk density (7.82 g/cm^3). In order to use compound materials in actual applications, the structural and optical properties of the thin films of shortlisted compound materials must be investigated thoroughly. Thickness, roughness and density of a thin film are crucial parameter to achieve the theoretical reflectivity performance. The density of the thin film is an important parameter in case of x-ray multilayers. If the density of the film is less than the bulk density, reflectivity drops down significantly. When thin films of compound material are deposited from the bulk target, film density is found less than the bulk density and also structural properties get modified because of change in near neighbour environment and confinement effects. Growth related atomic rearrangement affects the chemical stoichiometry and which in turn affects their optical properties[41]. Hence detailed study on the structural properties of thin films of compound material (NbC) is required before actual device fabrications.

In soft x-ray energy region, the optical properties of any material can be described by energy dependent complex index of refraction $n=1-\delta+i\beta$[53], where delta (δ) and beta (β) are refraction and absorption parts respectively. These parameters are known as optical constants. Knowledge of optical constants is essential to predict the optical response of a medium to incident radiation and also to explain the experimental results. In literature several techniques are used for the determination of the optical constants, such as transmission, photoemission, angle dependent reflection etc. Optical constants from a variety of sources are compiled in ref.[42,43] Henke et al.[42] used photo absorption data for the determination of atomic scattering factor for all the elements having atomic number Z= 1-92 in a finite energy range of 50 to 30,000 eV. They applied Kramer-Kronig relation to determine the real part of refractive index from the absorption data. Further to determine the accurate values of real part of the refractive index, Kramers– Kronig integrals should be performed over zero to infinity frequency range. In the practical situation several interpolation/extrapolation functions are used to generate the absorption data for infinite range, which introduces certain errors in the real part of refractive index calculated by Kramers-Kronig method. Furthermore, all materials are highly absorbing in the soft x-ray energy region, so it is quite challenging to deposit free standing ultrathin films to perform transmission measurements.

In the case of compound materials, optical constants are calculated by taking a weighted sum of the optical constants of constituent atoms using Henke's database. This approach works well for photon energies away from the absorption edges of the constituent elements. In the close vicinity of absorption edge this approach fails as the formation of chemical bonds leads to shift in absorption edge. In general, the overlapping of electron wave functions of the constituents of compound material leads to modify the optical constants. The δ and β are traditionally calculated from angle dependent reflectivity technique by means of Fresnel formulae. Both δ and β are experimentally measured at discrete photon energies, which is an advantage over the transmission measurements where only β is measured experimentally.

In this chapter structural and optical properties of NbC thin films are investigated using several experimental techniques. Optical constants in soft x-ray energy region have been determined. Details obtained from the experimental findings are discussed in detail.

3.2 Experimental:

3.2.1 Sample Preparation:

Thin films of NbC (typically 100Å, 200Å, 300Å and 500Å) have been deposited on a polished Si (100) wafer using ion beam sputtering technique[87]. Prior to deposition a base pressure of 3×10^{-7} m-bar was achieved. Deposition has been carried out under argon ambient at constant pressure of 6×10^{-4} m-bar. A commercially available 4 inch sputtering target of NbC (99.95% purity) have been used for deposition. After process optimization, it has been found that the films deposited at 1 kV beam voltage and a gas flow rate of 3 standard cubic centimeters per minute are better in rms roughness. These optimized parameters have been used for the deposition of all the samples. Further details about the deposition process are discussed in Chapter 2.

3.2.2 Optical Characterization:

For optical characterization of NbC thin films soft x-ray reflectivity (SXR) measurements have been carried out using reflectivity beamline[57] at Indus-1 synchrotron radiation source. Details of the beamline are discussed in chapter-2. For NbC thin film reflectivity vs angle scan have been performed in 0-80° incident angle and in 60- 150 Å wavelength region. Reflectivity vs wavelength scan have been carried out in 60 to 360 Å region at 10° incident angles. Optical constants of the materials available from CXRO database[84] have been used for the simulation of experimental data using Parratt formalism[88]. Surface roughness was taken into account using Névot -Croce model[13]. Details of the data analysis procedure are discussed in chapter-2.

3.2.3 Structural characterization:

To determine the chemical composition of NbC thin films, x-ray photoelectron spectroscopy (XPS) measurements have been carried out using an Omicron EA-125 photo electron spectrometer working at a base pressure of ~6.7×10^{-10} m-bar. Al source operated at 10 kV anode voltage and 10 mA emission current has been used for x-ray emission. A 4 kV, 1 µA Argon ion beam has been used to sputter the sample for chemical depth profiling using the XPS technique. XPS data have been recorded for as deposited and after different (10, 20, 30 and 40 minutes) sputtering time cycle. XPS spectra have been de-convoluted using Gaussian de-convolution method. More details about data analysis procedure are discussed in chapter-2.

Further to investigate structural parameters such as thickness , roughness and density of NbC thin films, hard x-ray reflectivity (XRR) measurements were performed using a BRUKER D-8 system consisting of θ - 2θ goniometer and x-ray source of Cu target having λ =1.54 Å wavelength. All the measurements have been performed with a step size of 0.005˚ in theta axes.

Parratt formalism has been used to analyze reflectivity data. Effect of surface roughness has been taken into account using Novet-Croce model[13]. A nonlinear least square refinement routine based on genetic algorithm has been used to refine fitting parameters[89]. More details about the experimental setup and data analysis procedure are discussed in detail in chapter-2.

For the investigation of surface morphology NbC thin films, atomic force microscopy (AFM) measurements have been carried out using the instrument Nanoscope III from Digital Instrument. AFM measurements have been performed over 1×1, 2×2, 5×5 and 10×10 μm^2 range in close contact mode over 256×256 pixel area. AFM data measured over different length scales have been combined to generate a single power spectral density (PSD) over a large spatial frequency range. The rms roughness has been determined by integrating the PSD in 10^{-2} to 10^{-4} nm^{-1}range. Details about the experimental setup are discussed in Chapter-2.

To investigate the crystalline state of NbC thin films, grazing incidence x-ray diffraction (GIXRD) measurements are carried out. GIXRD measurements have been performed at angle dispersive x-ray diffraction (ADXRD) beamline (BL-12)[65] on Indus-2 synchrotron radiation source[90]. The beamline consists of a Si (111) based double crystal monochromator and two experimental stations namely a six circle diffractometer with a scintillation point detector and Mar- 345 dtb Image plate area detector[66]. In the present study, GIXRD measurements have been carried out using the image plate detector. Incident monochromatic beam was fixed at an angle of 0.5˚ and GIXRD patterns are recorded by image plate detector. The wavelength and the distance between the sample and the detector are calibrated using XRD pattern of NIST standard LaB_6 powder. GIXRD data have been integrated using Fit2D software[91]. Details of ADXRD beamline and Image plate detector are discussed in Chapter-2.

To understand the local structure of NbC in thin films, extended x-ray absorption fine structure (EXAFS) measurements are carried out at BL-9, Scanning EXAFS Beamline[69] of Indus-2. The beamline consists of Rh/Pt coated meridional cylindrical mirror for collimation and Si (111) based double crystal monochromator to select excitation energy. XANES and EXAFS measurements are carried out in fluorescence mode using Vortex energy dispersive detector (VORTEX-EX). The energy range of EXAFS is calibrated using Nb foil at 18986 eV. Two standards NbO_2 and Nb_2O_5 are measured to estimate the oxidation state of Nb in NbC films. EXAFS data are processed using ATHENA software[71], whereas detailed fitting of EXAFS data are carried out in the *k* range of 2.5-7.5 $Å^{-1}$ using standard EXAFS equation using Artemis program where amplitudes and phases corresponding to all possible scattering from near neighbor atoms are calculated using FEFF 6.0 code[72]. More details about the EXAFS beamline and XAFS data analysis procedure are discussed in chapter-2.

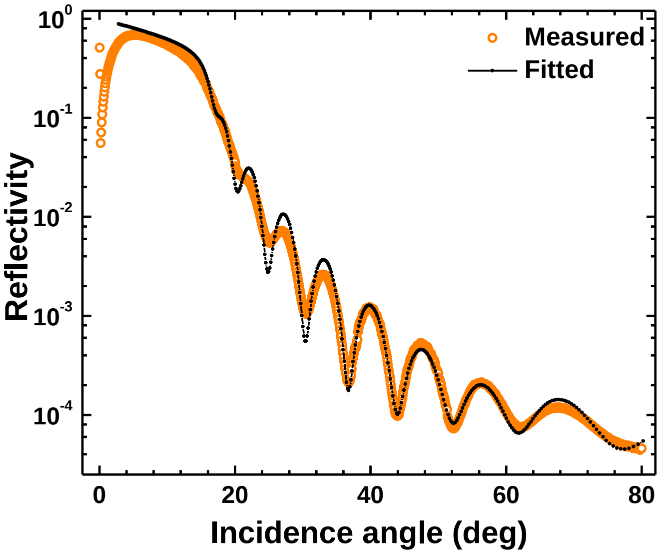

Figure 3.2: Measured and fitted soft x-ray reflectivity data of 500Å thick NbC film using 125Å incident wavelength

3.3 Results and discussion:

Soft x-ray reflectivity vs angle measurements of a 500 Å thick NbC film are carried out at reflectivity beamline Indus-1. For the SXR measurements 125 Å incident wavelength is used. Figure 3.2 shows the measured and fitted SXR curves. A three layer model is used to fit the SXR data. The model comprised of a native oxide layer of ~ 20 to 30 Å on the substrate, an ion beam deposited NbC layer and a surface layer of ~ 20 to 30 Å, formed due to contamination/oxidation with the ambient.

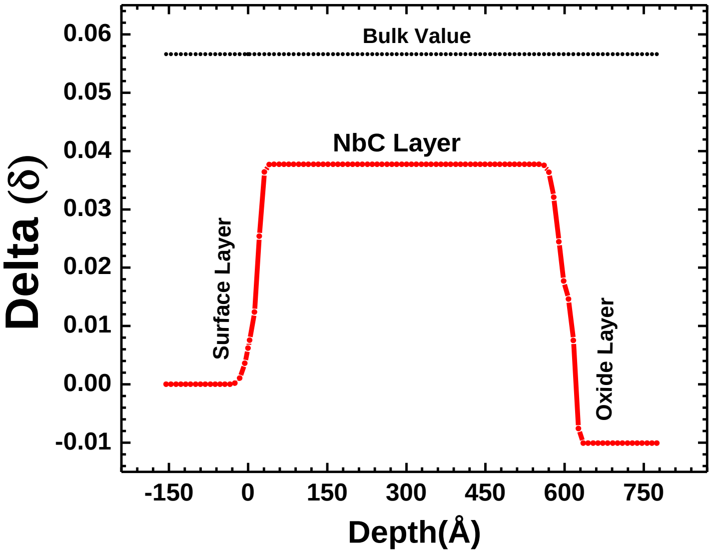

Figure 3.3: Optical density profile obtained from the fit parameters of soft x-ray reflectivity data of 500Ǻ NbC thin film is shown. For the reference, the bulk delta value is shown by dotted black horizontal line.

Further Figure 3.3 shows the optical density profile derived from fit parameters of SXR data. The optical density profile obtained for 125 Å suggests that the delta (δ) value for NbC is ~35% lower than the bulk δ value (see Figure 3.3). This decrement in optical density may deteriorate the reflectivity performance. In order to check reflectivity performance over an extended wavelength range, a reflectivity vs wavelength measurement is carried out.

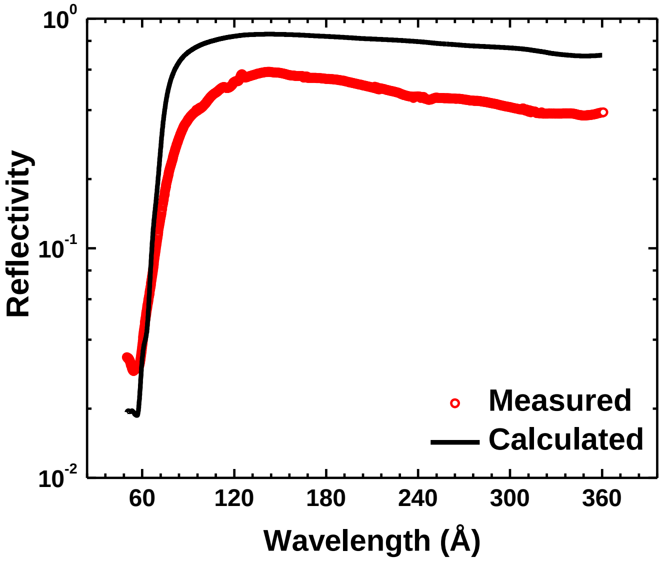

Figure 3.4: Measured and calculated SXR data of 500Å thick NbC thin film with wavelength measured at 10 degree angle. Large deviation in measured and calculated reflectivity can be observed.

Figure 3.4 shows the reflectivity vs wavelength measurements carried out in soft x-ray wavelength range of 50-360 Å at 10 degree incident angle along with the calculated spectrum. For the reflectivity vs wavelength calculation, the thickness and roughness value obtained from angle scan SXR data are used. It is evident from Figure 3.4 that the experimentally measured reflectivity shows the significant deviation of ~ 30% from the calculated reflectivity. To understand this discrepancy between measured and calculated reflectivity, we have performed a detailed structural analysis of NbC thin films using several experimental techniques. For studies or structural parameter a set of NbC thin films of different thicknesses (100 Å, 200Å, 300Å and 500Å) of are deposited.

To determine the structural parameters such as film thickness, rms roughness and the density of thin films, XRR measurements are carried out. Figure 3.5 shows the measured and fitted XRR curves versus wave vector q_z for four samples of NbC thin films of different thicknesses as described in Table 3.1. In Figure 3.5, the XRR curves corresponding to 200 Å, 300 Å and 500 Å are shifted vertically by multiplying a constant number for the sake of clarity. The well resolved Kiessig fringes in Figure 3.5 suggest that the interfaces in the thin films have sharp density gradient and low surface roughnesses. Critical angle region is highlighted in the Figure 3.5, which is used to calculate thin film mass density. A three layer model (the same as used in SXR analysis) is used to fit the XRR data. Scattering length density (ρ) and the imaginary part of the scattering length density Im (ρ) are calculated from the optical constants δ and β. These calculated ρ and Im (ρ) are used as starting parameters for the analysis of XRR data. Im ρ is kept fixed as absorption in hard x-ray region is negligible. After rigorous fitting of the XRR data the film thicknesses, roughnesses and density values are obtained and are listed in Table 3.1.

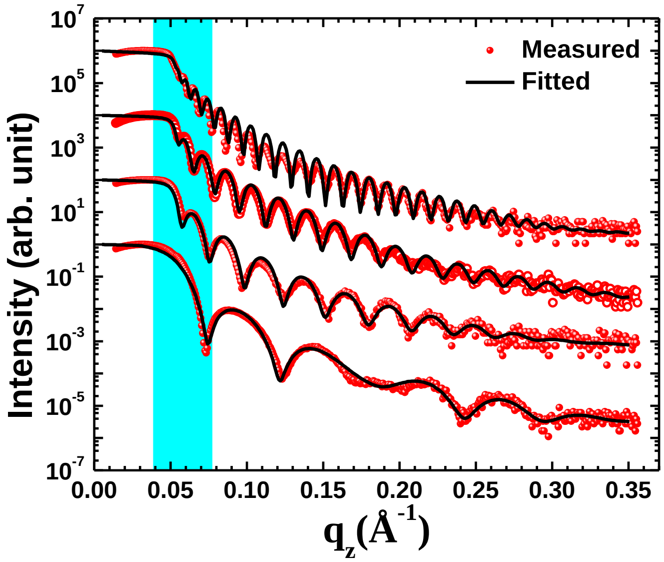

Figure 3.5: Measured and fitted XRR data of different NbC thin films of **a)** 100Å, **b)** 200Å, **c)** 300Å and **d)** 500Å thicknesses. Curves are shifted vertically for the sake of clarity. Critical angle region is highlighted.

As listed in Table 3.1 the thickness of NbC films are found 107 Å, 219 Å, 311 Å and 529 Å respectively. The density of sample (a) 107 Å thickness film is found to be 6.13 g/cm^3, which is significantly lower than the bulk value (7.82 g/cm^3). For 219 Å thick film the density is found 6.49 g/cm^3, for 311 Å film it is 6.86 g/cm^3 and for 529 Å thick film it is 7.11 g/cm^3.

Table 3.1: Structural parameters obtained from the fitting of XRR data.

Sample	Surface Layer		NbC Layer			Oxide Layer	
	Thickness (Å)	Roughness (Å)	Thickness (Å)	Roughness (Å)	Density (g/cm^3)	Thickness (Å)	Roughness (Å)
(a)	19±0.24	6.5±0.23	107±1.4	5.6±0.26	6.13±0.17	16±0.20	6.0±0.25
(b)	18±0.23	7.9±0.18	219±2.8	4.7±0.31	6.49±0.18	40±0.52	7.9±0.18
(c)	15±0.19	5.4±0.27	311±4.0	4.8±0.31	6.86±0.19	32±0.41	7.9±0.18
(d)	18±0.23	7.9±0.18	529±6.8	5.9±0.25	7.11±0.19	40±0.52	7.9±0.18

The density of NbC thin films is found to be increasing with increase in the film thickness. As the film thickness increases, the density approaches to the bulk value. The density of NbC films obtained in this case is significantly higher than that obtained by other workers[86]. Achieving near bulk density is advantageous for making x-ray thin film/multilayer devices as higher density increases the optical contrast.

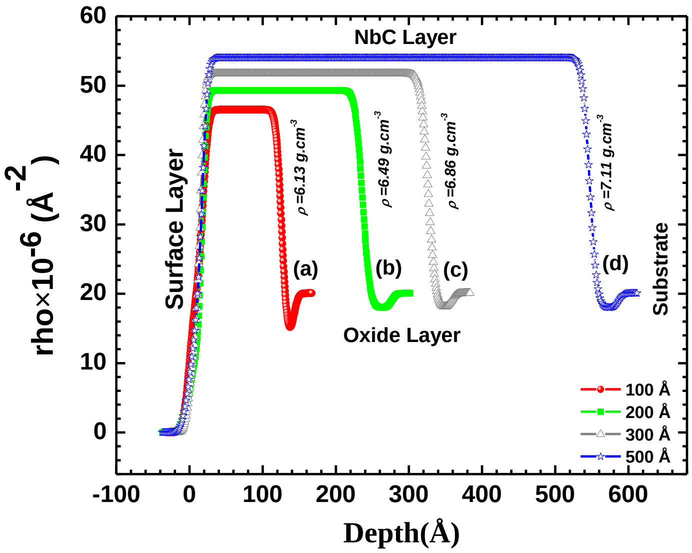

Figure 3.6: SLD profile derived from the XRR fit parameters of NbC thin films of thicknesses: **(a)** 100Ǻ, **(b)** 200Ǻ **c)** 300 Ǻ and **d)** 500Ǻ.

Further Figure 3.6 shows the scattering length density (SLD) profile derived from the fit parameters of XRR data, where curves a), b), c) and d) corresponds to the NbC thin films of different thicknesses as listed in Table 3.1. From the SLD profiles, it is clear that thin films are uniform across the depth. Near the surface region the change in density is because of film's reaction with ambient. RMS roughnesses of NbC samples are found to be in the range of 3 to 6 Å, suggesting that films have smooth surface morphology.

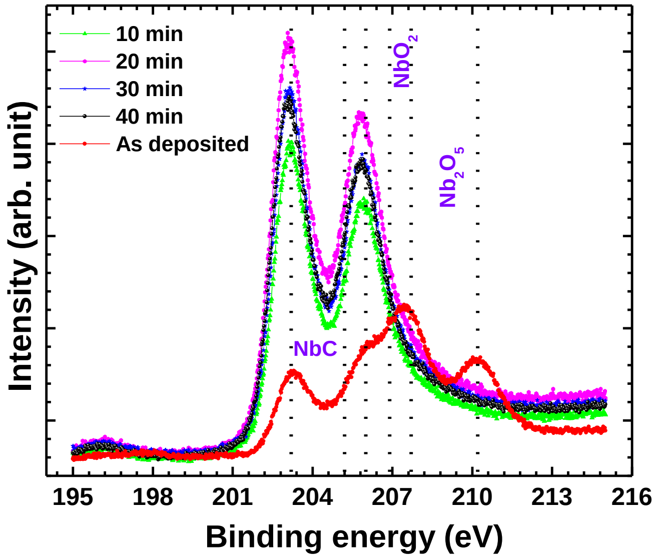

Figure 3.7: XPS spectrum for Nb 3d region acquired from NbC thin film of thickness 500Å after various sputtering times.

Further to determine the elemental composition and chemical stoichiometry of thin films across the depth, XPS measurements were carried out. Figure 3.7, Figure 3.8 and Figure 3.9 shows the XPS spectra (as deposited, and after various sputtering times) for 500 Å NbC thin film for Nb 3d, C 1s and O1s levels, respectively. Vertical lines represent the binding energy for various phases obtained from NIST XPS database[92] for NbC. XPS are de-convoluted using Gaussian de-convolution method and percentage contributions of various phases from different cores (Nb 3d, C 1s and O 1s) are obtained.

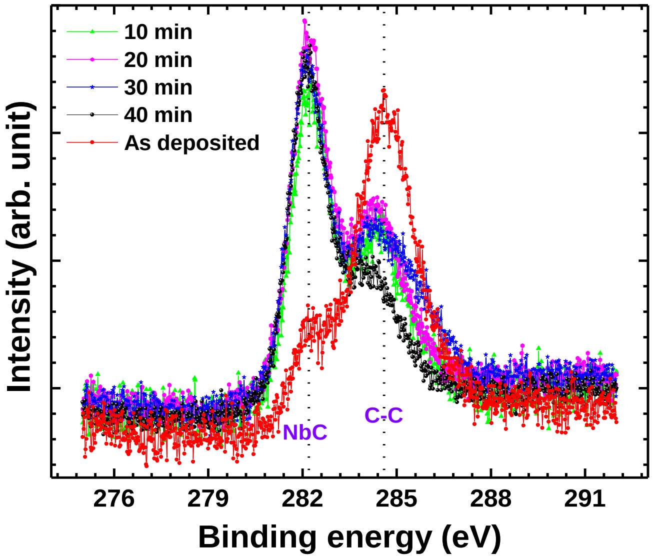

Figure 3.8: XPS spectrum for C 1s region acquired from NbC thin film of thickness 500Å after various sputtering times.

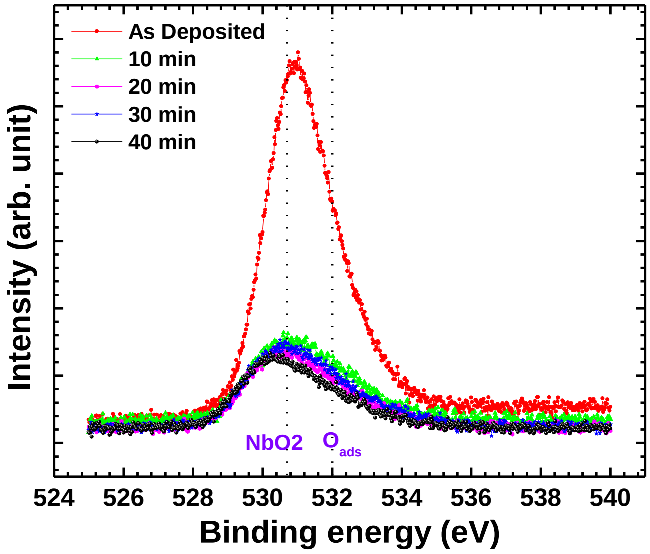

Figure 3.9: XPS spectrum for O 1s region acquired from NbC thin film of thickness 500Å after various sputtering times.

Etching rate is determined from XRR data after various sputtering and found to be 3-4 Å per minute. From the analysis of Nb core, XPS spectra percentage composition of NbC and NbO_2 are determined. In as deposited Nb core XPS data NbC is found 25.08% with 51.05%

Nb_2O_5 and 23.05% NbO_2, suggesting the presence of significant oxides on the surface. After the first sputtering cycle (10 minutes) the peak corresponding to Nb_2O_5 phase disappeared and NbC contribution is significantly increased to ~77% with simultaneous decrease in NbO_2 to 23%, which suggest that the top contamination layer is significantly reduced in 10 minutes of sputtering, since the etching rate is 3 – 4 Å per minute. In literature it has been reported that at room temperature, NbO_2 exists predominantly under the Nb_2O_5 layer rather than as point defects in Nb_2O_5 matrix.[41]

Table 3.2: The atomic percentage of elements in various phases detected from a NbC thin film of 500Å (BE-binding energy, O_{ads}-adsorbed oxygen).

Coating	**Nb (3d)**			**C (1s)**			**O (1s)**		
	Phase	**at%**	**BE (eV)**	**Phase**	**at%**	**BE (eV)**	**Phase**	**at%**	**BE (eV)**
NbC **As-deposited**	NbC NbO_2 Nb_2O_5	25.08 23.05 51.87	203.28 (3d5/2) 206.94 (3d3/2) 205.23(3d5/2) 206.03 (3d3/2) 207.71 (3d5/2) 210.16 (3d3/2)	NbC C	6.86 93.14	282.2 284.6	NbO_2 O_{ads}	57.72 42.28	530.7 532
NbC **Sputter etched 10 min**	NbC NbO_2	77.0 23.0	203.14 (3d5/2) 205.58 (3d3/2) 206.16(3d3/2) 207.60 (3d5/2)	NbC C	60 40	282.2 284.3	NbO2 O_{ads}	54.44 45.56	530.4 531.8
NbC **Sputter etched 20 min**	NbC NbO_2	82.19 17.81	203.16 (3d5/2) 205.68 (3d3/2) 206.60 (3d5/2) 208.38 (3d3/2)	NbC C	56.77 43.23	282.2 284.3	NbO_2 O_{ads}	55.17 44.83	530.5 532.3
NbC **Sputter etched 30 min**	NbC NbO_2	82.24 17.76	203.19 (3d5/2) 205.80 (3d3/2) 206.49 (3d5/2) 208.31 (3d3/2)	NbC C	35.84 64.16	282.2 284.3	NbO_2 O_{ads}	57.44 42.56	530.5 532
NbC **Sputter etched 40 min**	NbC NbO_2	81.86 18.14	203.1 (3d5/2) 205.66 (3d3/2) 206.45 (3d5/2) 208.29 (3d3/2)	NbC C	41.26 58.74	282.2 284.9	NbO_2 O_{ads}	58.38 41.62	530.2 531.8

The inelastic mean free path of the electrons for Al K-α radiation is ~20 Å. After further sputtering of 40 minutes the NbC contribution is ~82% with slight oxide of ~18%. Similarly compositions of different phases are determined from the C and O 1s cores respectively and results of those are tabulated in Table 3.2. From the various obtained phases, the elemental concentration of Nb, C and O are determined. Elemental concentration obtained from the analysis of XPS spectra are shown in Figure 3.10.

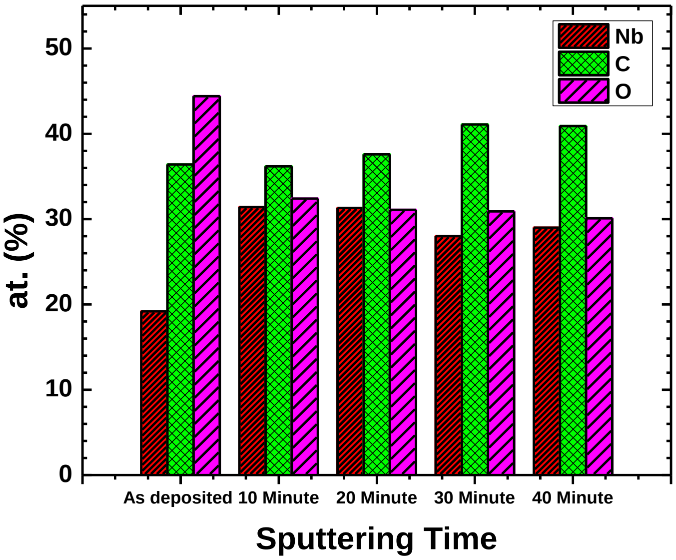

Figure 3.10: Elemental concentration obtained from the XPS data analyses after different sputtering cycle is shown.

In the as deposited XPS spectrum of Nb 3d core, Nb_2O_5 and NbO_2 phases are dominating. This suggests that significant amount of contamination is present on the top surface, which can also be confirmed in XPS spectra of C 1s and O 1s core. Intense C-C and $O_{adsorbed}$ peaks in C and O cores suggest that significant amount of carbon and oxygen contamination is present on the top surface. This contamination on top surface is also observed in SXR and XRR data also (see Figure 3.3 and Figure 3.6). This contamination layer is mainly because of reaction of top surface with the ambient. It is evident from Figure 3.10 that after 10 minutes of sputtering, the oxygen concentration reduced significantly while the carbon concentration do not reduced much. This high carbon concentration compared to Nb after sputtering is because of the presence of unreacted carbon. Across the depth, of the film Nb concentration increased from 19% to 29% with decrease in O concentration 44.4 at.% to 30at.%. A constant O (~30 at.%)

after 10 minute sputtering can be accounted mainly from the experimental chamber and partially from the diffusion of oxygen through voids and pores existing in film structure since very less amount of NbO_2 ~18 % is found from Nb 3d core. The XPS analysis showed that thin film contains NbC as dominated phase, with some amount of free carbon across the depth.

The surface morphology of thin films is characterized by the rms roughness. RMS roughness is also a function of spatial frequency. Several techniques like (XRR, AFM etc.) are used to study the surface roughness in various spatial frequency regions. In present case, to investigate the surface morphology of NbC thin films, AFM measurements are carried out. AFM images taken over different length scales are combined to generate a single PSD in the large spatial frequency range. Figure 3.11 shows the noise free smooth PSD functions of NbC thin films. From the PSD analysis the rms roughness values are calculated and found less than 6 -9 Å, which are in close agreement to the roughness value obtained from the XRR data.

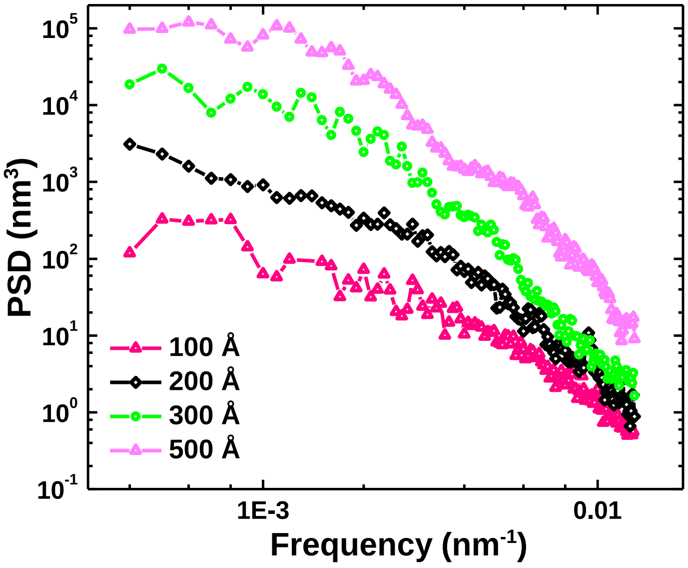

Figure 3.11: PSD of the NbC thin films of different thickness. The average PSD function was obtained by averaging several PSDs calculated on several line profiles from topographic data.

Further to investigate the crystalline state of NbC thin films, GIXRD measurements are carried out. Figure 3.12 shows the GIXRD curves of NbC thin film of three different sample (b), (c) and (d) for NbC films (see Table 3.1). Vertical lines in the figure represent the position and intensity of XRD peaks corresponding to NbC powder reported in JCPDS data base (#100181). The 2θ values of JCPDS data have been modified for experimental wavelength (1.234 Å) and matches well with observed peak positions. In GIXRD curve **b)** (300Ǻ film) a hump is seen because of Si substrate (as marked in figure), which is dominating in the GIXRD curve **a)**. Si feature was more prominent in 100Ǻ sample and NbC pattern was not discernible. GIXRD data suggests that the NbC thin films are polycrystalline, but no quantitative information about the structure and density could be obtained.

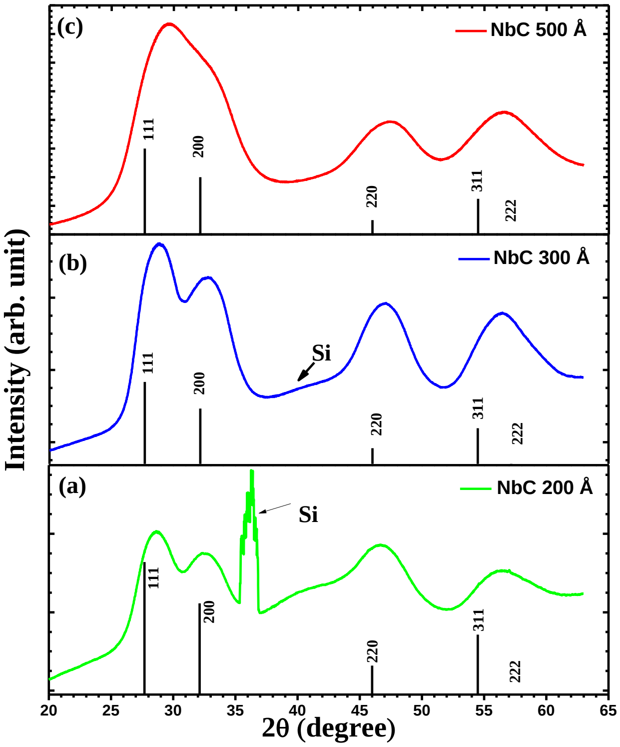

Figure 3.12: GIXRD pattern acquired from NbC thin films of different thicknesses. The vertical lines correspond to calculated data from JCPDS for standard NbC powder.

Further to investigate the local structure and correlate the increasing film density with thickness XANES and EXAFS measurements are carried out. K-edge XANES spectra are routinely used to determine oxidation state of compound materials where there are possibilities of different compound formation during growth. In the present study, Nb K-edge XANES spectra have been measured for NbC samples (a), (c) and (d), and then compared with spectra of standard NbO_2 (Nb^{4+}) and Nb_2O_5 (Nb^{5+}) commercial powders. Figure 3.13 (a) shows Nb K-edge XANES spectra of Nb metal foil, NbO_2, Nb_2O_5 and NbC thin films as a function of film thickness. Figure 3.13 (b) shows the first derivative of Nb K-edge for NbC thin film as well as Nb^{4+} and Nb^{5+}references. NbC thin film XANES spectra reveal that the Nb edge position has been shifted towards higher energy than Nb metal foil and 1st derivative of Nb edge values of thin films matches with Nb^{4+}, this suggests that the valence state of is +4.

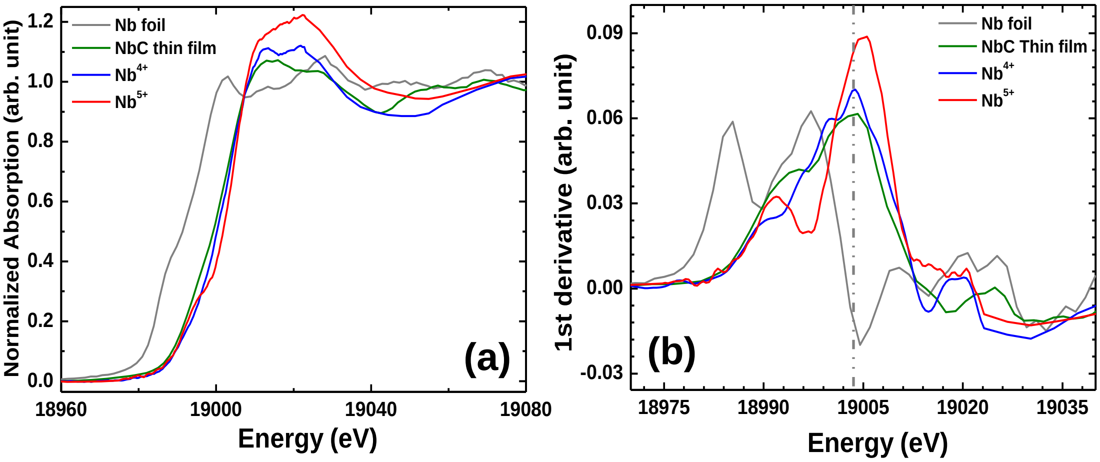

Figure 3.13: Normalized XANES spectra at NbC K-edge for Nb foil, NbO_2, Nb_2O_5 and NbC thin films of different thicknesses. In the inset first derivative of XANES data is shown.

To understand the local structure of NbC in the form of thin films, Nb K-edge EXAFS spectra has been analyzed. Figure 3.14 (a) shows the best fit of the Fourier transform (FT) of $k^2\chi(k)$ experimental EXAFS data corresponding to 100, 300 and 500 Å NbC thin films. For fitting EXAFS data, NbC crystalline *Fm3m* cubic structure has been used with a lattice constant 4.470 Å. In the structure of NbC, the Nb atoms occupy the Wyckoff position (0, 0, 0) and C atoms occupy position (0.5, 0.5, 0.5). An Nb atom is surrounded by 6 C atoms at 2.235 Å distance as first near neighbor and by 12 Nb at 3.161 Å as second near neighbor. In the FT-EXAFS spectra, shown in Figure 3.14 (a), the first peak is attributed due to Nb-C and second due Nb-Nb bonds[93]. In FT EXAFS spectra in R space, the peak intensity and widths are mainly related to the following two factors **(i)** local coordination number and **(ii)** Debye–Waller factor (DWF)[94]. From fitting of EXAFS spectra we have obtained Nb-C and Nb-Nb bond distances, coordination number and DWF, which have been plotted in Figure 3.14 (b) as a function of NbC film thicknesses. As it was noticed from GIXRD that 100 Å film is amorphous, the FT-EXAFS spectrum of this film shows significantly low Nb-Nb coordination and high disorder parameter. EXAFS fitting for higher thickness films show increase in coordination number and reduction in disorder parameter corresponding to Nb-Nb near neighbor atoms.

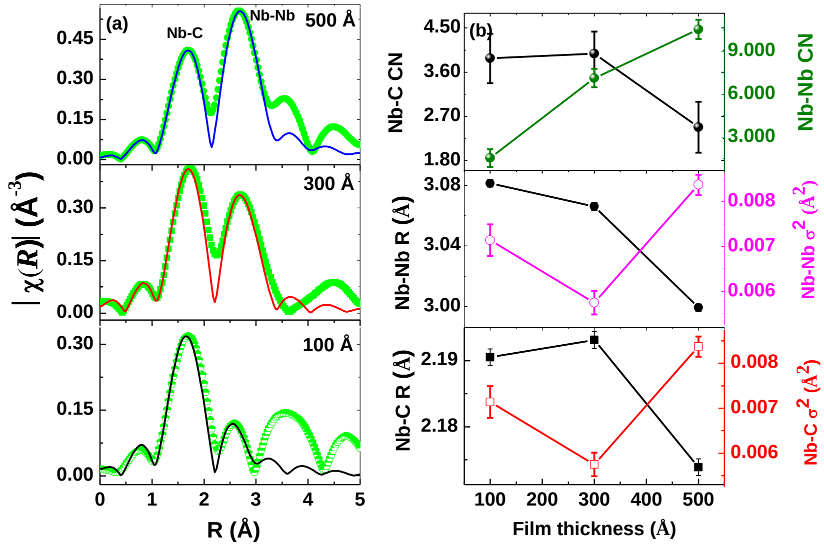

Figure 3.14: **(a)** Fourier transform of k^2-weighted experimental (circle) and fitted curves (solid line) of Nb K-edge for different thickness of NbC thin film. **(b)** Best fit plot of Nb-C and Nb-Nb bond distance (R), Debye–Waller factor (σ^2) and coordination number (CN) as a function of NbC film thickness.

As has been mentioned above, the density values obtained from XRR data for lower thickness of NbC films are significantly lower than the bulk density. This could possibly be due to lower coordination number of Nb-Nb compared to bulk coordination. Lower Nb-Nb coordination indicates the possibility of Nb vacancies, which can lower density of NbC thin film. It has been observed further from EXAFS analysis for higher thickness films, as the thickness increases, Nb-Nb coordination increases resulting in increase in film density. It may be noted that for 500 Å thick NbC film, the ratio of peak intensity for Nb-C and Nb-Nb has been reversed, approaching the bulk like behavior. The lower Nb-Nb coordination number for low thickness films may be due to the presence of unreacted carbon, as observed in the XPS analysis explained above.

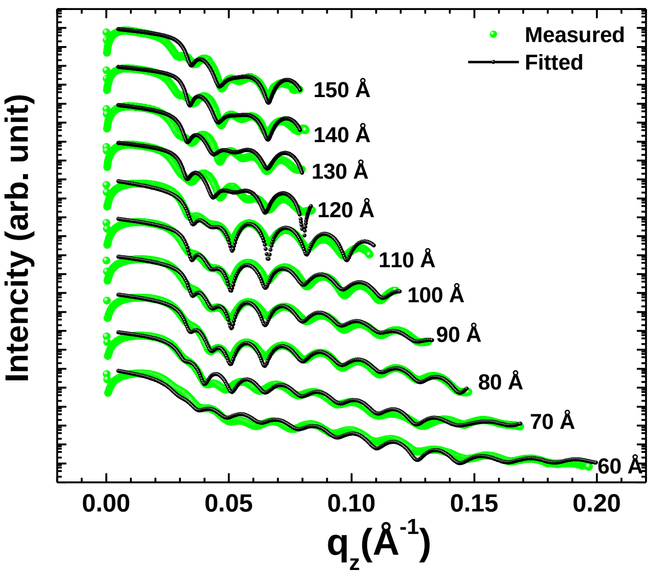

Figure 3.15: Measured and fitted soft x-ray reflectivity curves at different wavelengths. Curves are shifted vertically for the sake of clarity.

After characterization of the structural parameters, 300 Å thick NbC film has been chosen for the determination of optical constants. Structural parameters and film stoichiometry has been checked using XRR and XPS technique and has been discussed in above section. After pre-characterization of NbC film, SXR measurements are carried out in 60-150 Å wavelength region.

Measured and fitted SXR curves are shown in Figure 3.15. A three layer model (1-oxide layer, 2-principal NbC layer and 3- surface/contamination layer) as used for XRR data analysis is used to fit the SXR data. To obtain reliable values of optical constants and to reduce number of fit parameters, thickness and roughness values are kept fixed as obtained from XRR data.

The accuracy of optical constants determined from XRR technique depends on β/δ ratio[95]. If this ratio is less than one ($\beta/\delta<<1$), critical angle θ_c can be calculated from the $\theta_c=\sqrt{2\delta}$ relation, because the reflectivity pattern has a well-defined shoulder. For β/δ approaching to one, the reflectivity pattern becomes exponential like. Further if the ratio is greater than one ($\beta/\delta>1$) the critical angle region in reflectivity pattern is not distinguishable and it is not possible to determine δ and β uniquely. So for the region with $\beta/\delta>1$, the uncertainty in determination of δ and β is very high. The experimentally measured optical constants for NbC are listed in Table 3.3.

Table 3.3: Derived optical constants of NbC in the 60-150 Å wavelength region, along with Henke's tabulated values

Wavelength (Å)	**δ (Henke)**	**δ (Exp)[£]**	**β (Henke)**	**β (Exp)[£]**
60	0.0075	0.007(5)	0.00251	0.002(7)
70	0.0135	0.0124(8)	0.00244	0.002(7)
80	0.0194	0.0163(9)	0.00298	0.003(1)
90	0.0258	0.0250(1)	0.00350	0.0037(6)
100	0.0331	0.0302(4)	0.00400	0.0039(2)
110	0.0414	0.036(6)	0.00415	0.0057(4)
120	0.0512	0.036(7)	0.00507	0.005(9)
130	0.0628	0.043(3)	0.00609	0.008(1)
140	0.0759	0.052(8)	0.00807	0.006(9)
150	0.0907	0.062(8)	0.01114	0.009(9)

[£] For the experimental δ and β values the uncertainties in last significant digit are given in parentheses.

Further Figure 3.16 shows the measured optical constants along with tabulated Henke's data in 60-150 Å wavelength range. The error in last significant digit determined from least square refinement procedure is mentioned in the parenthesis in the table. It is obvious that, the β/δ ratio in whole wavelength region is less than one suggesting that uncertainty in determination of *δ* and *β* is minimum. Significant deviation in experimentally derived and tabulated bulk values of *δ* and β values are found, specially at higher wavelengths (110-150Å). The deviation in *δ* values is around 5 to 31%, while deviation in β values is 5-38 %.

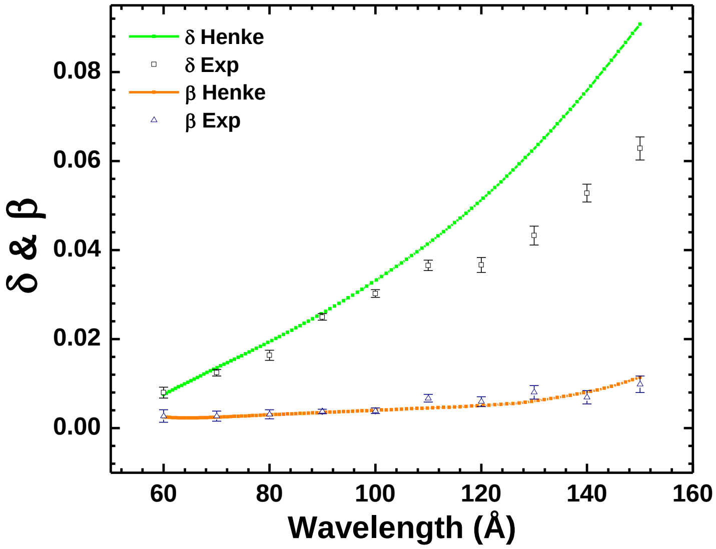

Figure 3.16: Measured optical constants of NbC shown as discrete points, along with the error bars. Solid curves correspond to Henke database for comparison.

It may be noted in Figure 3.16 mismatch in δ and β values is more after 120 Å. Mismatch in delta values is significantly high compared to beta values in whole wavelength region. This could be understood from the analysis of atomic scattering factor for Nb and C separately. Figure 3.17 shows real and imaginary part of atomic scattering factor (from CXRO website) f_1 and f_2 for Nb and carbon in soft x-ray region. Figure 3.17 suggest that f_2 values of Nb and C are very close in the wavelength range of 50-200Å, whereas the f_1 values of these two elements are significantly different. This suggest that the change in Nb:C ratio from 1:1 at near surface will not affect the beta value much but it will change the delta value significantly.

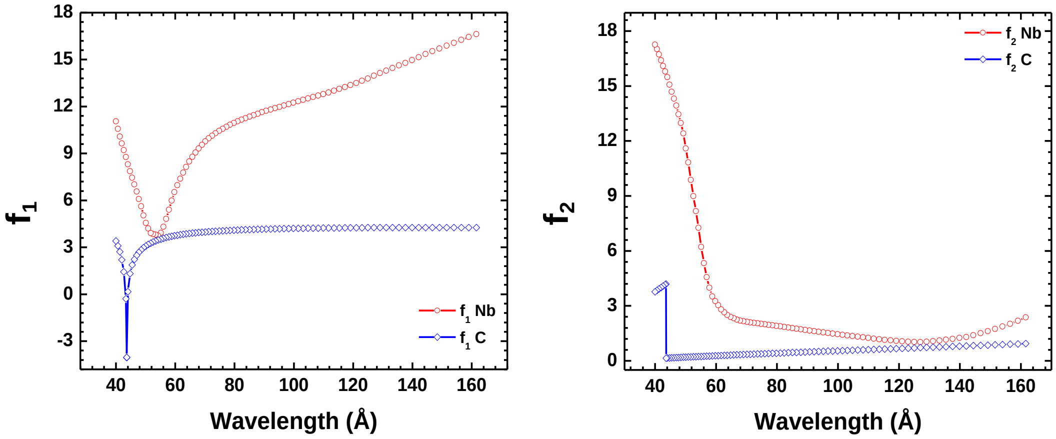

Figure 3.17: f1 and f2 for Nb and C in soft x-ray wavelength region of 40 – 160 Å.

In our case the lower delta value in higher wavelength range indicates that the NbC film do not have 1:1 ratio of Nb and C especially in near surface region, which is also confirmed by XPS data as discussed above.

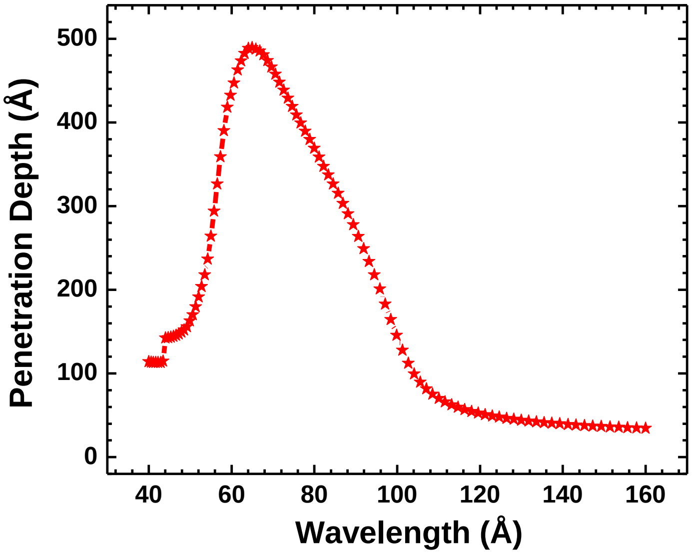

Figure 3.18: Penetration depth of NbC in 40 to 160 Å wavelength region at 15 degree incidence angle

Further Figure 3.18 shows penetration depth in 40-160 Å wavelength region at 15° incidence angle. The curve for penetration depth suggest that the photons of >120Å wavelength penetrates up to ~40Å in NbC. In this situation, the surface region will predominantly affect the optical constant behavior of ion beam deposited NbC. Because of growth process and reaction with ambient the surface of NbC thin film could have a large deviation in Nb:C ratio and leading to reduction the δ value with nominal change in β value.

The present study suggests before using compound material NbC in actual optical devices, it is essential to study the structural and optical properties. The main conclusions obtained from the present study are explained below.

3.4 Conclusions:

NbC is found to be suitable candidate for the fabrication of soft x-ray multilayer for high reflectivity performance near Si edge. Structural and optical properties NbC thin films are studied for x-ray multilayer application. Following are the main inferences of the aforementioned study.

- ✓ Significant mismatch of ~30% in measured and theoretically calculated SXR versus wavelength data are found.

- ✓ High density and low roughness NbC thin films are deposited, which is an advantage for making x-ray multilayers. Density of NbC films is found to be increasing with increase in film thickness. RMS surface roughness for all the thin films is found in 3-6 Å range, which suggest smooth surface morphology of NbC thin films.

- ✓ XPS measurements after various sputtering cycle suggests that some amount of unreacted carbon and oxygen is present in the depth of the NbC film.

- ✓ XANES spectra of NbC thin films revealed that Nb in NbC films are in +4 oxidation state. EXAFS data shows that Nb-Nb coordination increases with increase in the film thickness.

- ✓ Optical constants of NbC in 60-150 Å wavelength region are measured. The δ values are found 5 to 30 % lower than the bulk value whereas deviation in beta values are found to be in close agreement to Henke's tabulated values.

Chapter 4.

Study on Structural and Optical Properties of ZrC

In this chapter, influence of structural disorder on soft x-ray optical response of compound material ZrC is investigated and optical constants of ZrC in 60-200 Å wavelength region are determined. A discrepancy in soft x-ray performance of ZrC film is observed, which could not be explained with Henke's tabulated data. To understand this detailed structural and chemical characterizations are carried out using XPS, SXR, XRR, GIXRD and AFM techniques. Results obtained are described in this chapter.

4.1. Introduction:

In Chapter-3 it has been discussed that the structural and optical properties of thin films of compound material need to be investigated before their practical use in multilayer mirrors. Structural properties and optical constants of NbC thin films were determined near Si L- edge region (124 Å). In the present chapter a detailed work is carried out to analyze structural and optical properties of ZrC compound material. Zr/Al multilayer mirrors are used as reflection mirror in soft x-ray energy region 170-190 Å. However this combination (Zr/Al) is thermally unstable above 200°C and intermixing and alloy formation of Al-Zr alloy is reported[29]. As discussed in last chapter the transition metal carbide layers are non-stoichiometric, and contain significant amount of free carbon, which acts as barrier layer to avoid intermixing in multilayer mirrors. To improve the thermal stability of a multilayer mirror the elements should be replaced by a suitable compound material based on their optical properties.

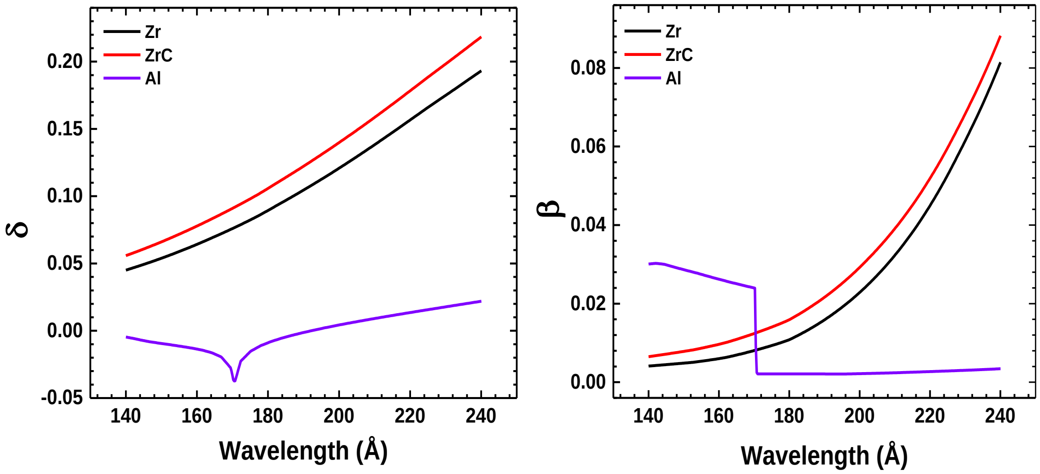

Figure 4.1: Comparison of the optical constants of ZrC and Zr with Al in 140-240 Å wavelength region is shown. Delta beta contrast for ZrC and Al is better suggesting it a better choice over Zr.

Further ZrC belongs to group-V transition metal carbides and have several applications such as in nuclear fuel, thermo voltaic reactor, field emission cathode etc.[96,97,98]. Since the optical constants of ZrC are similar to Zr in soft x-ray energy region, it may be used as a replacement to elements in Zr/Al multilayer mirrors. In Figure 4.1 optical constants of Zr, ZrC and Al are shown in 140 - 240 Å wavelength region, calculated from CXRO database[84]. From Figure 4.1 it is clear that the optical constant contrast between ZrC and Al is better than the contrast between Zr and Al. Therefore ZrC/Al multilayer should exhibit better reflectivity as compared to Zr/Al multilayer mirror with improved thermal stability. The reflectivity of a material depends on several growth related parameters. When thin films of compound materials are deposited from the bulk targets, the structural properties get modified.

The density of the film is an important parameter in case of soft x-ray multilayers. If the density of the film is less than the bulk density, reflectivity drops down significantly. When thin films are formed from bulk target of a compound material, density is found to be less than the bulk density and structural properties get modified because of change in near neighbor environment. If the chemical stoichiometry varies, the optical properties get modified, which affect the optics performance. Hence the compound materials must be investigated thoroughly for their structural and optical performances by pursuing a detailed scientific study prior to their use in actual applications.

Depositions of high quality ZrC thin films are difficult due to their unusual properties such as high melting point, low evaporation and sputtering rate, high reactivity of Zr with oxygen and water vapors. In literature few studies on structural properties of ZrC deposited using several techniques such as physical vapour deposition, chemical vapour deposition, DC magnetron sputtering, e-beam evaporation, pulsed laser deposition (PLD) etc.are available. In PLD technique laser fluence around $10 J/cm^2$ is required for the deposition of metal carbide films which is difficult to be implemented[85]. Deposition of high quality ZrC films requires optimization of several deposition parameters to obtain high density and low surface roughness.

Cracium et al.[99] have deposited ZrC thin films using the PLD technique for application in hard coating. They obtained a reasonable low density of 5.8 g/cm^3 for the films deposited near room temperature (~30°C). They have achieved highest density of 6.6 g/cm^3 at substrate temperature 500°C. Near bulk density was obtained at a higher thickness of 1650Å by PLD technique[100].

In this chapter structural and optical properties of ZrC thin films are investigated using several experimental techniques. Optical constants in soft x-ray energy region have been determined from reflectivity vs angle measurements performed in 40-200Å wavelength range. Details of the experimental findings are discussed.

4.2. Experimental:

4.2.1. Sample Preparation:

Thin films of ZrC (typically 100Å, 200Å, and 300Å) have been deposited on a polished Si (100) wafer using ion beam sputtering technique. Prior to deposition a base pressure of 3×10^{-5} Pa was achieved. Deposition have been carried out under argon ambient at constant pressure of 6×10^{-2} Pa. A commercially available 4 inch sputtering target of ZrC (99.99% purity) have been used for deposition. After process optimization, it has been found that the films deposited at 1000 V beam voltage and a gas flow rate of 3 standard cubic centimeters per minute are better in rms roughness. These optimized parameters have been used for the deposition of all the samples.

4.2.2. Optical Characterization:

For optical characterization of ZrC thin films soft x-ray reflectivity (SXR) measurements have been carried out using reflectivity beamline as discussed in Chapter-3. For ZrC thin film reflectivity vs angle scan have been performed in 0-65° incident angle and in 60-

200 Å wavelength region. Reflectivity vs wavelength scan have been carried out in 60 to 360 Å region at 10° incident angle.

4.2.3. Structural characterization:

For determination of the chemical composition/film stoichiometry and Zr:C ratio, XPS measurements are carried out as discussed in Chapter-3.

Further to investigate thickness, roughness and density of ZrC thin films, XRR measurements are carried out and details are discussed in Chapter-3.

For the investigation of surface morphology ZrC thin films, AFM measurements are carried out over 1×1, 2×2, 5×5 and 10×10 μm^2 range. Further details are discussed in Chapter-3.

Crystalline state of ZrC thin films is determined using GIXRD measurements. Further details for the measurements are explained in Chapter-3.

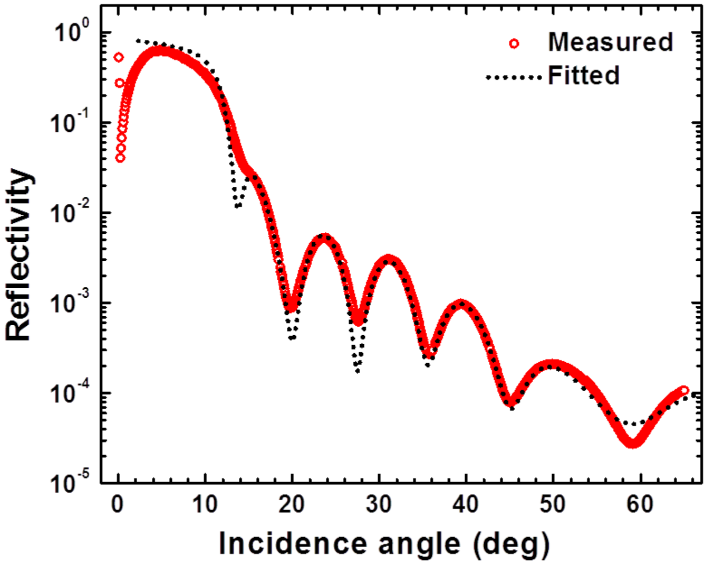

Figure 4.2: Measured and fitted soft x-ray reflectivity data of 300Å ZrC thin film measured at 100Å wavelength.

4.3. Results and discussions:

To check the optical response of ZrC thin films, soft x-ray reflectivity vs angle measurements are carried out using reflectivity beamline at Indus-1 synchrotron source. SXR measurements are carried out on a 300 Å thick ZrC thin film using incident wavelength λ=100 Å. Figure 4.2 shows the measured and fitted SXR curves for ZrC thin film. For the analysis of SXR data a three layer model is used. The model comprised of a native oxide layer of 20-30 Å on substrate, ion beam deposited ZrC layer and a surface layer of 20-30 Å, formed due to contamination/oxidation with the ambient.

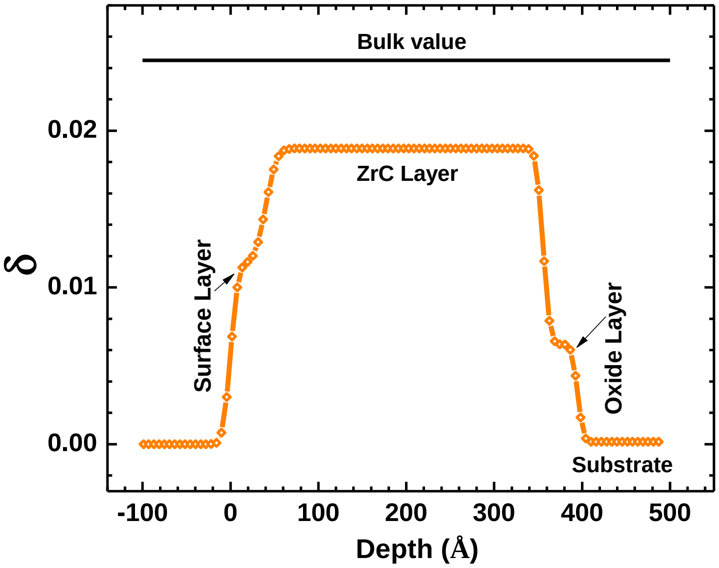

Figure 4.3: Optical density profile obtained from the fit parameters of soft x-ray reflectivity data of 300Å ZrC thin film. Bulk delta value is shown in dotted black line.

Further Figure 4.3 shows the optical density profile derived from fit parameters of SXR data, where a black horizontal line represents the bulk δ value for ZrC material. The optical density profile suggests that the δ value of ZrC for 100 Å wavelength is ~22% lower than the bulk δ value (see Figure 4.3). In order to check the reflectivity performance over an extended wavelength range, a reflectivity versus wavelength measurement is carried out in 45-90 Å range at 5° incident angle, result of that are shown in Figure 4.4. A calculated reflectivity spectrum using optical constants value obtained from CXRO database is also shown. Thickness and roughness values obtained from angle scan SXR data are used for calculation of reflectivity vs wavelength curve. It is evident from the figure that the experimentally measured reflectivity curve shows a large deviation from simulated reflectivity curve. The deviation is around 9 to 30%. To understand this anomaly between measured and calculated spectra, a detailed structural analysis is carried out using several experimental techniques. For the structural studies a set of thin films of different thicknesses (100 Å, 200Å, and 300Å) of ZrC are deposited.

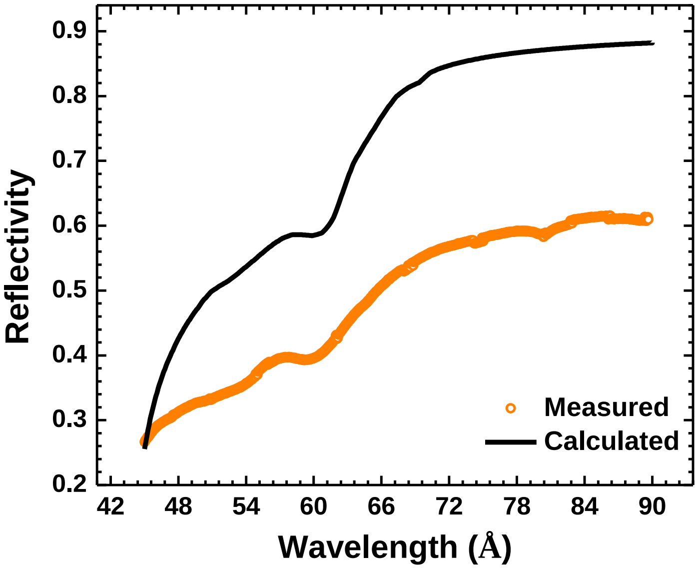

Figure 4.4: Measured and calculated SXR data of 300Å thick ZrC thin film with wavelength measured at 5 degree angle

Structural parameters such as thickness, roughness and density of thin film are obtained from XRR measurements. Figure 4.5 shows the measured and fitted XRR curves (using 1.54 Å wavelength) of ZrC thin films of different thicknesses as listed in Table 4.1. Here XRR curves corresponding to 200 Å and 300 Å thicknesses are shifted vertically by multiplying a constant number for the sake of clarity. The well resolved Kiessig fringes in Figure 4.5 suggest that the interfaces in the thin films have sharp density gradient and low surface roughnesses. Critical angle region is highlighted in the Figure 4.5, as this gives information of thin film mass density.

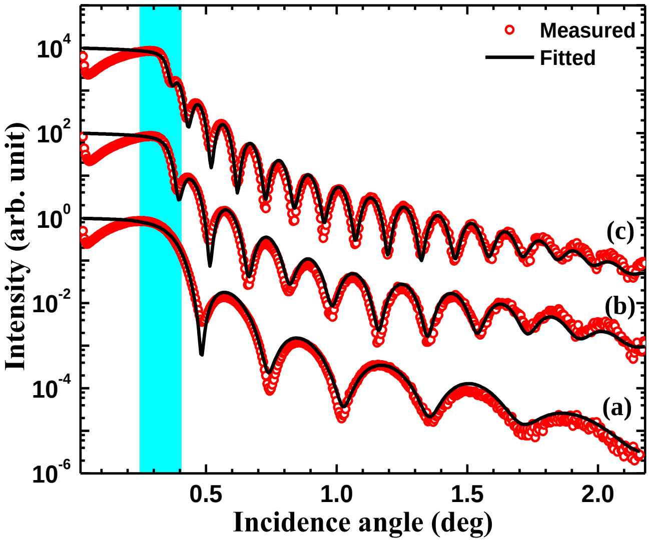

Figure 4.5: Measured and fitted XRR data of different ZrC thin films of a) 100Ǻ, b) 200Ǻ and c) 300Ǻ thicknesses. Curves are shifted vertically for the sake of clarity. Critical angle region is highlighted.

A three layer model (the same as used in SXR analysis) is used to analyze the XRR data. Scattering length density (ρ) and imaginary part of the scattering length density Im (ρ) are calculated from optical constants δ and β obtained from CXRO database. These calculated ρ and Im (ρ) are used as initial parameter for the data analysis. Im ρ is kept fixed as absorption in hard x-ray region is minimum. After rigorous fitting of XRR data film thickness, roughness and density values are obtained. All the fit parameters (thickness, roughness and density) obtained from XRR data analysis are compiled in Table 4.1. The density of different ZrC thin films of different thicknesses is found to be similar as 6.51 g/cm^3, which is slightly less than the bulk value 6.73 g/cm^3. The present experimental value of ZrC thin film density is significantly higher than that obtained by other workers, where near bulk density is obtained for higher thickness of

1650Å[100]. Achieving near bulk density is advantageous for making an x-ray thin film/multilayer mirror as higher density increases the optical contrast.

Table 4.1: Parameters obtained from the analysis of XRR data.

Sample	Surface Layer		ZrC Layer			Oxide Layer	
	Thickness(Å)	Roughness (Å)	Thickness (Å)	Roughness (Å)	Density (g/cm^3)	Thickness (Å)	Roughness (Å)
(a)	30±0.39	9.1±0.16	104±1.3	3±0.5	6.51±0.17	40±0.52	3.1±0.48
(b)	28±0.36	8.2±0.18	210±2.7	5±0.3	6.51±0.17	36±0.46	2.1±0.71
(c)	29±0.37	9.0±0.16	313±4.0	6±0.25	6.51±0.17	34±0.44	3.7±0.40

Figure 4.6 shows the scattering length density profiles (SLD) of three different ZrC thin films as derived from the fit parameters of XRR data as mentioned in Table 4.1.

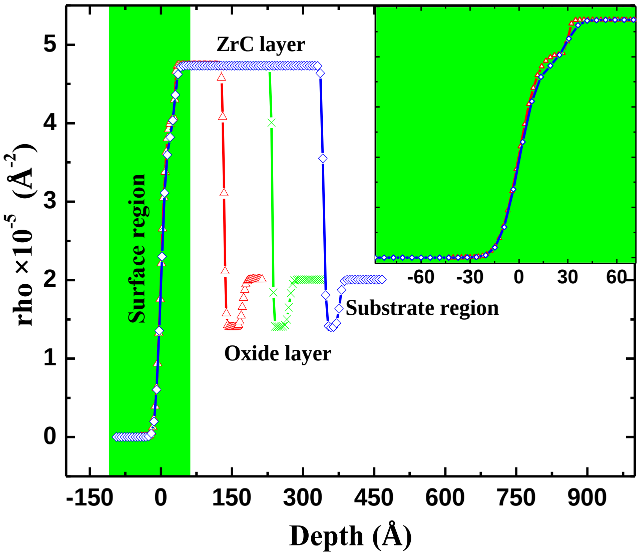

Figure 4.6: SLD derived from XRR fit of measured data of ZrC thin films: a) 100Å, b) 200Å and c) 300Å. Surface portion are zoomed in the inset.

The SLD profiles suggest that the thin films are uniform across the depth. Near the surface region of the films the change in density is because of film's reaction with ambient. The rms roughnesses of ZrC samples are found to be in the range of 3-6 Å, suggesting that the films have smooth surface morphology.

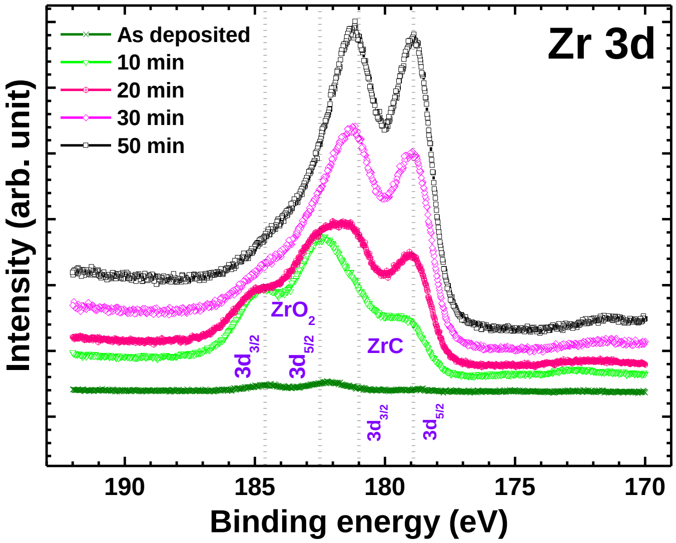

Figure 4.7: High resolution XPS spectrum for Zr 3d region acquired from ZrC thin film of thickness 300Å after various sputtering times.

To determine the elemental composition and chemical stoichiometry of ZrC thin film in the depth, the XPS measurements are performed after various sputtering cycles. Figure 4.7, Figure 4.8 and Figure 4.9 shows the XPS spectra corresponding to Zr 3d, C 1s and O 1s regions respectively. In the figure, the vertical dotted lines represent the peak positions of the binding energy of various phases obtained from NIST XPS data base[92]. In as deposited XPS spectrum the Zr 3d peak is barely visible. Presence of intense C 1s and O 1s peak suggest that the surface is strongly contaminated by adventitious carbon and formation of ZrO_2 phase. After the first sputtering cycle of 10 minutes, the Zr 3d and O 1s a signal corresponding to ZrO_2 is strongest, with reduced adventitious carbon. After 20, 30 and 50 minutes sputtering cycles, a shift in the binding energy of Zr 3d and C1s can be noted towards 179.1 eV and 281.6 eV, respectively, the values correspond to presence of ZrC[101] phase in the film. After 50 minutes of sputtering, O 1s peak is barely visible, suggesting that oxygen contamination has been reduced.

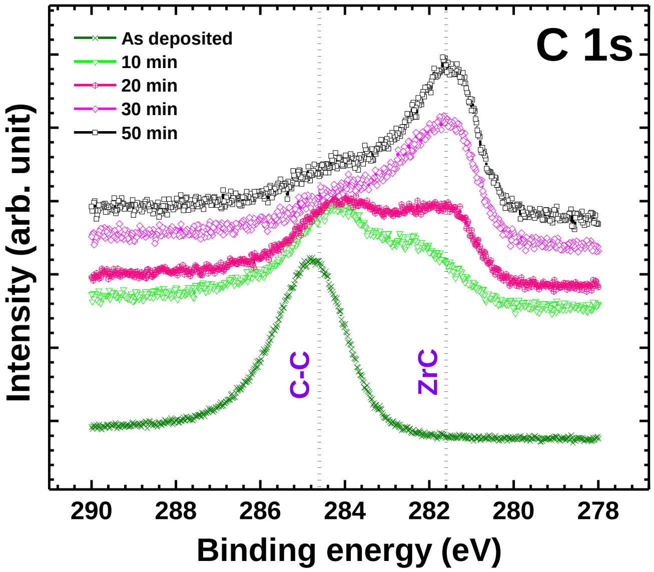

Figure 4.8: High resolution XPS spectrum for C 1s region acquired from ZrC thin film of thickness 300Å after various sputtering times.

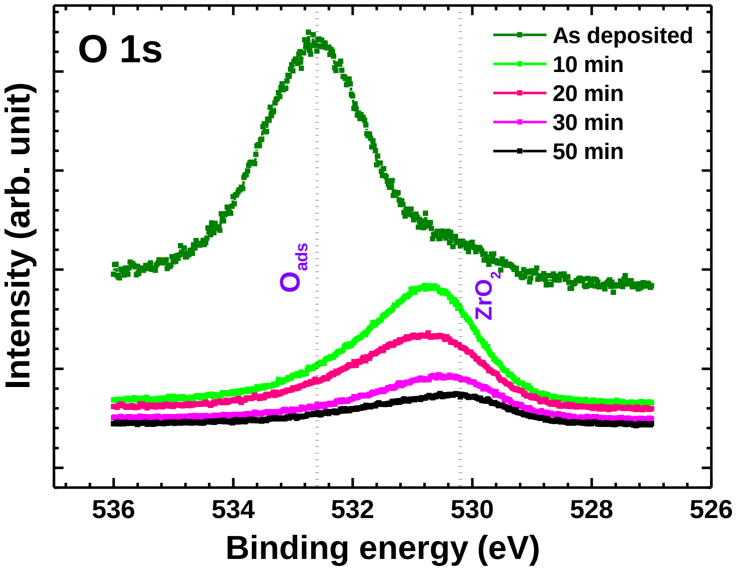

Figure 4.9: High resolution XPS spectrum for O 1s region acquired from ZrC thin film of thickness 300Å after various sputtering times.

Table 4.2: The atomic percentage of elements in various phases detected from a ZrC thin film of 300Å (BE-binding energy, O_{ads}-adsorbed oxygen).

Coating	Zr (3d)			C (1s)			O (1s)		
	Phase	at%	BE (eV)	Phase	at%	BE (eV)	Phase	at%	BE (eV)
ZrC **As-deposited**	ZrC	20.28	178.9 (3d5/2) 180.6 (3d3/2)	ZrC	1.27	282.3	ZrO_2	7.32	530.2
				C	76.01	284.7			
	ZrO_2	79.72	182.1 (3d5/2) 184.6 (3d3/2)	CO, CO_2	22.72	286.3	O_{ads}	92.68	532.6
ZrC **Sputter etched** **10 min**	ZrC	31.30	179.0 (3d5/2) 180.8 (3d3/2)	ZrC	32.20	282.5	ZrO_2	73	530.7
	ZrO_2	68.70	182.6 (3d5/2) 184.8 (3d3/2)	C	67.80	284.5	O_{ads}	27	532.2
ZrC **Sputter etched** **20 min**	ZrC	50.86	179.0 (3d5/2) 180.9 (3d3/2)	ZrC	48.20	282.1	ZrO_2	69.83	530.7
	ZrO_2	49.14	182.5 (3d5/2) 184.7 (3d3/2)	C	51.80	284.5	O_{ads}	30.17	532.2
ZrC **Sputter etched** **30 min**	ZrC	70.02	179.0 (3d5/2) 181.0 (3d3/2)	ZrC	68.30	281.8	ZrO_2	74.65	530.2
	ZrO2	29.98	182.6 (3d5/2) 194.5 (3d3/2)	C	31.70	284.4	O_{ads}	25.35	531.8
ZrC **Sputter etched** **50 min**	ZrC	75.48	178.9 (3d5/2) 181.0 (3d3/2)	ZrC	78.08	281.7	ZrO_2	65.21	530.5
	ZrO_2	24.52	182.5 (3d5/2) 184.5 (3d3/2)	C	21.91	284.6	O_{ads}	34.79	532

The quantitative estimation of elemental concentration is carried out by de-convolution of XPS spectra and the results of those are tabulated in Table 4.2. The intensity ratio of Zr 3d doublet of 3:2 is kept fixed for each chemical state. The results of elemental concentration are shown in Figure 4.10.

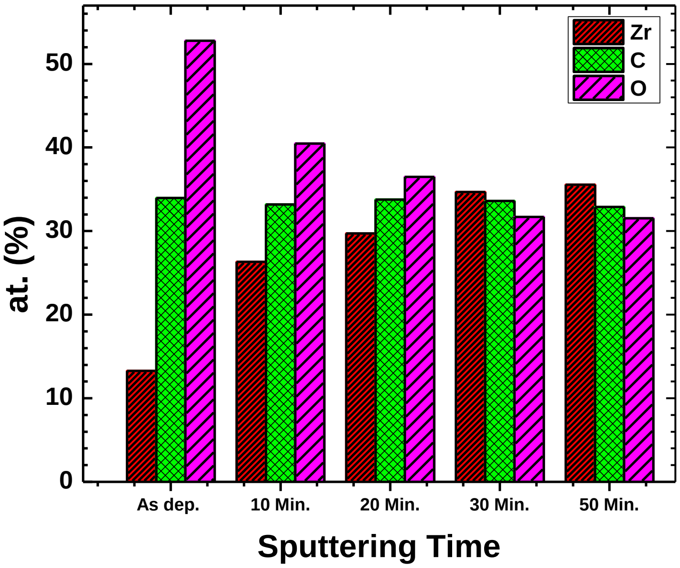

Figure 4.10: Concentration of elements from a ZrC thin film (**1-** as deposited, **2-** sputter etched for 10 minutes, **3-** sputter etched for 20 minutes, **4-** sputter etched for 30 minutes and **5-** sputter etched for 50 minutes).

The XPS analysis suggests that the top layer is strongly contaminated and is composed of a mixture of ZrC and ZrO_2 (ZrO_2 as dominating component). The major contaminants on the top surface are oxygen and carbon, which are partially coming from deposition conditions (relative high value of base pressure, residual gases in the deposition chamber's wall etc.) and sample handling. After sputter removal of near surface layers (10 minutes etching) an increase in Zr content (from 13.4 to 26.3%) with a simultaneous reduction in O concentration (from 56 to 37.3%) is observed, while carbon concentration remains same across the depth. It is important to note that the atomic percentage of Zr, C and oxygen are significantly different from those existing on the film surface. A large decrease in ZrO_2 phase (37.8% from 84.2%) is observed after subsequent sputter etching (20, 30 and 50 minutes). Zr 3d peak shifts towards ZrC phase with simultaneous decrease in oxygen concentration. However the overall presence of elemental oxygen remained significantly high (~30 at.%). The presence of oxygen can be accounted mainly to the diffusion of oxygen through the voids and pores existing in the film structure and partially from the experimental chamber[102]. The XPS analysis suggests that the film comprised of ZrC as dominating phase with significant amount of carbon and oxygen contaminants. This presence of unreacted carbon on the surface along with small amount of oxygen in the depth may be responsible for deviation in optical constants value, which in turn affects the reflectivity performance.

The surface morphology of thin films is characterized by rms roughness. RMS roughness is also a function of spatial frequency. AFM images taken over different length scales are combined to generate a single PSD in large spatial frequency range. Figure 4.11 shows the noise free smooth PSD functions of ZrC thin films. From the PSD analysis the rms roughness value is calculated and found less than 3 -6 Å, which is in good agreement with the roughness value obtained from XRR data.

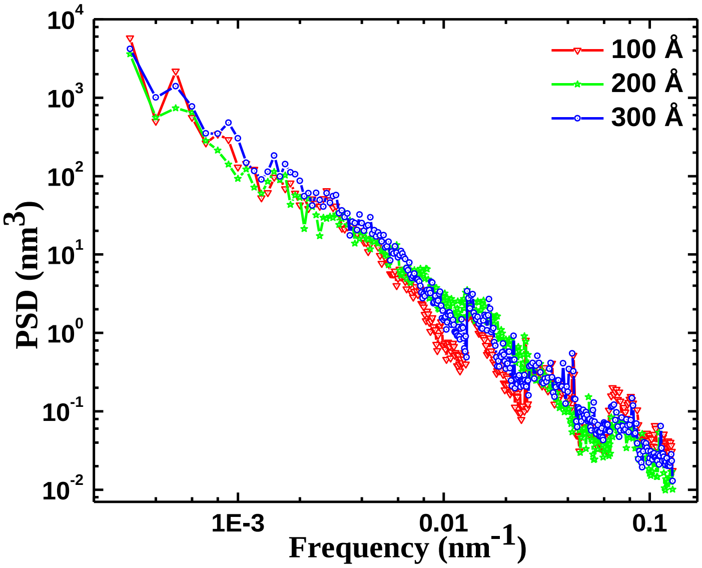

Figure 4.11: PSD of the ZrC thin films of different thickness. The average PSD function was obtained by averaging several PSDs calculated on several line profiles from topographic data.

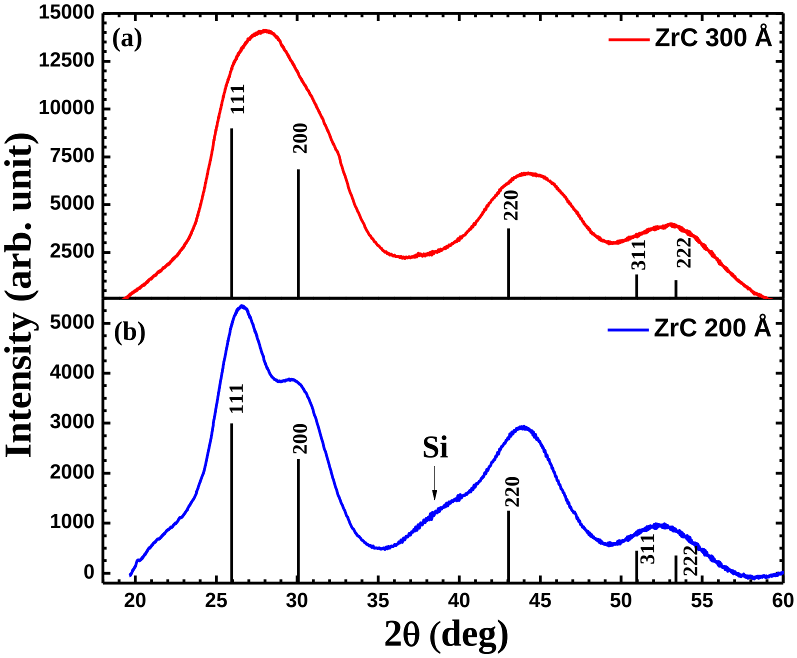

Figure 4.12: GIXRD pattern acquired from ZrC thin films of different thickness. The vertical lines correspond to calculated data from JCPDS for standard ZrC powder.

Further to investigate the crystalline state of ZrC thin films, GIXRD measurements are carried out. Figure 4.12 shows the GIXRD curves of ZrC thin films. Vertical black lines in the figure represent the position and intensity of XRD peaks corresponding to ZrC powder reported in JCPDS data base (74-1221). The 2θ values of JCPDS data have been modified for experimental wavelength and matches well with observed peak positions. In GIXRD curve **b)** a hump is seen which is because of Si substrate (as marked in figure). Si feature was more prominent in 100Å sample and ZrC pattern was not discernible. GIXRD data suggests that ZrC films are polycrystalline.

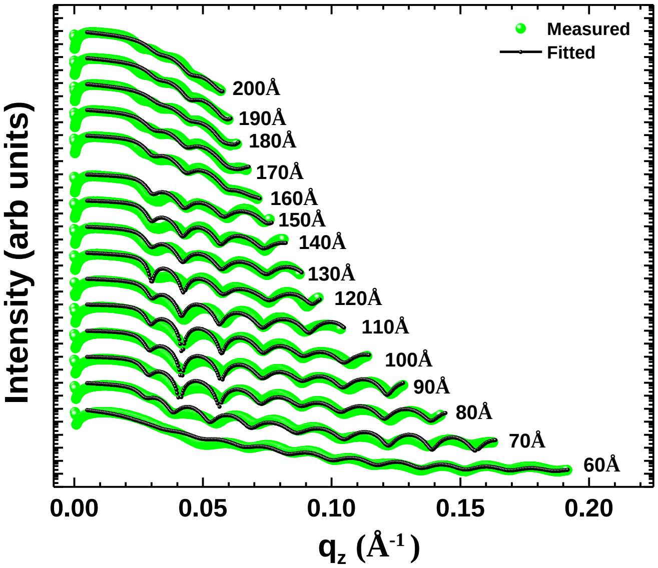

Figure 4.13: Measured and fitted angle dependent soft x-ray reflectivity measured in 60Å to 200Å wavelength region. Reflectivity data are fitted with same model used in GIXRR data analysis. Curves are vertically shifted for the sake of clarity.

After characterizing the structural properties of 300 Å thick ZrC film it is used for the determination of optical constants in 60-200 Å wavelength region. Measured and fitted SXR curves in 60-200Å wavelength region in 10Å step are shown in Figure 4.13 along with the best fit curves. Near the Zr M4 edge region, the reflectivity measurements are carried out in 2 Å step, the results are shown in Figure 4.14.

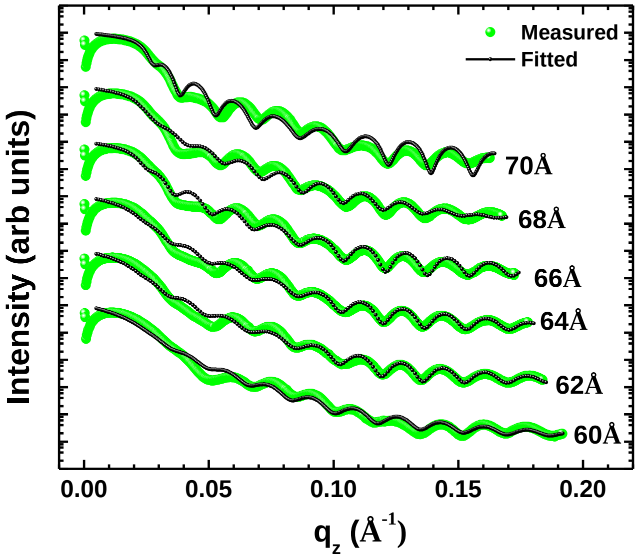

Figure 4.14: Measured and fitted soft x-ray reflectivity data at λ=62, 64, 66, 68 and 70 Å (Zr M4 edge). Data are fitted with same model used in GIXRR data analysis. Curves are vertically shifted for the sake of clarity.

Three layer model (1-oxide layer, 2-principal ZrC layer and 3- surface/contamination layer) is used to fit the SXR data. To obtain reliable values of optical constants and to reduce the number of fit parameters, thickness and roughness values as obtained from XRR analysis are kept fixed. As discussed in the last chapter, the accuracy of optical constants measured from x-ray reflectivity technique depends on β/δ ratio. If β/δ<<1, critical angle θ_c can be calculated from the $\theta_c=\sqrt{2\delta}$ relation, because the reflectivity pattern has a well-defined shoulder. For β/δ approaching to one, the reflectivity pattern becomes exponential like. Further if the ratio is greater than one (β/δ>1) the critical angle region in reflectivity pattern is not distinguishable and it is not possible to determine δ and β uniquely. So for the region with β/δ>1, the uncertainty in determination of δ and β is very high.

The experimentally measured optical constants for ZrC are listed in Table 4.3 are same are plotted in Figure 4.15 along with the tabulated values obtained from Henke's database obtained from CXRO website. The error in last significant digit determined from the least square refinement procedure is mentioned in the parenthesis in the Table 4.3. It is obvious that, the β/δ ratio in whole wavelength region is less than one suggesting that uncertainty in determination of δ and β is minimum. At higher wavelengths (70-200Å) measured δ values are found lower than the tabulated bulk values. The deviation in δ values is around 15 to 35%. Below 70Å (near Zr M4 edge) region the measured δ values show a deviation of around 2 to 20 %. In case of β a large deviation of 24-50% is found in 60-70Å wavelength region. Above 70Å wavelength the β values are in close agreement with Henke's tabulated values with deviation of ±10%. It is interesting that the delta values are showing a large deviation from Henke's tabulated data whereas the beta values are in close agreement.

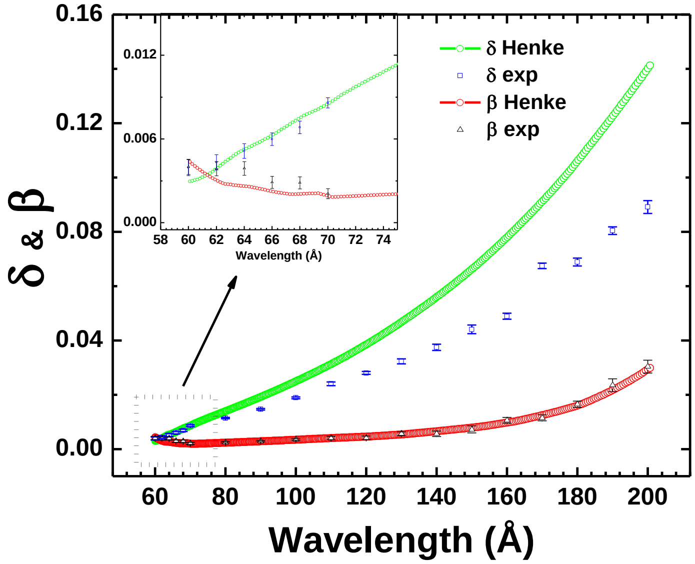

Figure 4.15: Measured optical constants of ZrC shown as discrete points, along with the error bars. Solid curves correspond to Henke's database for comparison. In inset optical constants near Zr M4 edge are shown. Measured and Henke's data are in close agreement.

This could be understood from the analysis of atomic scattering factor for Zr and C separately. Figure 4.16 shows real and imaginary part of atomic scattering factor (from CXRO website) f_1 and f_2 for Zr and carbon in soft x-ray region. Figure 4.16 suggest that f_2 values of Zr and C are very close in the wavelength range of 50-200Å, whereas the f_1 values of these two elements are significantly different. This suggest that the change in Zr:C ratio from 1:1 at near surface will not affect the beta value much but it will change the delta value significantly. In our case the lower delta value in higher wavelength range indicates that the ZrC film do not have 1:1 ratio of Zr and C specially in near surface region, which is also confirmed by XPS as discussed in section 4.2.3.

Table 4.3: Derived optical constants of ZrC in the 60-200 Å wavelength region, along with Henke's tabulated values

Energy (eV)	Wavelength (Å)	δ (Henke)	δ (Exp)[£]	β (Henke)	β (Exp)[£]
206.63	60	0.00398	0.0048(6)	0.00444	0.0045(6)
199.96	62	0.00429	0.0043(5)	0.00305	0.0038(5)
193.71	64	0.00523	0.0051(5)	0.00261	0.0039(5)
187.84	66	0.00625	0.0062(5)	0.00225	0.0029(4)
182.32	68	0.00749	0.0068(4)	0.00205	0.0028(4)
177.11	70	0.00851	0.0086(4)	0.00192	0.0021(4)
154.97	80	0.01387	0.0114(3)	0.00230	0.0024(2)
137.75	90	0.01912	0.0146(3)	0.00281	0.0029(3)
123.98	100	0.02486	0.0188(3)	0.00338	0.0035(3)
112.70	110	0.03120	0.0239(7)	0.00399	0.0040(6)
103.31	120	0.03842	0.0280(6)	0.00453	0.0041(6)
95.36	130	0.04668	0.0322(9)	0.00532	0.0056(7)
88.55	140	0.05588	0.037(1)	0.00650	0.005(1)
82.65	150	0.06613	0.044(2)	0.00785	0.007(1)
77.48	160	0.07789	0.048(1)	0.00965	0.010(1)
72.92	170	0.09108	0.067(1)	0.01240	0.011(1)
68.87	180	0.10594	0.068(1)	0.01591	0.016(1)
65.25	190	0.12244	0.080(2)	0.02165	0.023(2)
61.99	200	0.14004	0.089(2)	0.02926	0.030(2)

[£] For the experimental δ and β values the uncertainties in last significant digit are given in parentheses.

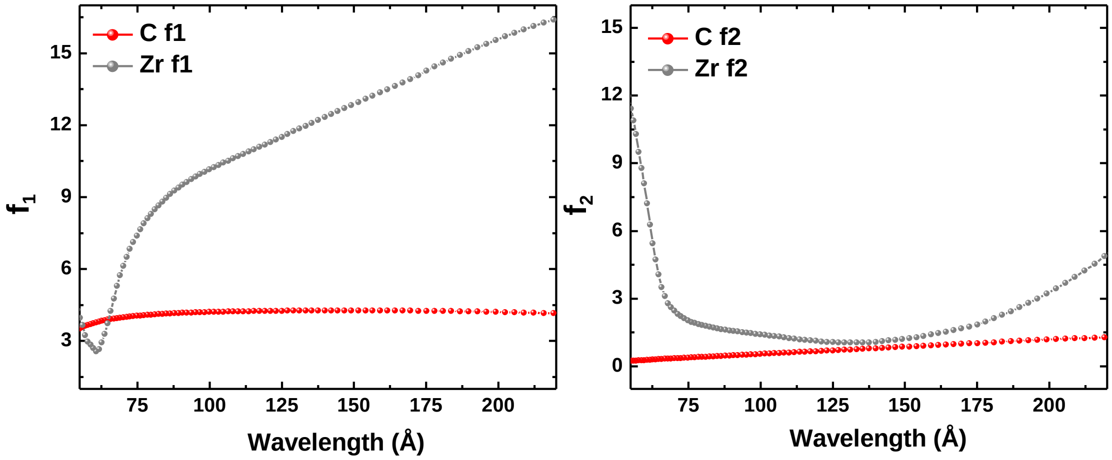

Figure 4.16: f_1 and f_2 for Zr and C in soft x-ray wavelength region of 40 – 160 Å.

Further Figure 4.17 shows the penetration depth of ZrC for 40-160 Å wavelength region at 15° incidence angle. The curve for penetration depth suggest that the photons of >120Å wavelength penetrates up to ~40Å in ZrC. In this situation, the surface region will predominantly affect the optical constant behavior of ion beam deposited ZrC. Because of growth process and reaction with ambient the surface of ZrC thin film could have a large deviation in Zr:C ratio and leading to reduction the δ value with nominal change in β value.

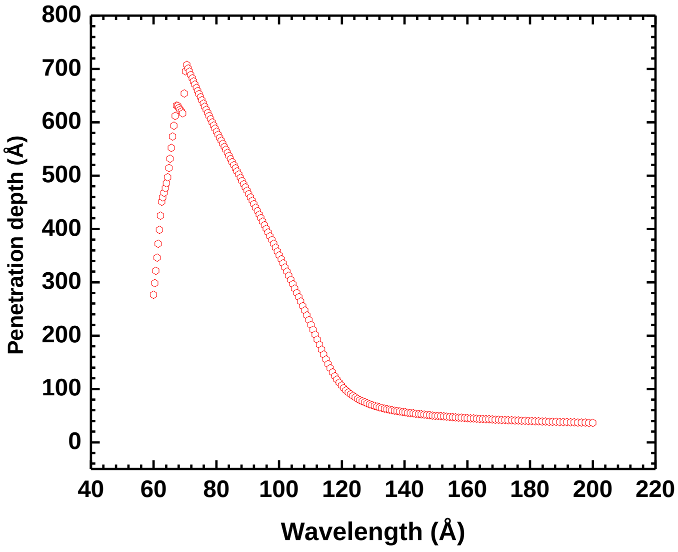

Figure 4.17: Penetration depth of ZrC in 40 to 160 Å wavelength region at 15 degree incidence angle.

The present study suggests that ZrC is an important optical material for soft x-ray multilayer application and may be used for more stable and reflective coating for multilayer system. It is essential to study the structural and optical properties of ZrC prior using it in multilayer system.

4.4. Conclusions:

ZrC is found to be suitable candidate for the fabrication of soft x-ray multilayer for high reflectivity performance near Al edge. Structural and optical properties ZrC thin films are studied for x-ray multilayer application. Following are the main inferences of the aforementioned study.

- ✓ Significant mismatch of 9 – 30 % in measured and theoretically calculated SXR vs wavelength data are found.

- ✓ High density and low roughness ZrC thin films are deposited, which is an advantage for making x-ray multilayers. Near bulk density (97% to bulk density) ZrC films are deposited. RMS surface roughness for all the thin films is found to be in 3-6 Å range, which suggests smooth surface morphology of ZrC thin films.

- ✓ XPS measurements performed after sequential etching suggests that some amount of adventitious carbon and oxygen is present in the depth.

- ✓ Optical constants of ZrC in 60-200 Å wavelength region are measured. The δ values are found 15-35 % less than Henke value while β values are found in close agreement to Henke's tabulated value.

Chapter 5.

Surface Contamination Effect on Optical Properties

Carbon contamination is a severe problem for optical elements used in SR beamlines and need to be removed periodically using appropriate cleaning technique. In this chapter, surface laser cleaning technique is used to remove the carbon layer from the gold surface without affecting the surface underneath. Cleaning quality is analyzed using several experimental techniques. Results obtained are described in detail.

5.1. Introduction:

The continuous spectrum of electromagnetic radiation emitted by electron storage rings in a synchrotrons radiation (SR) sources extend from extreme ultraviolet (EUV) to hard x-rays and currently are the main sources of radiation for the experiments on material characterization, biomedical imaging, and absorption measurements etc.. In these sources, several optical elements (such as mirrors, gratings, zone plates etc.) in EUV spectrometers and SR beamlines are used. The carbon contamination on these optical elements is a major problem[33,103].The carbon containing molecules (such as oil vapours from the machining process, vacuum pump oil vapours etc.) adsorb on the optical surface and crack. This cracking process occurs either directly by x-rays or by the free electrons at the optical surface created by x-rays. After cracking, the carbon atoms stay on the surface with stronger bonding with the surface. Carbon contamination causes poor signal-to-noise ratio, which makes it difficult to perform the experiments near carbon K edge energy range[104]. Even a 10 Å thick carbon layer reduces the relative reflectivity of a single reflecting layer of optical surface by 1.4%[47]. As example Figure 5.1 shows the calculated reflectivity of gold mirror in 10-60 Å wavelength region at 5º incident angle. In the same figure, reflectivity of gold mirror with a carbon layer of 10 Å and 100 Å thicknesses is shown. It is clear that a carbon layer of 10 Å significantly affects the reflectivity performance of the gold film. Further as carbon layer thickness is increased to 100 Å, the reflectivity drops down significantly. This reduction is because of the high absorption of EUV radiation in carbon, which makes the contamination layer as a serious source of loss of throughput. Extreme ultraviolet lithography (EUVL) scanner optics typically consists of ten such reflecting layers, where total throughput deteriorates drastically. As a remedy, the optical elements need to be replaced[48]. Since soft x-ray/EUV optical elements are very costly, hence dispose of the damaged optical elements is not a viable solution. Hence it is desirable to develop a technique for periodic removal of the carbon contamination without damage or modifications to the underneath gold film/surface[49,50,51].

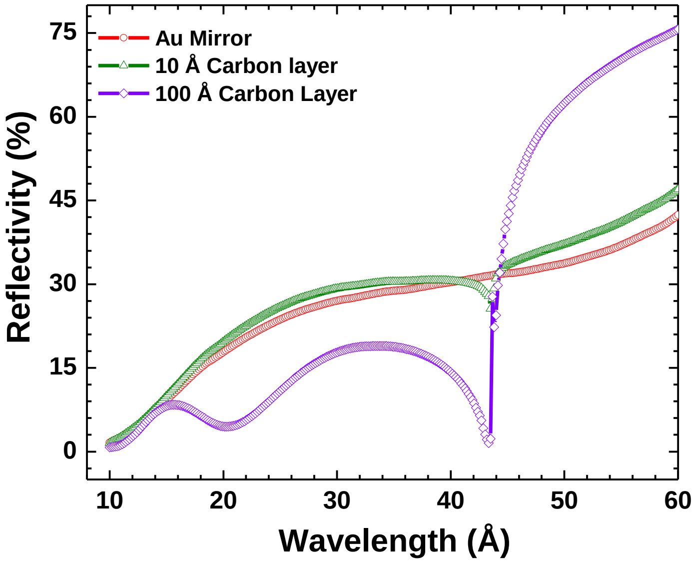

Figure 5.1: Calculated reflectivity of Au mirror is shown in 10-60 Å (near carbon edge) at 5 degree incident angle. Effect of carbon layer on top of gold mirror is shown. It is clear that a 10 Å carbon layer significantly affects the reflectivity performance of Au mirror. A 100 Å thick carbon layer reduces the reflectivity of the Au mirror.

In the past decade numerous efforts have been put for removal of the carbon contamination from the optical elements of SR beamlines using several conventional wet and dry cleaning techniques such as chemical cleaning, plasma cleaning, ultraviolet (UV) lamp cleaning in oxygen atmosphere[105], DC discharge cleaning[106], RF discharge cleaning[107], laser shockwave cleaning[108], etc. The Hg UV lamp cleaning in activated oxygen atmosphere is used for cleaning of the mirror in TEMPO beamline at SOLEIL synchrotron, France where the roughness and reflectivity was recovered after cleaning of the contaminated mirror. The UV/ozone cleaning technique is also used successfully for cleaning of replica gratings. The UV/ozone cleaning reversed the degradation of figure error caused by the carbon build up, and restored the reflectivity[109]. This technique is also used in Elletra synchrotron source, Italy for cleaning of the optics in the soft x-ray monochromator. These conventional cleaning methods have their own limitations, such as in chemical cleaning method, the chemical agents are used to clean any size samples, but the surface topology of the optical elements may change due to re-deposition of impurities from the chemical solution. In case of DC/RF discharge cleaning[106,107], there are several parameters to be optimized such as type of gas, pressure of gas, electrode power, cleaning time, etc., which makes the use of these techniques difficult for cleaning with good surface quality. In the case of laser shockwave cleaning[108], a shockwave is used for the carbon layer removal from the optical surfaces. For the generation of the shockwave an ultra-short laser pulse is focused in air to form plasma resulting in the shockwave. In this technique, distance between laser focus and optical surface is a crucial parameter. If the distance is less than the optimized distance, the plasma plume may damage the optical surface and if the distance is larger than optimized distance, the amplitude of shockwave may not be sufficient for smooth cleaning of optical elements, and hence topology of the surface may change.

Several scientists and engineers are facing carbon contamination problem on synchrotron optics. Recently (16th-17th July 2012) a satellite workshop "*Carbon contamination of optics: causes, characterisation and in-situ treatments*"[110] was held at synchrotron SOLEIL, St Aubin (France). Several experimental works related to carbon contamination on storage ring, beamline optics, lasers, space optics etc. are presented and published. Pecault et al. has reported reduction in optics lifetime due to organic contamination[111,112]. Raabe et al. have reported carbon contamination at PoLux and Nano-XAS beamline at Swiss light source (SLS).

Dry laser cleaning technique has immense advantages in area of cleaning. In this technique, a laser beam is focused on a material which is to be cleaned. Absorption of laser beam in the material results in the ablation of the material resulting in smooth cleaning of the optical elements. Dry laser cleaning has several advantages over other conventional cleaning techniques, such as it is very fast, non-contact, dry in nature, highly localized, well controlled layer-by-layer removal of material, less parameters to be optimized, fibre optic beam delivery option for in-line cleaning of components and most important no significant change in the surface quality and roughness of the film surface/substrate after cleaning[113,114,115,116].

The most important parameter for laser cleaning process is fluence (F), defined as energy per unit area. Laser cleaning process is a selective thermal ablation process, and it starts above a minimum fluence, called ablation threshold fluence. Thus the laser fluence should be high enough to ablate the layers, but it should be low enough to ensure that the underneath surface/ substrate is not damaged. The temperature rise ΔT in one dimensional heat conduction in semi-infinite solid model is given by[60]:

$$\Delta T = \frac{AF\alpha}{C_p \rho l_d} = \frac{AI\alpha t_p}{C_p \rho l_d} \quad \textbf{5.1}$$

where, A is the Hamaker's constants, F is the laser fluence, I is the laser intensity, α is the absorption of the laser in the material, C_p is the specific heat, l_d is the heat diffusion length. The heat diffusion length is defined as:

$$l_d = \sqrt{4kt_p} \quad \textbf{5.2}$$

where k is the thermal diffusivity of the material and t_p is the laser pulse duration. The time required for coating material to reach the vaporization temperature can be calculated by:

$$T_s(t) - T_0 = \left(\frac{2\alpha I}{K} \sqrt{kt/\pi} \right) \quad \textbf{5.3}$$

where T_s is the temperature of the coating material and K is the thermal conductivity of the material. The cleaning efficiency in a single scan is defined as:

$$\eta = 1 - \frac{N_f}{N_i} \tag{5.4}$$

Here N_f and N_i are the respective surface densities of the coating material before and after laser cleaning. The maximum cleaning efficiency in N laser scans is defined as:

$$\eta_{\max} = 1 - (1 - \eta)^N \tag{5.5}$$

Further the evaporation rate R_{evap} and ablation depth d can be defined as:

$$R_{evap} \cong \frac{I_\alpha}{\varepsilon_b} \tag{5.6}$$

$$d = \frac{1}{\alpha_p}.\ln\left(\frac{F}{F_{th}}\right) \tag{5.7}$$

where ε_b is the binding energy and α_p is the penetration depth of the laser. Linear cleaning speed v for $P\%$ spot overlapping is defined as:

$$v = \left(1 - \frac{P}{100}\right)(S \times R) \tag{5.8}$$

where R is the pulse repetition rate, S is the focus spot diameter. All these parameters are optimized for the carbon cleaning experiments.

In the present work a nanosecond pulsed Nd:YAG laser is used to remove e-beam deposited carbon layer from the Au surface. It is found that the carbon layer can be removed using nanosecond duration laser pulses at high repetition rate of 1-2 kHz. X-ray photoelectron spectroscopy (XPS), soft x-ray reflectivity (SXR), Raman spectroscopy and x-ray absorption spectroscopy (XAS) techniques have been used to analyze the Au surface before and after the laser cleaning. Atomic force microscopy (AFM) technique is used for topographic measurements. Power spectral density (PSD) function is calculated to analyze surface imperfection over wide frequency range.

5.2. Experimental:

5.2.1. Sample Preparation:

For the laser cleaning experiments gold film of ~200 nm thickness is deposited on 50 mm×30 mm size BK7 glass substrate. A 20 nm thick carbon layer is deposited on two third portion of the gold coated sample using electron beam evaporation technique. One third portion of the sample is kept intact for comparison after the laser cleaning experiments. Schematic diagram of the sample is shown in Figure 5.2, where region A, B, and C denotes the intact gold film (marked as A), carbon coated gold film (marked as B) and area used for laser cleaning (marked as C).

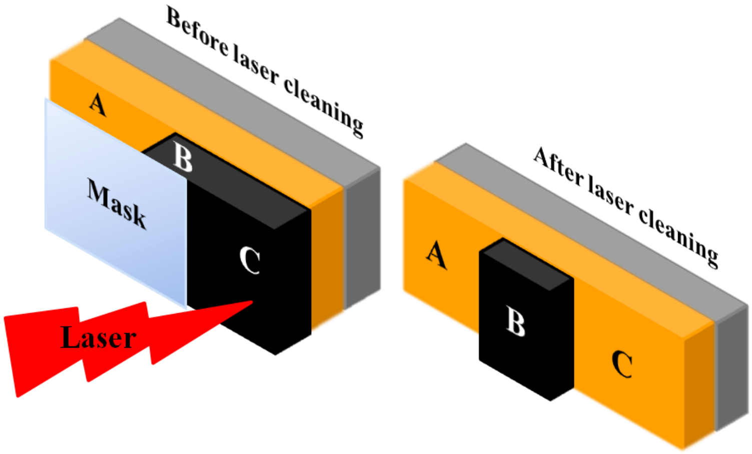

Figure 5.2: Schematic diagram of the sample used for laser cleaning experiments (A) intact gold film, (B) carbon coated gold film, (C) carbon removed gold film after laser treatment.

The two areas A and B are kept under the mask during the laser cleaning experiments. Region-C is used for the laser beam exposure to remove the carbon layer. Actual photo-graph of the sample before and after the laser cleaning is shown in Figure 5.3.

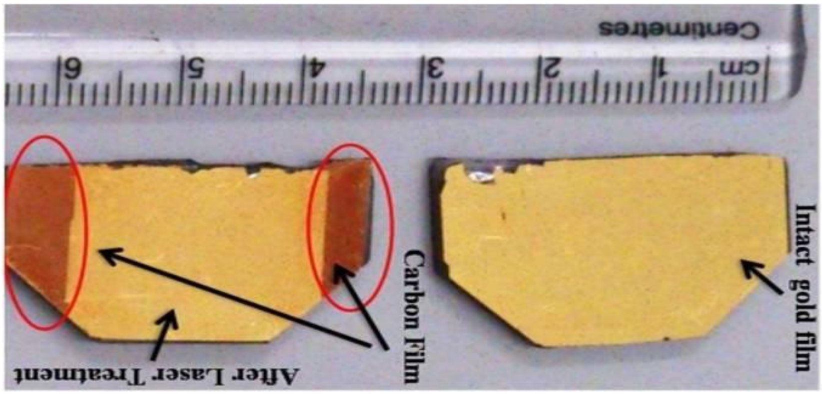

Figure 5.3: Photograph of the intact gold film, carbon coated gold film, and the area on the sample where the carbon film is removed and underneath gold film is visible.

5.2.2. Laser Cleaning Setup:

A lamp pumped acousto-optic Q-switched Nd:YAG laser system, with 100 ns pulse duration, 10 mJ of pulse energy is used for laser cleaning process. Schematic diagram of laser cleaning setup is shown in Figure 5.4.

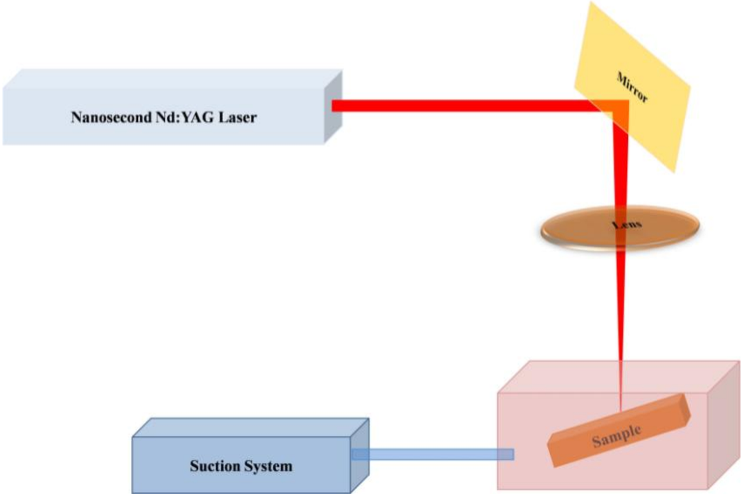

Figure 5.4: Schematic layout for laser cleaning setup for carbon removal.

Experimental parameters of laser cleaning setup are given in Table 5.1. In this setup an orthogonal pair of galvanometer scanners is located at a suitable distance from the target.

Galvanometer scanners typically consist of a mirror mounted to an electric motor, with positional feedback arrangement. The scanner mirror can move the laser beam in the X-Y direction.

Table 5.1: Parameters of the Nd: YaG laser used for the cleaning experiments

Pumping method	Flash Lamp
Average output power	1-20 W
Pulse energy	1-10 mJ
Peak power	2-100 kW
Pulse duration	100-400 ns (FWHM)
Repetition rate	1-50 kHz
Linear scan speed	280 mm/s
Focus spot diameter	0.1-1.0 mm

The laser beam always remains at focus in the plane using a flat field lens. The flat field lens is used such that the laser beam strikes normal (perpendicular) to the sample. The typical laser spot diameter at the focal plane is ~ 500 µm. In the laser cleaning process the pulse energy is varied from 1mJ- 10mJ, angle of incidence from 10 degree to 45 degree, number of passes from 1 to 10 and percentage of spot overlapping from 60 % to 90 % for a fixed area of 48 mm^2. For different percentage of the laser spot overlapping a CAD drawing is generated and then the data is transferred to X-Y scanner. For the cleaning experiment sample holder is fixed on a linear stage to get the precise positioning of the sample. During the laser cleaning process the debris of the carbon layer is removed using a suction pump of 200 lpm capacity. Process parameters such as laser repetition rate, pulse duration, pulse energy, laser intensity, focused beam area for the carbon thin film are optimized in a similar fashion as reported by Gamaly and co-workers[117,118] and these optimized parameters have been used for the present carbon cleaning experiments using a Q-switched Nd:YAG laser.

5.2.3. Structural Characterization:

X-ray photoelectron spectroscopy (XPS) technique is used to determine the cleaning efficiency. XPS measurements are carried out using an Omicron EA-125 photo electron spectrometer working at a base pressure of ~6.7×10^{-8} Pa. Al source operated at 10 kV anode voltage and 10 mA emission current is used for x-ray emission. A concentric hemispherical analyzer of resolution 0.8 eV and pass energy 50 eV is used. XPS spectra have been de-convoluted using Gaussian de-convolution method.

It is known that Raman spectra are extremely sensitive to all form of carbon (graphite or diamond). Here we have investigated all three regions of sample using Raman spectroscopy. The Raman scattering is excited using the Ar laser at 488 nm and is analyzed using a Jobin-Yvon micro-Raman spectrometer (HR800) over the range 800–1800 cm^{-1}. Raman spectrum is de-convoluted with Lorentzian peaks.

5.2.4. Optical Characterization:

Soft x-ray reflectivity measurements are carried out at reflectivity beam line[57] Indus-1 synchrotron radiation source. The experimental station in the beamline is a high vacuum soft x-ray reflectometer. SXR measurements are carried out in 0 to 30 degree incidence angle at 70 Å incident wavelength. For the analysis the SXR data, the Parratt formalism[88] is used. The effect of surface roughness is taken into account using the Névot -Croce model[13]. A nonlinear least-square refinement routine based on the Genetic algorithm is used to refine the fitting parameters[89].

5.3. Results and Discussions:

Laser cleaning experiments are carried out to remove the carbon layer of 200 Å thickness from the gold surface. Several parameters such as laser pulses, angle of cleaning, spot overlapping and laser power are optimized for carbon cleaning. The optimized parameters of 30 degree angle of incidence, 60-90% spot overlapping, ns pulse laser and 2 mJ laser power is used for the laser cleaning experiments. Eggenstein et al. have reported cleaning of gratings and mirrors at BESSY II using plasma discharge process in 18 hours[104], which seems to be a very slow and time consuming process. In the present work an area of 48 mm^2 has been cleaned in 3 minutes, suggesting that laser cleaning technique is very fast. Cleaning quality are analyzed using several techniques and are discussed below. Since the XPS technique is highly surface sensitive and also highly sensitive to carbon, XPS measurements on three different regions of the sample marked as region A, B and C (see Figure 5.2) of the C1s core level are carried out and are shown in Figure 5.5. From Figure 5.5 (b), it is evident that the peak corresponding to C-*1s* binding energy has a significantly large width which indicated that different phases of carbon are present in the sample.

The XPS spectrum of the carbon coated gold film region (b) is fitted using Gaussian de-convolution method with two peaks, one with peak energy 284.7 eV and second having peak energy of 287.8 eV. Earlier Bratt et al. [119] have tabulated maximum possible carbon bonds/group with corresponding binding energy. This report suggests that the peak at 284.7 eV corresponds to C-C *sp2* hybridization and peak at 287.8 eV corresponds to C-O group. In the present analysis, the XPS spectrum of intact gold film is fitted considering C-C *sp2* hybridization peak (284.8 eV) and other with C-O group peak (287.6 eV).

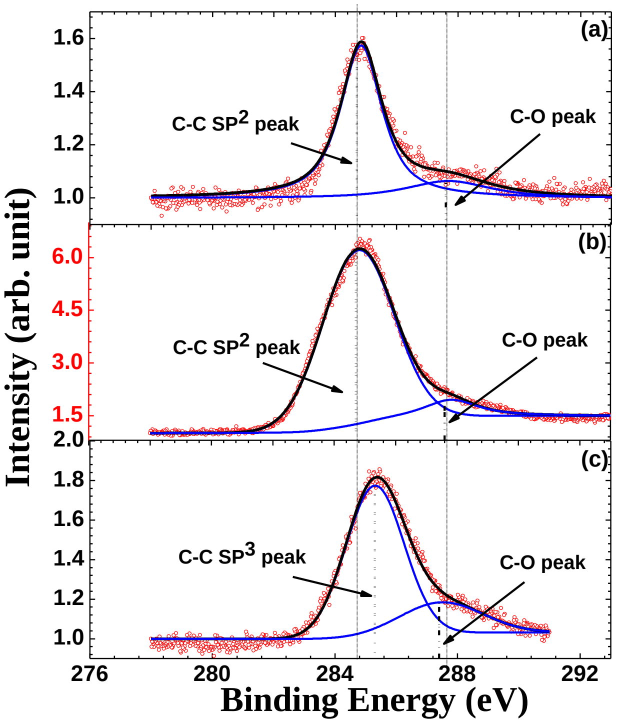

Figure 5.5: XPS measurements of the three regions of the sample **(a)** intact gold film **(b)** carbon coated gold film **(c)** the gold film after carbon removal with laser cleaning.

After the laser cleaning experiments, the carbon film is removed; however the presence of the carbon peak in the XPS spectra [Figure 5.5 (c)] seems to be originated from the residue carbon atoms/ atmospheric carbon. The position of the carbon peak of the laser cleaned region "C" is shifted with respect to the carbon peak of the intact gold film region 'A' and that of carbon coated gold film region 'B'. Carbon peak of laser cleaned region-C is fitted with two components, one with peak energy 285.3 eV, and second having peak energy 287.4 eV. The peak at 285.3 eV corresponds to C-C *sp3* hybridization (diamond like) and at 287.4 eV corresponds to C-O group[119]. Earlier Kononenko et al. have reported phase transition in amorphous carbon using optical laser pulses[120]. Gaudinet et al. [121] have reported amorphous to crystalline transition in carbon induced by femtosecond pulsed x-ray free electron laser. In the present case the presence of peak at 285.3 eV corresponding to C-C sp^3 bonding suggests that the residue carbon present on the sample surface after laser cleaning have undergone a phase transition induced by laser shots.

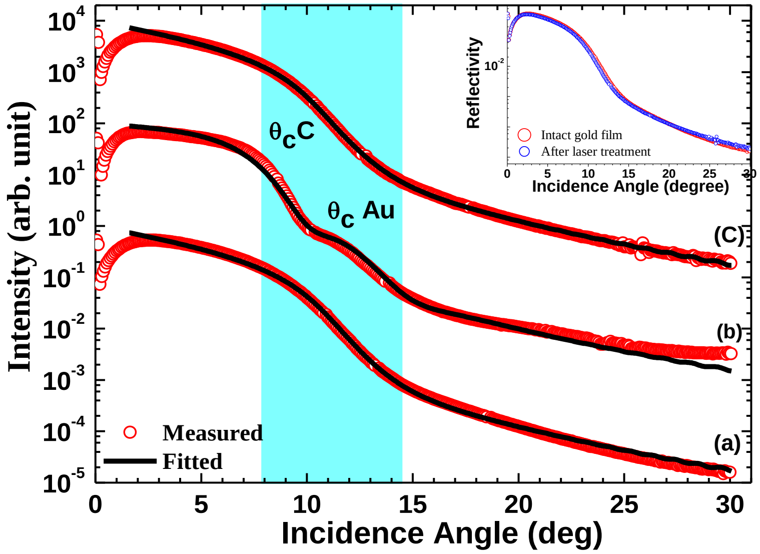

Figure 5.6: Measured and fitted SXR spectra of (a) intact gold film, (b) carbon coated gold film and (c) gold film after carbon removal are shown. Measurements were carried out using λ= 7 nm wavelength. Critical angle corresponding to total external reflection region are distinctly different of pure gold film and carbon coated gold film as shown in highlighted area in the figure. After carbon film removal with laser treatment the reflectivity curve of intact gold film and that of laser cleaned film are similar as shown in inset of the figure.

However the intensity of C peak of two areas- region-A (intact gold film) and region-C (laser treated area) are similar. This suggest that the atmospheric carbon on region-A and sp^3 phase on region-C are in similar amount. For further confirmation and quantitative study, SXR measurements are carried out using 70 Å incident wavelength for all three regions and results are shown in Figure 5.6.In SXR data, the carbon coated gold film and pure gold film gives distinctly different critical angles. The region-B of the sample (see Figure 5.6 (c)) which has a carbon coating of 20 nm on top of gold thick layer therefore give rise to two distinctly different critical angles at ~7.9 degree for carbon and at ~10.5 degree for gold.

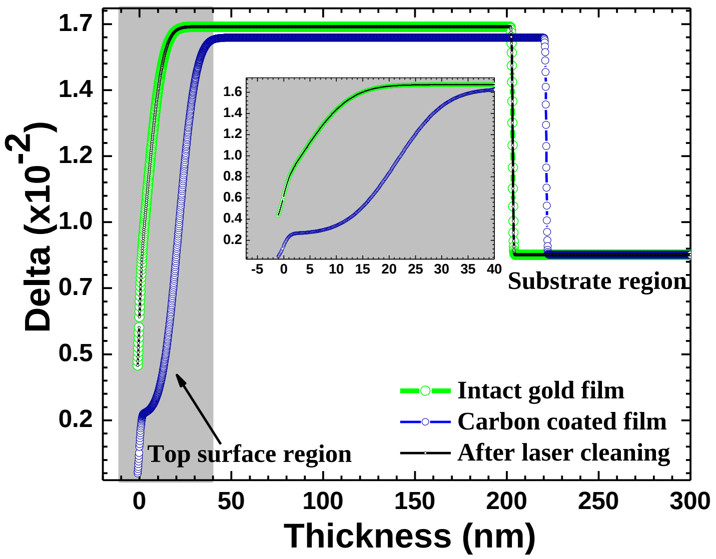

Figure 5.7: Optical density profile derived from SXR fit of measured data of intact gold film (region-A), carbon coated gold film (region-B) and carbon removed gold film (region-C). The profile of intact gold film (region-A) and that of laser cleaned gold film (region-C) are identical, whereas the profile of carbon coated gold film are markedly different as shown in the inset.

Similarly SXR data corresponding to region-A of the sample which is intact gold film shows a single critical angle corresponding to gold layer at 10.5 degree, shown in Figure 5.6 (a). Since the Nd:YAG laser cleaning is carried out on region-C hence this region should show a single critical angle corresponding to gold film if carbon layer is removed. Figure 5.6 (c) corresponding to region-C confirms that this region has a single critical angle corresponding to pure gold film. In the inset of Figure 5.6, measured reflectivity of intact gold film and laser cleaned gold film are shown, which are exactly same suggesting that the carbon film has been removed. The SXR data of region-A and region-C are analyzed using a three layer model on substrate. The model comprised of a native oxide layer on substrate, gold layer and top contamination layer. Further the SXR data corresponding to region-B is fitted with four layers, oxide layer, gold layer, carbon layer and top contamination layer. The parameters such as optical constants of the film obtained from detailed fitting from SXR data are found in close agreement with theoretical values. The optical density profiles obtained from the fit parameters are shown in Figure 5.7. In the inset of Figure 5.7, surface portion of the optical density profiles are zoomed. With the comparison of fitted optical density profile of intact gold film (green curve in Figure 5.7) with the laser treated region (black curve in Figure 5.7), it is clear that surface quality of the gold film before and after laser cleaning are the same, which is very important particularly in case of synchrotron optics.

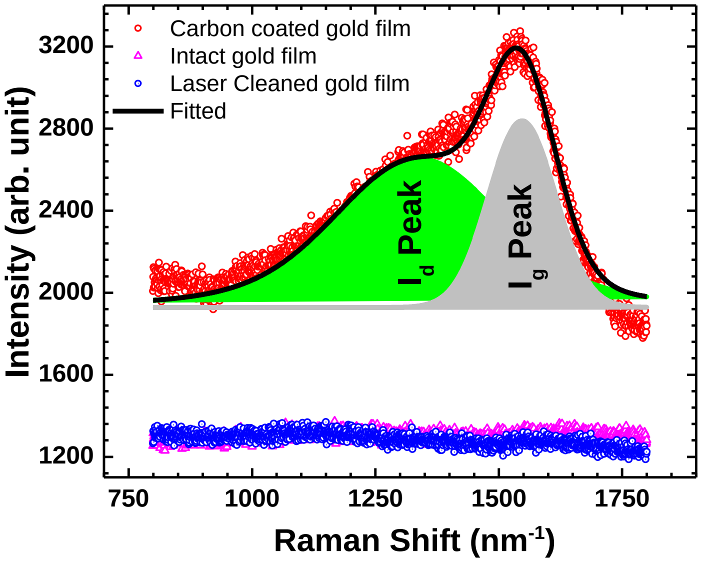

Figure 5.8: Raman spectrum of three regions of the sample is shown for (region-A) intact gold film, (region-B) carbon coated gold film and (region-C) gold film after carbon removal with laser cleaning.

Further to investigate the cleaning quality, we performed Raman measurement, as Raman spectroscopy technique is very sensitive to all phase of carbon[122]. Figure 5.8 shows the Raman spectra of three regions of the sample as shown in Figure 5.2. Raman curve for region-B is de-convoluted with two lorentzian peaks. One peak with Raman shift 1547.1 nm^{-1} corresponds to graphite phase (I_g peak) of carbon and the second peak with Raman shift 1335 nm^{-1} corresponds to disorder (I_d peak). Further no peaks are obtained in the Raman spectrum of region-A (intact gold film) and the region-C (laser cleaned gold film), suggesting that the carbon film has been removed completely.

Surface roughness is a very important parameter in case of the optical elements. The surface morphology of thin films is characterized by rms roughness. RMS roughness is also a function of spatial frequency. Several techniques like (XRR, AFM etc.) are used to study the surface roughness in various spatial frequency regions. In present case, to check the surface morphology of gold films, AFM measurements are carried out over different length scales and resultant topographic data are combined to generate a single PSD.

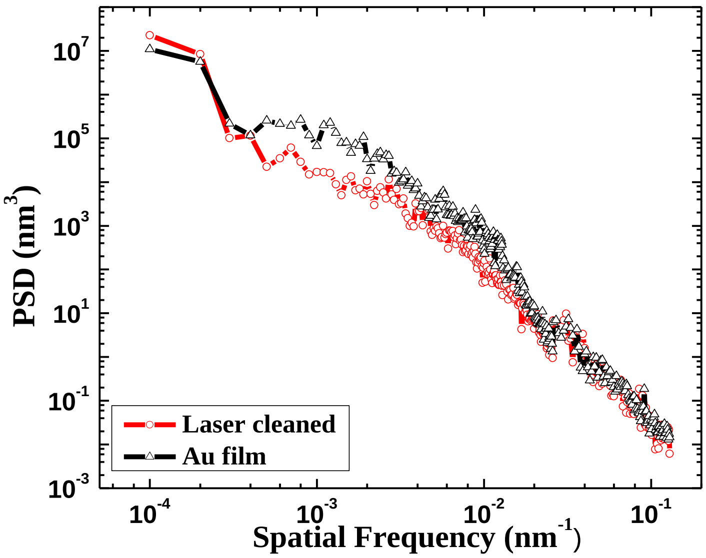

Figure 5.9: PSD of the gold film before and after laser cleaning. The average PSD function was obtained by averaging several PSDs calculated on several line profiles from topographic data.

Figure 5.9 shows the noise free smooth PSD functions of gold film over spatial frequency bandwidth of 10^{-1} to 10^{-4} nm^{-1} before and after laser cleaning. The PSD values of intact gold film are high suggesting higher surface roughness. From the PSD analysis the rms roughness of intact gold film is found 3.76 nm, which is improved to 1.54 nm after laser cleaning. It is evident from Figure 5.9 that the laser cleaning process modifies the PSD in mid frequency range of 4×10^{-4} to 10^{-2} nm^{-1} whereas it remains similar above 10^{-2} nm^{-1} range. PSD analysis suggests that the laser cleaning technique improves the surface morphology of the gold film. Earlier, several reports are published about cleaning of carbon layer using other techniques, but they have reported some change in surface roughness of the film[123,124]. The present study finds an improvement in surface roughness after laser cleaning process indicating that the technique is superior not only for carbon removal but also heals the surface roughness.

5.4. Conclusions:

Carbon contamination significantly affects the performance of the optical elements used in SR beamlines. A cleaning technique is therefore required for the periodic removal of carbon contamination. Laser cleaning technique is deployed for the first time for removal of carbon contamination from gold film. Following are the main inferences of the aforementioned study.

- ✓ A 200 Å thick carbon layer is removed completely from the gold surface using ns pulsed Nd: YAG laser.
- ✓ Cleaning quality is determined using XPS, Raman and SXR techniques and it is found that ns pulsed Nd:YAG laser is highly effective in the removal of carbon layer.
- ✓ The laser cleaning technique is found very fast compared to other conventional cleaning techniques.
- ✓ Surface morphology is analyzed using SXR and AFM techniques and it is found that laser treatment does not affect the surface quality of gold film, which is very important for optical elements.

Chapter 6.

Summary and Future Scope

In this chapter, the main findings of the present thesis work are summarized along with the scope of the future work.

6.1. Summary and Conclusions:

Compound materials (NbC and ZrC) have shown stable and enhanced optical performances in soft x-ray energy region. The expected performance from compound materials is difficult to achieve because of growth related changes in structural and chemical properties. Further the optical constants of compound materials are distinctly different from the Henke et al tabulated values and need to be determined. In present thesis work a detailed structural and optical studies on thin films of NbC and ZrC compound materials are carried out. In addition a laser based cleaning technique is deployed for the removal of surface contamination (carbon and gold layer) from optics surface.

Structural studies:

In the present thesis work two compound materials NbC and ZrC are investigated for their use in x-ray optical elements. A discrepancy in soft x-ray reflectivity performance of NbC and ZrC films are observed, which could not be explained with Henke's tabulated data. To understand the deviation, a detailed structural and chemical investigation of NbC and ZrC films of different thicknesses are carried out. Structural parameters (thickness, roughness and film density) have been determined from XRR technique. Density of the NbC films is found to be increasing from 6.13 g/cm^3 to 7.11 g/cm^3 with increase in film thickness from 100 Å to 500 Å (bulk density is 7.82 g/cm^3), while the density of ZrC films is found to be 6.49 g/cm^3, which 97% of the bulk density (6.73 g/cm^3) for all the thicknesses (100 Å to 300 Å). The less density in NbC film is because of Nb vacancy (low Nb-Nb coordination) as explained from the detail analysis of the EXAFS data. The surface roughness of the NbC and ZrC films are found to be in 3-6 Å range from XRR and AFM data. The chemical stoichiometry as a function of depth is explored using XPS technique. Analysis of XPS results after various sputtering cycles suggests that some amount of unreacted carbon and oxygen is present in the depth of the NbC film, while in ZrC films the unreacted carbon near the surface with small amount of oxygen throughout the film thickness is found.

In conclusion, Nb vacancy and presence of unreacted carbon is found to be responsible for variation in optical constants that in turn lowers the reflectivity performance of thin film in soft x-ray region. Our present study suggests that the NbC is a suitable material for soft x-ray optical applications near Si L-edge, while ZrC may turn out to be a suitable candidate for the fabrication of soft x-ray multilayer for high reflectivity performance near Al L-edge region.

Optical Studies:

Optical constants of NbC in 60-150 Å wavelength region are measured while the optical constants of ZrC are measured in 60-200 Å wavelength region and are compared with the tabulated Henke values. The values of δ and β for NbC are found to be lower (5 to 38 %) than the bulk value, while the δ and β values for are found to be 15-35 % less than the data obtained from Henke's tabulated values. This deviation in optical constants in soft x-ray region is due to the change in chemical composition of NbC and ZrC.

Surface Contamination Studies:

A lamp pumped acousto-optic Q-switched Nd:YAG laser system, with 100 ns pulse duration and 10 mJ of pulse energy is used for laser cleaning process. After several process optimization a 200 Å carbon layer is successfully removed from the gold surface. Further a gold layer of 480 Å is removed from the SiO_2 substrate. X-ray reflectivity, Raman spectroscopy results obtained from gold mirror before and after laser cleaning of carbon layer suggest that the carbon layer has been removed. Surface quality is analyzed after laser cleaning using SXR and

PSD analysis and it has been found that the laser cleaned surface has significant improvement compared to the actual mirror surface.

6.2. Scope of the Future Work:

X-ray multilayers are widely used as optical elements in the 3rd generation synchrotron radiation sources. Compound multilayers are found thermally stable compared to elemental multilayers. In India, two synchrotron radiation sources Indus-1 and Indus-2 of energy 0.45 GeV and 2.5 GeV respectively are operational. In several beamlines of Indus-1 and Indus-2 elemental multilayers are used, where thermal stability is a serious issue. Since compound multilayers are found thermally more stable, it is appropriate to investigate the detailed behavior of compound multilayers particularly carbide based multilayers (NbC/Si, ZrC/Al, ZrC/Mg etc.), which are highly stable and form smooth surface with the spacer material. A further study is required on fabrication of ZrC/Al multilayer and to analyze the interface diffusion with layer thickness, which could not be performed in the present thesis.

Further the effect of temperature and ion irradiation on the optical behavior of compound materials in the soft x-ray energy region need to be investigated, because optical constants are sensitive parameters and may introduce error in design of a multilayer if not known accurately.

Further the laser cleaning setup need to be installed at Indus-1 synchrotron radiation source for in situ cleaning of carbon contamination. Study on the effect of laser pulse on materials is required.

Bibliography:

[1] D. Attwood, “Soft X-Rays and Extreme Ultraviolet Radiation” Cambridge University Press, Cambridge, UK, (1999).

[2] R Soufli Ph.D. Thesis “Optical Constants of Materials in the EUV/Soft X-Ray Region for Multilayer Mirror Applications” Submitted to Ernest Berkeley Orlando Lawrence National Laboratory 1997.

[3] M. Kühne and P. Müller, “Higher order contributions in the synchrotron radiation spectrum of a toroidal grating monochromator determined by the use of a transmission grating” Rev. Sci. Instrum. **60**, 2101 (1989).

[4] R. L. Cavasso Filho, M. G. P. Homem, R. Landers, A. Naves de Brito, “Advances on the Brazilian toroidal grating monochromator (TGM) beamline” J. Electron Spectrosc. Relat. Phenom. **144-147**, 1125 (2005).

[5] J. H. Underwood, “X-ray optics” American Scientist **66**, 476 (1978).

[6] J. H. Underwood and T. W. Barbee, Jr., “Layered synthetic microstructures as Bragg diffractors for x-rays and extreme ultraviolet: theory and predicted performance,” Appl. Opt. **20**, 3027 (1981).

[7] R. Loudon, “The Quantum Theory of Light” Oxford University Press, London, UK, 2nd edition, (1983).

[8] J. D. Jackson, “Classical Electrodynamics” Wiley, New York NY, USA, 3rd edition, (1998).

[9] R.W. James, “The Optical Principles of the Diffraction of X-Rays” (Bell & sons, London), Chapter IV (1962).

[10] J. C. Slater, *The Quantum Theory of Matter* (McGraw Hill, New York), Second Edition, Chapter 14 (1968).

[11] A. H. Compton and S.K. Allison, “X-Rays in Theory and Practice” (Van Nostrand, New York), Second Edition (1935).

[12] R. L. Liboff, “Introductory Quantum Mechanics” (Addison-Wesley, Reading, MA,), Third Edition, (1998).

[13] L. Névot and P. Croce, “Caractérisation des surfaces par réflexion rasante de rayons X. Application à l'étude du polissage de quelques verres silicates” Rev. Phys. Appl. **15,** 761 (1980).

[14] D. E. Aspnes, “The accurate determination of optical properties by ellipsometry” In Handbook of Optical Constants of Solids, E. D. Palik Ed. (Academic Press, London UK) pp. 89-112 (1998).

[15] J. Pfluger, J. Fink, “Determination of optical constants by high energy electron energy loss spectroscopy (EELS)” In Handbook of Optical Constants of Solids, E.D. Palik Ed. (Academic Press, London UK) pp. 293-311 (1998).

[16] D. W. Lynch, “Optical constants”, In Handbook of Synchrotron Radiation, G.V. Marr Ed., (North-Holland, Elsevier Science, The Netherland) (1987).

[17] S. V. Pepper, “Optical Analysis of Photoemission” J. Opt. Soc. Am. **60,** 805 (1970).

[18] T. Ejima, “Formulae of Total Electron Yield for Multilayers: Extension of Pepper's Method” Jpn. J. Appl.Phys. **42**, 6459 (2003).

[19] T. Ejima, T. Harada, A. Yamazaki, “Optical constant measurements of the uppermost layer of a reflection multilayer using reflection and total electron yield spectra” Proc.of SPIE Vol.**6317** 630170Z (2006)**.**

[20] L. D. Landau and E.M. Lifshitz, “Electrodynamics of Continuous Media” (Addison-Wesley, NewYork), pp. 256–261 (1960).

[21] J. E. Marsden and M.J. Hoffman, “Basic Complex Analysis” (Freeman, New York), Second Edition, p. 548 (1973).

[22] F. Wooten, “Optical Properties of Solids” (Academic, New York) (1972).

[23] R. W. Ditchburn, “Light” (Blackie, London), Second Edition, Appendix XIX (1963).

[24] Han-chang Pan, Ming-HuaShiao, Chien-Ying, Chien-Nan Hsiao, “Influence of sputtering parameter on the optical and electrical properties of zinc-doped indium oxide thin films” J. Vac. Sci. Technol.A, **23** 1187 (2005).

[25] C. V. Ramana, E. J. Rubio, C. D. Barraza, A. Miranda Gallardo, Samantha McPeak, Sushma Kotru, J. T. Grant, “Chemical bonding, optical constants, and electrical resistivity of sputter-deposited gallium oxide thin films” J. Appl. Phys. **115**, 043508 (2014).

[26] Arijeet Das, Rajkumar K. Gupta, Mohammed H. Modi, Chandrachur Mukherjee, Sanjay K. Rai, Aniruddha Bose, Tapas Ganguli, Satish C. Joshi, Gyan S. Lodha, Sudip K. Deb, “Fine structures in refractive index of sapphire at the $L_{\_II,III}$ absorption edge of aluminum determined by soft x-ray resonant reflectivity” Appl. Opt. **30**, 7402 (2012).

[27] Xiaodong Wang, Guangming Wu, Bin Zhou, Jun Shen, “Optical Constants of Crystallized TiO_2 Coatings Prepared by Sol-Gel Process” Materials, **6,** 2819 (2013).

[28] Qi Zhong, Wenbin Li, Zhong Zhang, Jingtao Zhu, Qiushi Huang, Haochuan Li, Zhanshan Wang, Philippe Jonnard, Karine Le Guen, Jean-Michel André, Hongjun Zhou, Tonglin Huo, “Optical and structural performance of the Al(1% wtSi)/Zr reflection multilayers in the 17-19 nm region” Opt. Exp. **49** 10692 (2012).

[29] Qi Zhong, Zhong Zhang, Wenbin Li, Jingtao Zhu, Zhanshan Wang, Philippe Jonnard, Karine Le Guen, Yanyan Yuan, Jean-Michel André, Hongjun Zhou, Tonglin Huo, "Al/Zr multilayer mirror and its thermal stability for EUV application" J. Phys.: Conf. Ser. **425,** 152010 (1-5) (2013).

[30] E. Allaria, C. Callegari, D. Cocco, W. M. Fawley, M. Kiskinova, C. Masciovecchio, and F. Parmigiani, "The FERMI@Elettra free-electron-laser source for coherent x-ray physics: photon properties, beam transport system and applications" New J. Phys. **12** (7), 075002 (2011).

[31] W. Ackermann, G. Asova, V. Ayvazyan, A. Azima, et al., "Operation of a free-electron laser from the extreme ultraviolet to the water window" Nat. Photonics **1** (6), 336 (2007).

[32] A. R. Khorsand, R. Sobierajski, E. Louis, S. Bruijn, E. D. van Hattum, R. W. E. van de Kruijs, M. Jurek, D. Klinger, J. B. Pelka, L. Juha, T. Burian, J. Chalupsky, J. Cihelka, V. Hajkova, L. Vysin, U. Jastrow, N. Stojanovic, S. Toleikis, H. Wabnitz, K. Tiedtke, K. Sokolowski-Tinten, U. Shymanovich, J. Krzywinski, S. Hau- Riege, R. London, A. Gleeson, E. M. Gullikson, and F. Bijkerk, "Single shot damage mechanism of Mo/Si multilayer optics under intense pulsed XUV-exposure" Opt. Express **18**(2), 700 (2010).

[33] F. Barkusky, A. Bayer, S. Döring, P. Grossmann, and K. Mann, "Damage threshold measurements on EUV optics using focused radiation from a table-top laser produced plasma source" Opt. Express **18**(5), 4346 (2010).

[34] R. Sobierajski, S. Bruijn, A. R. Khorsand, E. Louis, R. W. E. van de Kruijs, T. Burian, J. Chalupsky, J. Cihelka, A. Gleeson, J. Grzonka, E. M. Gullikson, V. Hajkova, S. Hau-Riege, L. Juha, M. Jurek, D. Klinger, J. Krzywinski, R. London, J. B. Pelka, T. Płociński, M. Rasiński, K. Tiedtke, S. Toleikis, L. Vysin, H. Wabnitz, and F. Bijkerk, "Damage mechanisms of

MoN/SiN multilayer optics for next-generation pulsed XUV light sources” Opt. Express **19**(1), 193 (2011).

[35] F. Barkusky, A. Bayer, S. Döring, P. Grossmann, and K. Mann, Opt. Express, “Damage threshold measurements on EUV optics using focused radiation from a table-top laser produced plasma source” **18**(5), 4346 (2010).

[36] Amol Singh, M. H. Modi, A. K. Sinha, R. Dhawan, G. S. Lodha, “Study of structural and optical properties of zirconium carbide (ZrC) thin-films deposited by ion beam sputtering for soft x-ray optical applications” Surf. Coat.Tech. **272,** 409 (2015).

[37] A. F. Jankowski, L. R. Schrawyer, M. A. Wall, “Structural stability of heat-treated W/C and W/B4C multilayers” J. Appl. Phys. **68**, 5162 (1990).

[38] Mohammed H. Modi, S. K. Rai, Mourad Idir, F. Schaefers, G. S. Lodha, “NbC/Si multilayer mirror for next generation EUV light sources.” Opt Exp. **20,** 15114 (2012).

[39] M. Y. Liao, Y. Gotoh, H. Tsuji, and J. Ishikawa, “Compound-target sputtering for niobium carbide thin-film deposition” J. Vac. Sci. Technol. **B 22(5)**, L24 (2004).

[40] S. Barzilai, M. Weiss, N. Frage, and A. Raveh, “Structure and composition of Nb and NbC layers on graphite” Surf. Coat. Tech. **197(2-3)** 208 (2005).

[41] Mélissa DELHEUSY, Ph.D. Thesis, “X-ray investigation of Nb/O interfaces” submitted to UNIVERSITÄT STUTTGART FAKULTÄT MATHEMATIK UND PHYSIK July 2008 and Amol Singh, Mohammed H. Modi, G. S. Lodha, “Optical properties of zirconium carbide in 60–200 Å wavelength region using x-ray reflectivity technique” Appl. Opt. **54**, 253 (2015).

[42] B. L. Henke, E. M. Gullikson, and J. C. Davis, “X-Ray Interactions: Photoabsorption, Scattering, Transmission, and Reflection at E = 50-30,000 eV, Z = 1-92” At. Data Nucl.Data Tables **54**, 181–342 (1993).

[43] Edward D Palik “Handbook of optical constants of solids”, Orlando: Academic Press, 1985.

[44] P. N. Rao, Mohammed H. Modi, G. S. Lodha, “Optical properties of indium phosphide in the 50–200Å wavelength region using a reflectivity technique” Appl. Opt. **49**, 5378 (2010).

[45] D. Ksenzov, T. Panzer, C. Schlenper, C. Morawe, and U. Pietsch, “Optical properties of boron carbide near the boron K edge evaluated by soft x-ray reflectometry from a Ru/B4C multilayer” Appl. Opt. **48**, 6684 (2009).

[46] P. Gupta, A.K. Sinha, M.H. Modi, S.M. Gupta, P.K. Gupta, S.K. Deb, “Resonant soft x-ray reflectivity as a sensitive probe to investigate polished zinc sulphide surface” Appl. Surf. Sci. **257**, 210-214 (2010).

[47] D.L. Windt, “IMD: Software for modeling the optical properties of multilayer films” Comput. Phys. **12**, 360 (1998).

[48] J. Chen, E. Louis, C.J. Lee, H. Wormeester, R. Kunze, H. Schmidt, D. Schneider, R. Moors, W. van Schaik, M. Lubomska, F. Bijkerk, “Detection and characterization of carbon contamination on EUV multilayer mirrors” Opt. Exp. **19**, 16969 (2009).

[49] K. Boller, R.-P. Haelbich, H. Hogrefe, W. Jark, C. Kunz, “Investigation of carbon contamination of mirror surfaces exposed to synchrotron radiation” Nucl. Instrum.Methods in Phys. Research, **208**, 273 (1983).

[50] T. Koide, S. Sato, T. Shidara, et al. . Miyahara, “Investigation of carbon contamination of synchrotron radiation mirrors” Nucl. Instrum.Methods A, **246**, 215 (1986).

[51] C. Tarrio, S. Grantham, “Synchrotron beamline for extreme-ultraviolet multilayer mirror endurance testing” Rev. Sci. Instrum, **76**, 056101 (2005).

[52] A. G. Michette, “Optical system for soft x-rays” (Plenum Press, NewYork) (1986).

[53] E. Spiller, “Soft X-ray optics” (SPIE, Bellingham, WA, USA) (1994).

[54] J. H. Underwood, E. M. Gullikson, M. Koike, P. J. Batson, P. E. Denham, F. D. Franck, R. E. Tackaberry, W. F. Steele, “Calibration and standards beamline 6.3.2 at the Advanced Light Source” Rev. Sci. Instrum. **67,** 3372 (1996).

[55] C. Tarrio, R.N. Watts, T.B. Lucatorto, M. Haass, T.A. Calcott, J. Jia, “The New NIST/ARPA National Soft X-Ray Reflectometry Facility” J. X-ray Sci. Tech. **4,** 96 (1994).

[56] S.S. Ramamurthi, G. Singh, “Status of the INDUS-1 SR source” Nucl.Instr.MethodA **359** 15 (1995).

[57] R.V. Nandedkar, K.J.S. Sawhney, G.S. Lodha et al., “First results on the reflectometry beamline on Indus-1” Current Science **82,** 298 (2002)

[58] E.M. Gullikson, R. Korde, L.R. Canfield, R.E. Vest, “Stable silicon photodiodes for absolute intensity measurements in the VUV and soft X-ray regions” J. Elect. Spectr.and Rel. Phen. **80**, 313 (1996).

[59] Mohammed H. Modi, Rajkumar Gupta, Amol Singh, G. S. Lodha, “Quantitative determination of higher harmonic content in the soft x-ray spectra of toroidal grating monochromator using a reflection multilayer” Appl. Opt. **51**, 3552 (2012).

[60] A. K. Choubey, Amol Singh, Mohammed H. Modi, B.N. Upadhyaya, G.S. Lodha, S.M. Oak, “Study on effective cleaning of gold layer from fused silica mirrors using nanosecond-pulsed Nd:YAG laser” Applied Optics**, 52,** 7540-7548**,** 2013, and A.K. Choubey Ph.D. Thesis “Study and Development of High Power Pulsed Nd:YAG Lasers and Their Material Processing Applications ” Submitted to Homi Bhabha National Institute September 2014.

[61] Parasmani Rajput, Ph.D. Thesis “Depth-Resolved Structural Studies in Thin Films and Multilayers Using X-Ray Standing Waves” Submitted to Devi Ahilya Vishwavidyalaya, Indore 2008.

[62] G. Betz and G. K. Wehner, “Sputtering by Particle Bombardment II”, edited by R. Behrisch (Springer, Berlin, 1983).

[63] Paul van der Heide, “X-ray Photoelectron Spectroscopy: An introduction to Principles and Practices” John Wiley and sons Inc. (2012).

[64] B. E. Warren, “X-ray Diffraction”, (Addison-Wesley Publishing Company, 1969); R. Kaplow, N. Kato, R.J. Weiss, A.J.C. Wilson and R.A. Young, “Physics of X-ray Diffraction”, edited by L.V. Azaroff, (McGraw-Hill Book Co., 1974).

[65] A K Sinha, Archna Sagdeo, Pooja Gupta, AnujUpadhyay, Ashok Kumar, M N Singh, R K Gupta, S R Kane, A Verma, S K Deb, “Angle Dispersive X-ray Diffraction Beamline on Indus-2 Synchrotron Radiation Source: Commissioning and First Results” J. Phys.: Conf. Ser. **425** 072017 (2013).

[66] A.P. Hammersley, S.O. Svensson, A. Thompson, “Calibration and correction of spatial distortions in 2D detector systems” Nucl. Instr. Meth. A. **346,** 312 (1994).

[67] D. G. Stearns, et al., “Nonspecular x-ray scattering in a multilayer-coated imaging system” J. Appl. Phys. **84** 1003 (1998).

[68] P. A. Lee, P. H. Citrin, P. Eisenberger and B. M. Kinkaid, “Extended x-ray absorption fine structure-its strengths and limitations as a structural tool” Rev. Mod. Phys. **53**, 769 (1981).

[69] A. K. Poswal, A. Agrawal, A. K. Yadav, C. Nayak, S. Basu, S. R. Kane, C. K. Garg, D. Bhattachryya, S. N. Jha, N. K. Sahoo, “Commissioning and first results of scanning type EXAFS beamline (BL-09) at INDUS-2 synchrotron source” AIP Conf. Proc. **1591**, 649 (2014).

[70] S. Basu, C. Nayak, A. K. Yadav, A. Agrawal, A. K. Poswal, D. Bhattacharyya, S. N. Jha and N. K. Sahoo, “A comprehensive facility for EXAFS measurements at the INDUS-2 synchrotron source at RRCAT, Indore, India” J. Phys.: Conf. Ser. **493**, 012032 (2014).

[71] B. Ravel and M. Newville, "ATHENA, ARTEMIS, HEPHAESTUS: data analysis for X-ray absorption spectroscopy using IFEFFIT" J. Synch. Rad. **12**, 537 (2005).

[72] S. I. Zabinsky, J. J. Rehr, A. Ankudinov, R. C. Albers, and M. J. Eller, "Multiple-scattering calculations of x-ray-absorption spectra" Phys. Rev. B **52**, 2995 (1995).

[73] J. R. Ferraro, "Introductory Raman spectroscopy", 2nd ed., (Amsterdam, Boston: Academic Press., 2003) p. 3-97.

[74] T. Chasse, H. Neumann, B. Ocker, M. Scherer, W. Frank, F. Frost, D. Hirsch, A. Schindler, G. Wagner, M. Lorenz, G. Otto, M. Zeuner, B. Rauschenbach, "Mo/Si multilayers for EUV lithography by ion beam sputter deposition" Vacuum **71,** 407 (2003).

[75] G. F. Marshall, Ed, "Applications of Thin Film Multilayered Structures to Figured X-Ray Optics" SPIE Proc. **563,** (1985).

[76] N. M. Ceglio and P. Dhez, Eds, "Multilayer Structures & Laboratory X-Ray Laser Research" SPlE Proc. **688,** (1986).

[77] F. E. Christensen, Ed., "X-Ray Multilayers in Diffractometers, Monochromators, and Spectrometers" SPIE Proc. **984,** (1988).

[78] R. B. Hoover, Ed, "X-Ray/EUV Optics for Astronomy and Microscopy" SPIE Proc. **1160,** (1989).

[79] E.N. Zubarev, A.V. Zhurba, V.V. Kondratenko, V.I. Pinegyn, V.A. Sevryukova, S.A. Yulin, T. Feigl, N. Kaiser, "The structure, diffusion and phase formation in Mo/Si multilayers with stressed Mo layers" Thin Solid Films **515,** 7011 (2007).

[80] A. K. Petford·Long, M. B. Stearns, C.-H. Chang, S. R. Nutt, D. G. Stearns, N. M. Ceglio. and A. M. Hawryluk, "High-resolution electron microscopy study of x-ray multilayer structures" J. Appl. Phys. **61,** 1422 (1987).

[81] Stefan Braun, Hermann Mai, Matthew Moss, Roland Scholz and Andreas Leson, "Mo/Si Multilayers with Different Barrier Layers for Applications as Extreme Ultraviolet Mirrors" Jpn. J. Appl. Phys. **41**, 4074 (2002).

[82] H. Maury, P. Jonnard, J.-M. André, J. Gautier, M. Roulliay, F. Bridou, F. Delmotte, M.-F.Ravet, A. Jérome, and P. Holliger, "Non-destructive X-ray study of the interphases in Mo/Si and Mo/B4C/Si/B4C multilayers" Thin Solid Films **514,** (1-2), 278 (2006).

[83] A. F. Jankowski, L. R. Schrawyer, M. A. Wall, "Structural stability of heat-treated W/C and W/B4C multilayers" J. Appl. Phys. **68**, 5162 (1990).

[84] http://henke.lbl.gov/optical_constants/

[85] T. Ohnishi, T. Yamamoto, S. Meguro, H. Koinuma, M. Lippmaa, "Pulsed laser ablation and deposition of complex oxides" J. Phys.: Conf. Ser. **59,** 514 (2007).

[86] Jeffrey A. Klug, Thomas Proslier, Jeffrey W. Elam, Russell E. Cook, Jon M. Hiller, Helmut Claus, Nicholas G. Becker, Michael J. Pellin, "Atomic Layer Deposition of Amorphous Niobium Carbide-Based Thin Film Superconductors" J. Phys. Chem. C **115**, 25063 (2011).

[87] S.K Rai, PhD Thesis, "Interface Characterization of Multilayer Mirrors" (2013).

[88] L.G. Parratt, "Surface Studies of Solids by Total Reflection of X-Rays" Phys. Rev. **95**, 359 (1954).

[89] A. Nelson, "Co-refinement of multiple-contrast neutron/X-ray reflectivity data using MOTOFIT" J. App. Cryst. **39**, 273 (2006).

[90] S K Deb, Gurnam Singh, P D Gupta, "Indus-2 Synchrotron Radiation Source: current status and utilization" J. Phys.: Conf. Ser. **425,** 072009 (2013).

[91] A. P. Hammersley, S. O. Svensson, M. Hanfland, A. N. Fitch, D. Häusermann, "Two-dimensional detector software: From real detector to idealised image or two-theta scan" High Pressure Research, **14,** 235 (1996).

[92] http://srdata.nist.gov/xps/Default.aspx

[93] S. Kodama, N. Ichikuni, K. K. Bando, T. Hara, S. Shimazu, "Preparation of supported NbC catalysts from peroxoniobic acid and in situ XAFS characterization" Applied Catalysis A: General, **25,** 343 (2008).

[94] D. C. Koningsberger et al., "X-Ray Absorption: Principles, Applications, Techniques of EXAFS, SEXAFS and XANES" John Wiley & Sons, 1988.

[95] R. Soufli and E. M. Gullikson, "Reflectance measurements on clean surfaces for the determination of optical constants of silicon in the extreme ultraviolet–soft-x-ray region" Appl. Opt. **36**, 5499 (1997).

[96] Yutai Katoh, Gokul Vasudevamurthy Takashi Nozawa Lance L. Snead, "Properties of zirconium carbide for nuclear fuel applications" J. Nucl. Mat. **441**, 718 (2013).

[97] B. V. Cockeram, D. P. Measures, and A. J. Mueller, "The development and testing of emissivity enhancement coatings for themophotovoltaic (TPV) radiator applications" Thin Solids Films, **355-356,** 17 (1999).

[98] F. M. Charbonnier, W. A. Mackie, R. L. Hartman, and Tianbao Xie, "Robust high current field emitter tips and arrays for vacuum microelectronics devices" J. Vac. Sci. Technol. B, **19,** 1064 (2001).

[99] V. Craciun, E.J. McCumiskey, M. Hanna, C.R. Taylor, "Very hard ZrC thin films grown by pulsed laser deposition" J Eur. Cer. Soc. **33,** 2223 (2013).

[100] D. Craciun, G. Socol, N. Stefan, G. Broune, V. Cracium, “Chemical composition of ZrC thin films grown by pulsed laser deposition” Appl. Sur. Sci. **255,** 5260 (2009).

[101] R. Kaufmann, H. Klewe-Nebenius, H. Moers, G. Pfenning, H. Jenett, J. H. Ache, “XPS studies of the thermal behaviour of passivated Zircaloy-4 surfaces” Surf. Interf. Anal.**11,** 502 (1988).

[102] M. Balaceanu, M. Braic, V. Braic, A. Vladecsu, C. C. Negrila, “Surface chemistry of plasma deposited ZrC hard coatings” J. Optoelectr. Adv. Mater. **7**, 2557 (2005).

[103] M. E. Couprie, M. Billardon, M. Velghe, C. Bazin, M. Bergher, H. Fang, J. M. Ortega, Y. Petrof, and R. Prazeres, “Optical properties of multilayer mirrors exposed to synchrotron radiation” Nucl. Instrum. Methods Phys. Res., Sect. A **272**, 166 (1988).

[104] F Eggenstein, F Senf, T Zeschke, W Gudat, “Cleaning of contaminated XUV-optics at BESSY II” Nucl. Instr. and Meth A. **467-468,** 325 (2001).

[105] C. Chauvet, F. Polack, M. G. Silly, B. Lagarde, M. Thomasset, S. Kubsky, J. P. Duval, P. Risterucci, B. Pilette, I. Yao, N. Bergeard and F. Sirotti, “Carbon contamination of soft X-ray beamlines: dramatic anti-reflection coating effects observed in the 1 keV photon energy region” J. Synchrotron Rad. **18**, 761 (2011).

[106] T T. Koide, T. Shidara, K. Tanaka, A. Yagishita and S. Sato, “In-situ dc oxygen discharge cleaning system for optical elements” Rev. Sci. Instrum. **60**, 2034 (1989).

[107] R. A. Rosenberg and D. B. Crossley, “Oxygen rf-discharge cleaning: Plasma characterization and implementation on a grasshopper beam line” Nucl. Instr. and Meth A. **266**, 386 (1988).

[108] J. M. Lee and K. G. Watkins, “Removal of small particles on silicon wafer by laser-induced airborne plasma shock waves” J. Appl. Phys. **89**, 6496 (2001).

[109] Roger W.C. Hansen, Jeff Wolske, Peter Z. Takacs, "UV/ozone cleaning of a replica grating" Nucl. Instr. and Meth A. **347,** 254 (1994).

[110] http://www.synchrotron-soleil.fr/Workshops/2012/SRI2012-Sat.Carbon12

[111] G. Guéhenneux, M. Veillerot, I. Tovena, "Evaluation of the airborne molecular contamination inside the LIL" Nucl. Instr. and Meth A. **557**, 676 (2006).

[112] Karell Bien-Aimé, Jérome Néauport, Isabelle Tovena-Pecault, EvelyneFargin, Christine Labrugère, Colette Belin, and Michel Couzi, "Laser induced damage of fused silica polished optics due to a droplet forming organic contaminant" Appl. Opt. **48**, 2228 (2009).

[113] C. Tam, W. P. Leung, W. Zapka, and W. Ziemlich, "Laser-cleaning techniques for removal of surface particulates" J. Appl. Phys. **71**, 3515 (1992).

[114] Jie Zhang,Youneng Wang, Peng Cheng, and Y. Lawrence Yao, "Effect of pulsing parameters on laser ablative cleaning of copper oxides" J. Appl. Phys. **99,** 064902-1 (2006).

[115] J. Padma Nilaya, Pallavi Raote, Aniruddha Kumar and Dhruba J. Biswas, "Laser-assisted decontamination-A wavelength dependent study" Appl. Surf. Sci. **254,** 7377 (2008).

[116] H. Guo, R. Martukanitz and T. Deb Roy, "Laser assisted cleaning of oxide films on SUS409 stainless steel" J. Laser Appl. **16,** 236 (2004).

[117] E. G. Gamaly, A. V. Rode, and B. Luther-Davies, "Ultrafast ablation with high-pulse-rate lasers. Part I: Theoretical considerations" J. Appl. Phys. **85,** 4213 (1999).

[118] A. V. Rode, B. Luther-Davies, and E. G. Gamaly, "Ultrafast ablation with high-pulse-rate lasers. Part II: Experiments on laser deposition of amorphous carbon films" J. Appl. Phys. **85,** 4222 (1999).

[119] Ariana Bratt, Andrew R. Barron, "XPS of Carbon Nanomaterials" http://cnx.org/content/m34549/1.2/ (last viewed 01.09.15).

[120] T.V. Kononenko, S.M. Pimenov, V.V. Kononenko, E.V. Zavedeev, V.I. Konov, G. Dumitru, V. Romano, “Laser-induced spallation in diamond-like carbon films” Appl. Phys. A **79**, 543 (2004).

[121] J. Gaudin, O. Peyrusse, J. Chalupsky, M. Toufarova, L. Vysın, V. Hajkov, R. Sobierajski, T. Burian, Sh. Dastjani-Farahani, A. Graf, M. Amati, L. Gregoratti, S. P. Hau-Riege, G. Hoffmann, L. Juha, J. Krzywinski, R. A. London, S. Moeller, H. Sinn, S. Schorb, M. Störmer, Th. Tschentscher, V. Vorlıcek, H. Vu, J. Bozek, C. Bostedt, “Amorphous to crystalline phase transition in carbon induced by intense femtosecond x-ray free-electron laser pulses” Phys. Rev. B, **86,** 024103 (2012).

[122] Jacob Filik, “Raman spectroscopy: a simple, non-destructive way to characterize diamond and diamond-like materials” Spectroscopy Europe **17,** 10 (2005).

[123] B. R. Müller, J. Feldhaus, F. Schäfers and F. Eggenstein, “Cleaning of carbon contaminated vacuum ultraviolet-optics: Influence on surface roughness and reflectivity” Rev. Sci. Instrum. **63**, 1428 (1992).

[124] Kazuumi Tanaka, Kazuhiro Hamamoto, Noriyuki Sakaya, Morio Hosoya, Takeo Watanabe, and Hiroo Kinoshita, “Cleaning Characteristics of Contaminated Imaging Optics Using 172 nm Radiation” Jpn. J. Appl. Phys. **46**, 6150 (2007).